



저작자표시-비영리-변경금지 2.0 대한민국

이용자는 아래의 조건을 따르는 경우에 한하여 자유롭게

- 이 저작물을 복제, 배포, 전송, 전시, 공연 및 방송할 수 있습니다.

다음과 같은 조건을 따라야 합니다:



저작자표시. 귀하는 원저작자를 표시하여야 합니다.



비영리. 귀하는 이 저작물을 영리 목적으로 이용할 수 없습니다.



변경금지. 귀하는 이 저작물을 개작, 변형 또는 가공할 수 없습니다.

- 귀하는, 이 저작물의 재이용이나 배포의 경우, 이 저작물에 적용된 이용허락조건을 명확하게 나타내어야 합니다.
- 저작권자로부터 별도의 허가를 받으면 이러한 조건들은 적용되지 않습니다.

저작권법에 따른 이용자의 권리는 위의 내용에 의하여 영향을 받지 않습니다.

이것은 [이용허락규약\(Legal Code\)](#)을 이해하기 쉽게 요약한 것입니다.

[Disclaimer](#)

Thesis for the Doctor of Philosophy

**Phase study and thermoelectric
properties of Cu_2SnSe_3 for green
energy harvesting**

August 2019

Graduate School of Seoul National University,
School of Materials Science and Engineering,
Republic of South Korea

MUHAMMAD SIYAR

Phase study and thermoelectric properties of Cu_2SnSe_3 for green energy harvesting

Supervisor: Prof. Park Chan

A thesis submitted to the graduate school of Seoul National University in partial fulfillment of the requirement of the degree of Doctor of Philosophy

August 2019

MUHAMMAD SIYAR

**Confirming the Ph.D. Dissertation written by
Muhammad Siyar**

August 2019

Chair: Sang-Im Yoo

Vice Chair: Park Chan

Examiner: Mi-Young Kim

Examiner: Jin-Sang Kim

Examiner: Sung-Hwan Bae

Acknowledgments

Great collaborations under the guidance of my advisor Professor Park Chan allowed this thesis to come to fruition. I really appreciate his kind guidance and endless support during my PhD research and stay in South Korea. I am really thankful to my advisory committee members, Prof. Mi-Young Kim, Prof. Jin-Sang Kim, and Asst Prof. Sung-Hwan Bae for their comments and valuable suggestions. I appreciate the precious support and help of all my lab colleagues at SNU, due to which my stay in the lab was pleasant and enjoyable. I extend my sincere thanks to all members of the MSE, SNU and all those who contributed directly or indirectly to this dissertation.

Outside of work, I would like to thank a number of people at SNU and outside the SNU like Dr Sajid Anwar, Dr ateeq-Ur-Rehman, Mr. Wiqar Ahmad and all MKH group members who made my time in Seoul so enjoyable. Finally, I'd like to thank those closest to me for sticking out these five years with me. My mother, brothers, and the rest of my family are a constant source of happiness and motivation for me. Without their endless support, motivation and appreciation, my goal of getting PhD may not be fulfilled. Most importantly, I would like to thank my amazing wife Dr Ambreen khan. She was unfailingly supportive for the past three years, never complaining about family matters so I could complete graduate school at SNU. Finally I dedicate my PhD dissertation work to my father who has given me the true essence of education from my childhood.

Abstract

TE energy harvesting is one of the approaches to address the global environmental challenges, utilizing waste heat for useful electric power generation. This technology recently attracted attention of the commercial sectors, due to the possible applications of TE materials in wearable electronic devices, solid state Peltier cooling, remote area sensors, etc. Currently available commercial TE materials such as Bi_2Te_3 , Sb_2Te_3 and PbTe consist of either toxic or expensive elements. Therefore, exploration of TE materials with less toxic, less expensive and more earth-abundant elements is the focus of the TE community these days. The ternary chalcogenide Cu_2SnSe_3 is expected to be one of these auspicious TE materials, owning large flexibility to tune its physical and electronic properties. The elements of Cu_2SnSe_3 are less toxic, abundant in nature and relatively cheap compared to Te and Pb.

Previous studies reported that Cu_2SnSe_3 can be found in various allotropic forms, which include orthorhombic, monoclinic and cubic structures. Phase transformation in solid state compounds involves rearrangement of atoms, which can be induced by the change of temperature, pressure and/or composition. It is important to understand the thermodynamic conditions of these diverse phases since different synthesis conditions and stoichiometry can lead to the formation of different phases. Phase transitions can lead to different band gap and lattice parameters, which can further affect the physical properties. The effect of annealing temperature on the phase transition of Cu_2SnSe_3 was investigated, and the TE properties of the monoclinic and cubic phases of Cu_2SnSe_3 were compared for the first time. Stoichiometric composition of Cu_2SnSe_3 was synthesized by melt

solidification and heat treatment at various temperatures followed by water quenching. XRD analyses reveal that the samples annealed at 720 and 820 K have mostly monoclinic phase along with small amount of cubic phase. The Cu_2SnSe_3 annealed at 960 K is mostly cubic. It was found that the mostly cubic phase has ZT much higher than the mostly monoclinic phase sample. Better TE performance of high temperature cubic phase can be attributed to the smaller band gap (~ 0.92 eV) which can lead to higher electrical conductivity than monoclinic (~ 1.0 eV) at room temperature.

Although the cubic phase Cu_2SnSe_3 has slightly higher thermoelectric efficiency than the monoclinic phase but still the ZT of both the phases is much lower compare to commercialized PbTe thermoelectric material. It can be realized that both have nearly similar thermoelectric properties but still the ZT of the Cu_2SnSe_3 is much lower than the PbTe due to the lower Seebeck coefficient of the Cu_2SnSe_3 . To improve the Seebeck coefficient of the Cu_2SnSe_3 we synthesized CTSe-SnS composites by mechanical alloying followed by spark plasma sintering. An optimized improvement in TE properties was achieved by adding 3% SnS to the CTSe matrix, which led to enhanced ZT in the medium temperature range. It was found that SnS addition to Cu_2SnSe_3 (CTSe) can effectively enhance the Seebeck coefficient from 30 to 490 $\mu\text{Volt/K}$ at room temperature, but the power factor was not much improved due to the loss of electrical conductivity. But still, a prominent improvement in ZT value from 0.06 to 0.18 at 570 K for the CTSe was achieved due to disorder scattering, which can lead to a lower thermal conductivity of the composites than the pristine CTSe. The results show that the thermoelectric properties of CTSe can be engineered by the presence of SnS phase in the CTSe matrix.

Despite of large improvement enhancement in Seebeck coefficient in the Cu_2SnSe_3 -SnS composites, the improvement in the ZT value was not that impressive due to

loss of electrical conductivity. It is a big challenge to decouple Seebeck coefficient and electrical properties in alloying and composites, where increasing one value will lead to compromise another. Doping and solid solution can be one of the promising approaches to control the Seebeck coefficient without largely compromising the electrical conductivity for improved ZT of the various thermoelectric materials.

Here we introduced a strategy to control the Seebeck coefficient without losing large part of electrical conductivity of the CTSe by making its solid solution with Cu_2SnS_3 (CTS). Suppressing Se vacancies by introducing S in the CTSe lattice is one of the way to control the Seebeck coefficient. The analogous crystal and band structure of Cu_2SnSe_3 (CTSe) with Cu_2SnS_3 (CTS) was the motivation behind the study of TE performance of $\text{Cu}_2\text{Sn}(\text{S}_x, \text{Se}_{1-x})_3$ ($0 \leq X \leq 0.8$) solid solution. CTSe and $\text{Cu}_2\text{Sn}(\text{S}_x, \text{Se}_{1-x})_3$ ($0 \leq X \leq 0.8$) solid solution were prepared using mechanical alloying (MA) followed by spark plasma sintering. Rietveld refinement of the powder X-ray diffraction (XRD) data was performed to determine the variation in the lattice constants of the $\text{Cu}_2\text{Sn}(\text{S}_x, \text{Se}_{1-x})_3$ ($0 \leq X \leq 0.8$) solid solution with gradual replacing of Se with S. Here we found that the band gap and TE properties optimization as well as reducing in thermal conductivity can be efficiently achieved by careful optimizing of the composition of $\text{Cu}_2\text{Sn}(\text{S}_x, \text{Se}_{1-x})_3$ ($0 \leq X \leq 0.8$) solid solution for enhanced TE performance of the CTSe.

Finally making thin films and 2D structures of the Cu_2SnSe_3 can be another way to explore the its commercial potential due to its higher power density, light weight and compact size. Due to high conductive nature of the Cu_2SnSe_3 it is expected that the Cu_2SnSe_3 thin film can give us much better TE properties compare to thin films of conventional TE compounds like SnSe, due to incorporation of defects during thin film deposition. CTSe thin films were successfully deposited by PLD for the first time, and the effects of substrate temperature on the microstructure

and TE properties of the films were investigated. A monoclinic CTSe target and Pt-coated silicon substrates were used to deposit films at substrate temperatures of 300, 350 and 400 °C. The TE properties of the films were studied, and it was found that 350 °C is the optimized substrate temperature in which the highest power factor of 2.8×10^{-4} (W/m²K) was achieved among the studied samples. Increasing substrate temperature further up to 400 °C degraded the microstructure and electrical properties of the deposited film, and hence the power factor was decreased compared to the other films deposited at 300 and 350 °C. The power factor of 2.8×10^{-4} (W/m²K) of the sample deposited at 350 °C is very close to the reported value for bulk CTSe. A high power factor which is comparable with bulk CTSe, along with other benefits like higher energy density, light weight and compact size, makes CTSe film a potential candidate for various TE applications.

Keyword: Thermoelectric, Cu₂SnSe₃, Phase studies, Composites, Solid solution,

Student Number: 2014-31423

Table of contents

1 Chapter 1	11
1.1 Introduction.....	11
1.2 References.....	19
2 Chapter 2	20
2.1 Introduction to thermoelectricity.....	20
2.2 Efficiency and ZT.....	24
2.3 TE Materials in Use.....	25
2.4 References:.....	35
3 Chapter 3	37
3.1 General properties of Cu_2SnSe_3	37
3.2 Phase studies of Cu_2SnSe_3	37
3.3 TE studies on Cu_2SnSe_3	38
3.4 Approaches for ZT improvement of Cu_2SnSe_3	39
4 Chapter 4	42
Effect of annealing temperature on the phase transition, band gap and thermoelectric properties of Cu_2SnSe_3	42
4.1 Introduction.....	42

4.2	Experimental procedure	44
4.2.1	Sample preparation:.....	44
4.2.2	Characterization:	44
4.3	Results and Discussions	46
4.3.1	Phase analysis	46
4.3.2	Electronic transport properties	48
4.4	Summary.....	64
4.5	References:	65
5	Chapter 5.....	68
5.1	Introduction.....	68
5.2	Materials and Methods.....	70
5.3	Results and discussion.....	71
5.4	Summary.....	86
5.5	References	86
6	Chapter 6.....	91
6.1	Introduction.....	91
6.2	Experimental procedure	93
6.2.1	Sample preparation:.....	93
6.2.2	Characterization:	94

6.3	Results and Discussions	95
6.4	Summary.....	105
6.5	References:.....	105
7	Chapter 7.....	107
7.1	Introduction.....	107
7.2	Experimental procedure	109
7.2.1	Sample preparation.....	109
7.2.2	Substrate preparation	109
7.2.3	Deposition process.....	110
7.2.4	Characterizations.....	110
7.3	Results and discussion.....	112
7.4	Summary.....	123
7.5	References:.....	124

1 Chapter 1

1.1 Introduction

Despite of the issues facing for energy security by the modern industrialized world, green energy production is the ultimate goal to sustainable future of the world. The industrialization of the current era enabled the people life prosperous on one side but raised the other numerous challenges to the planet such as global warming and other environmental issues. To ensure the sustainable economic growth without affecting the environment of the green planet, scientists worked hard to divert the energy production from direct resource utilization to the renewable energy resources. Nonrenewable energy resources are limited while renewable energy resources have cost and capacity issues. So energy harvesting is crucial for the coming modern world where energy sector will face bigger challenges in the future. Energy harvesting by waste heat utilization, not only increases the capacity of any energy system but it also reduces the waste heat going in to the atmosphere. Among the various waste heat recovery systems, the TE technology is an efficient way where waste heat is directly converted into useful electric power. The whole system is very simple, comprised of mainly of the solid state TE materials, and haven't any large moving parts. The TE energy is more silent and green compare to other conventional heat recovery systems. One more unique feature of this technology is that, it not merely converts heat directly into electric power but can also utilize the electric power to produce

instant cooling. So the TE system can be used for various applications of energy generations as well as electronic refrigeration systems. The performance of a TE materials is evaluated on the basis of the dimensionless figure of merit, $ZT = S^2\sigma T/\kappa$, where σ is the electrical conductivity, S is the Seebeck coefficient, κ is the total thermal conductivity and T is the absolute temperature in Kelvin [1]. Increase in ZT requires high values of S and σ but still low thermal conductivity. It is very hard to control these TE parameters independently, where all of them are connected to each other by one way or another. It is the rule of thumb that semiconductors can be a better choice due to high Seebeck coefficient and dominant heat conduction by phonon migration [2]. These days most of the commercialized TE materials are mostly semiconductors compounds or alloys as shown in the Fig. 1. Further any material has own best operating temperature range in which its performance is high. For example, Bi_2Te_3 types TE materials shows high performance in low temperature range from around room temperature to $200\text{ }^\circ\text{C}$ [3]. Similarly, PbTe and half Heusler materials shows high performance in medium temperature range, while SiGe and oxide based TE materials are better for high temperature applications. Bismuth telluride can be alloyed with Sb_2Te_3 or Bi_2Se_3 , which reduces thermal conductivity considerably [4]. Problems with tellurium arise, since it is scarce, toxic and volatile at high temperatures [5]. Therefore, the use of tellurium is limited. Lead telluride (PbTe) was found to have good TE properties at temperatures in the range of $300\text{--}700\text{ K}$. To date the TE technology is not commercially mature due to its low efficiency. Apart from the low efficiency other challenges includes the high cost and toxicity

of the elements used in the TE modules. TE materials such as Bi_2Te_3 , Sb_2Te_3 and PbTe consist of either toxic or expensive elements [5, 6]. Therefore, study of TE materials with less toxic, less expensive and more earth-abundant elements, is the focus of the TE community these days. The ternary chalcogenide CTSe is expected to be one of these auspicious TE materials, owning large flexibility to tune its physical and electronic properties [7]. The elements of CTSe are less toxic, abundant in nature and relatively cheap compared to Te and Pb.

In the structure of CTSe, Sn orbitals have a small effect on carrier transport, and Cu-Se atoms form carrier conductive bond network which determines electrical conductivity [7]. Therefore, it is possible to control the TE properties of CTSe by doping on the Sn site. It can increase the effective mass to achieve high Seebeck coefficient while preserving 3D conductive framework as electron-crystal like structure [8]. The dimensionless figure of merit (ZT) of ~ 1.2 was reported by Li et al. in In-doped CTSe compound at 850 K [9].

Previous studies reported that CTSe can be found in various allotropic forms, which include orthorhombic, monoclinic and cubic structures [10, 11]. Phase transformation in solid state compounds involves rearrangement of atoms, which can be induced by the change of temperature, pressure and/or composition. It is important to understand the thermodynamic conditions of these diverse phases since different synthesis conditions and stoichiometry can lead to the formation of different phases. Phase transitions can lead to different band gap and lattice parameters, which can further affect the physical properties.

In this dissertation work we first studied the various phases of CTSe, possibly present at different temperature and compare its TE properties. Later we tried to control the various TE parameters of the CTSe structure for improved ZT. In chapter 3 the effect of annealing temperature on the phase transition of CTSe was investigated and the TE properties of the monoclinic and cubic phases of CTSe were compared for the first time. Stoichiometric composition of CTSe was synthesized by melt solidification and heat treatment at various temperatures followed by water quenching. XRD analyses reveal that the samples annealed at 720 and 820 K have mostly monoclinic phase along with small amount of cubic phase. The CTSe annealed at 960 K is mostly cubic. It was found that the mostly cubic phase has ZT much higher than the mostly monoclinic phase sample. Better TE performance of high temperature cubic phase can be attributed to the smaller band gap (~ 0.92 eV) which can lead to higher electrical conductivity than monoclinic (~ 1.0 eV) at room temperature.

In chapter 4 we found that the cubic phase CTSe has slightly higher TE efficiency than the monoclinic phase but still the ZT of both the phases is much lower compare to commercialized PbTe TE material. It can be realized that both have nearly similar TE properties but still the ZT of the CTSe is much lower than the PbTe due to the lower Seebeck coefficient of the CTSe. To improve the Seebeck coefficient of the CTSe we synthesized CTSe-SnS composites by mechanical alloying followed by spark plasma sintering and the study is given in chapter 5. Alloying or composites are studied to be the efficient ways for enhancing Seebeck coefficient of various TE materials, where optimum doping in

composites can increase the effective mass of the system which can lead to enhance the Seebeck coefficient¹⁴. An optimized improvement in TE properties was achieved by adding 5% SnS to the CTSe matrix, which led to enhanced ZT in the medium temperature range. It was found that SnS addition to CTSe can effectively enhance the Seebeck coefficient from 30 to 490 $\mu\text{V}/\text{K}$ at room temperature, but the power factor was not much improved due to the loss of electrical conductivity. But still, a prominent improvement in ZT value from 0.06 to 0.15 at 570 K for the CTSe was achieved due to disorder scattering, which can lead to a lower thermal conductivity of the composites than the pristine CTSe. The results of theoretical calculations were in agreement with the experimental results which suggest that SnS addition to the CTSe matrix reduce its thermal conductivity by introducing an extra scattering parameter to the thermal conductivity due to the disorder in the composite structure. The results show that the TE properties of CTSe can be engineered by the presence of SnS phase in the CTSe matrix.

Despite of large improvement enhancement in Seebeck coefficient in the CTSe – SnS composites, the improvement in the ZT value was not that impressive due to loss of electrical conductivity. It is a big challenge to decouple Seebeck coefficient and electrical properties in alloying and composites, where increasing one value will lead to compromise another. Here we introduced a strategy in chapter 6 to control the Seebeck coefficient without losing large part of electrical conductivity of the CTSe by making its solid solution with CTS. Suppressing Se vacancies by introducing S in the CTSe lattice is one of the ways to control the

Seebeck coefficient. The analogous crystal and band structure of CTSe with CTS was the motivation behind the study of TE performance of $\text{Cu}_2\text{Sn}(\text{S}_x, \text{Se}_{1-x})_3$ ($0 \leq X \leq 0.8$) solid solution. CTSe and $\text{Cu}_2\text{Sn}(\text{S}_x, \text{Se}_{1-x})_3$ ($0 \leq X \leq 0.8$) solid solution were prepared using mechanical alloying (MA) followed by spark plasma sintering. Rietveld refinement of the powder X-ray diffraction (XRD) data was performed to determine the variation in the lattice constants of the $\text{Cu}_2\text{Sn}(\text{S}_x, \text{Se}_{1-x})_3$ ($0 \leq X \leq 0.8$) solid solution with gradual replacing of Se with S. Here we found that the band gap and TE properties optimization as well as reducing in thermal conductivity can be efficiently achieved by careful optimizing of the composition of $\text{Cu}_2\text{Sn}(\text{S}_x, \text{Se}_{1-x})_3$ ($0 \leq X \leq 0.8$) solid solution for enhanced TE performance of the CTSe.

Finally making thin films and 2D structures of the CTSe can be another way to explore the its commercial potential due to its higher power density, light weight and compact size. Due to high conductive nature of the CTSe it is expected that the CTSe thin film can give us much better TE properties compare to thin films of conventional TE compounds like SnSe, due to incorporation of defects during thin film deposition.

In chapter 7 the TE studies on the CTSe thin films deposited by PLD was carried out for the first time, and the effects of substrate temperature on the microstructure and TE properties of the films were investigated. A monoclinic CTSe target and Pt-coated silicon substrates were used to deposit films at substrate temperatures of 300, 350 and 400 °C. The crystal structure was successfully transferred to the Si substrate from the CTSe target by laser ablation

without any phase changes, and all three film samples retained the monoclinic phase structure. The TE properties of the films were studied, and it was found that 350 °C is the optimized substrate temperature in which the highest power factor of 2.8×10^{-4} (W/m²K) was achieved among the studied samples. Increasing substrate temperature further up to 400 °C degraded the microstructure and electrical properties of the deposited film, and hence the power factor was decreased compared to the other films deposited at 300 and 350 °C. The power factor of 2.8×10^{-4} (W/m²K) of the sample S2 is very close to the reported value for bulk CTSe. A high power factor which is comparable with bulk CTSe, along with other benefits like higher energy density, light weight and compact size, makes CTSe film a potential candidate for various TE applications.

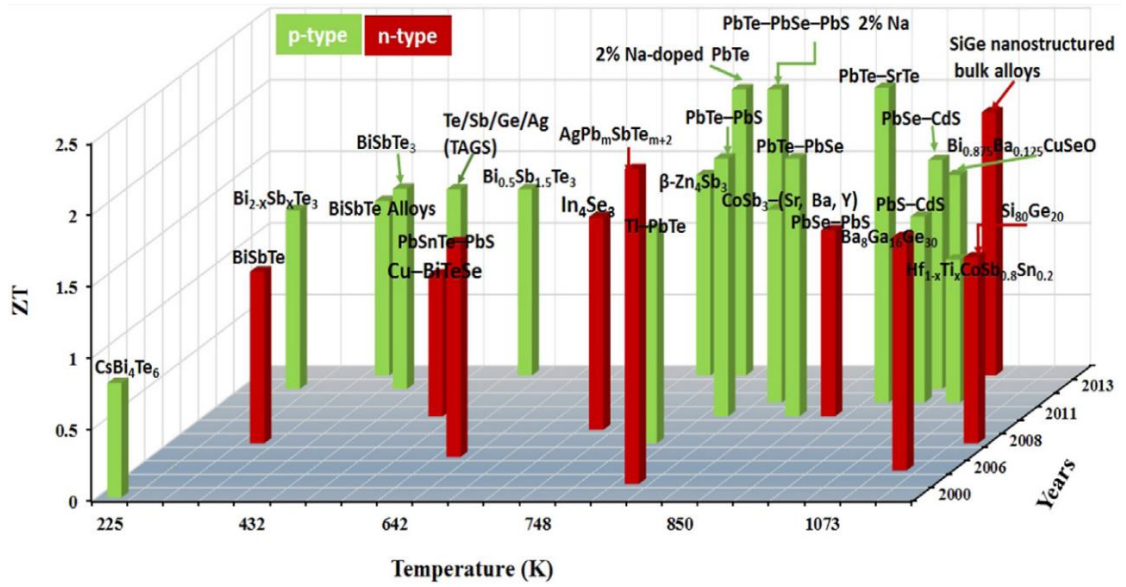


Figure 1. Schematics representation of ZT values of the of P-type and n-type Thermoelectric materials with respect to time line and temperature. [11]

1.2 References

- 1) Goldsmid, H. J. "Bismuth Telluride and Its Alloys as Materials for Thermoelectric Generation." *Materials* 7, no. 4 (Apr 2014): 2577-92. <http://dx.doi.org/10.3390/ma7042577>.
- 2) F. Ioffe, A. F. (Abram Fedorovich). *Semiconductor thermo elements and TE cooling* (1880-960).
- 3) GE, Z. H., ZHAO, L. D., WU, D., LIU, X. Y., ZHANG, B. P., LI, J. F, HE, J. Q. . "Low-Cost, Abundant Binary Sulfides as Promising Te Materials." *Materials Today* 19 (2016): 227-39.
- 4) J. Fan, H. L. Liu, X. Y. Shi, S. Q. Bai, X. Shi, L. D. Chen. *Acta Mater* 61 (2013): 4297-304.
- 5) J. Fan, H. L. Liu, X. Y. Shi, S. Q. Bai, X. Shi, L. D. Chen,. *Acta Mater* 61 (2013): 4297-304.
- 6) J. Fan, W. Schnelle, I. Antonyshyn, I. Veremchuk, W. Carrillo-Cabrera, X. Shi, Y. Grin, L. D. Chen, Dalton T. (
- 7) Minnich, A. J., M. S. Dresselhaus, Z. F. Ren, G. Chen. "Bulk Nanostructured Te Materials: Current Research and Future Prospects." *Energy & Environmental Science* 2, no. 5 (2009): 466-79.
- 8) WU, H, LI, R. " Properties of Bismuth Telluride Nanomaterials: A Computer Simulation Study." *Journal of Nanoelectronics and Optoelectronics* 12 (2017): 1199-202.
- 9) WU, H. LI, R. "Properties of Bismuth Telluride Nanomaterials: A Computer Simulation Study." *Journal of Nanoelectronics and Optoelectronics* 12 (2017): 1199-202.
- 10) X. Y. Shi, L. L. Xi, J. Fan, W. Q. Zhang, L. D. Chen. *Chem Mater* 22 (2010): 6029-31.
- 11) Y. Y. Li, G. H. Liu, J. T. Li, K. X. Chen, G. He, Z. C. Yang, Y. M. Han, M. Zhou, L. F. Li, . *Mater Chem Phys* 177 (2016): 398-404.

2 Chapter 2

General background

2.1 Introduction to thermoelectricity

Thermoelectricity is the generation of direct power from the junction of two dissimilar metals upon heating or cooling this junction by external electric power through two related mechanisms, the Seebeck effect and Peltier effects respectively [1]. When two metals are placed in electric contact, electrons flow out of the one in which the electrons are less bound and into the other. When two dissimilar metals are brought into electrical contact, the electrons flow from the metal where it is relatively weak bonded towards the other side. The bonding of electrons is referring to the hypothetical location which is called the Fermi energy level of electrons in any material [2]. The higher is the Fermi energy level the lower is the bonding with in the metal. Fermi energy level is the quantum mechanics term used for the energy difference between the occupied and unoccupied electrons energy levels at temperature of the absolute zero [3]. The flow of electrons from the higher Fermi energy state towards the lower energy states will continue until the Fermi levels of the two metals (F_1 and F_2) comes to the same level caused by the change in electrostatic potential due to flow of electrons. This electrostatic potential is called the contact potential (ϕ_{12}) and is given by $e\phi_{12} = F_2 - F_1$, where e is the charge of single electron.

For the continuous flow of electron or current, one side temperature must be raised compare to the other side of the junction. The temperature difference across the metals junction unbalanced the Fermi level, as it is unlikely that the two metals will have Fermi levels with identical temperature dependence. Different Fermi energy levels of the two sides caused the flow of electric current until this temperature difference is maintained. To maintain the temperature difference, heat must enter the hot junction and leave the cold junction; this is consistent with the fact that the current can be used to do mechanical work [4].

The electromotive force (emf) generated due thermal gradient at a junction is called the Seebeck effect [5]. The Seebeck effect was originally discovered by Italian scientist Alessandro Volta in 1794, it is named after the Baltic German physicist Thomas Johann Seebeck, who in 1821 independently rediscovered it [5]. It was observed that a closed loop of different metals connected in to two places caused to deflect the compass needle, when a temperature gradient was applied across the junction. The phenomena created was explained in a way that the temperature difference across the junction of the two dissimilar metals caused the electron energy levels to shift differently and hence a potential difference was created and therefore a magnetic field around the wires.

Seebeck did not recognize that there was an electric current involved, so he called the phenomenon "thermomagnetic effect". Danish physicist Hans Christian Ørsted rectified the oversight and coined the term "Thermoelectricity" [6]. The relation for the Seebeck coefficient can be extracted from the modified

Ohm law for the emf, where electric current can be generated even in the absence of voltage difference. The local current density “J” is given by [6]

$$J = \sigma (-\Delta V + E_{emf}),$$

Here V is the local voltage and σ is the local conductivity. In general, the Seebeck effect is expressed by $S = -\Delta V / \Delta T$ where ΔV the voltage difference across the junction and ΔT is the temperature gradient. The Seebeck coefficient of any material is temperature dependent which is varying for each material and its composition.

Another important parameter in Thermoelectricity is the Peltier effect. The Peltier effect is the presence of heating or cooling at an electrified junction of two different conductors and is named after French physicist Jean Charles Athanase Peltier, who discovered it in 1834, [7]. When a current is made to flow through a junction between two conductors, A and B, heat may be generated or removed at the junction. The Peltier heat generated at the junction per unit time is [7]

$$Q = (\Pi_A - \Pi_B) I,$$

where Π_A and Π_B are the Peltier coefficients of conductors A and B, and I is the electric current flow from A to B. The total heat generated is not determined by the Peltier effect alone, as it may also be influenced by Joule heating and thermal gradient effects.

The Peltier coefficients represent how much heat is carried per unit charge. Since charge current must be continuous across a junction, the associated heat flow will develop a discontinuity if Π_A and Π_B are different. The Peltier effect can be

considered as the back-action counterpart to the Seebeck effect if a simple TE circuit is closed. The Seebeck effect will drive a current, which in turn (by the Peltier effect) will always transfer heat from the hot to the cold junction. The close relationship between Peltier and Seebeck effects can be expressed in the direct connection between their coefficients ($\Pi = TS$) the Peltier effect is more important term where the TE generator is used as refrigeration system

The Thomson effect was revealed in 1851 by William Thomson during the study of thermodynamic reasoning to conclude that sources of emf exist in a TE circuit in addition to those located at the junctions [8]. In particular, he predicted that an emf would arise within in a *single* conductor whenever a temperature gradient was present. The Thomson effect can be demonstrated from the schematics in the Fig.3

In this experiment a current pass through an iron rod which is bent into a U-shape [9]. Resistance coils, R_1 and R_2 , are wound about the two sides of the U, as shown. These form two arms of a balanced Wheatstone bridge. The bottom of the U is then heated. This establishes two temperature gradients – a positive one extending from A to C , and a negative one extending from C to B . As a result of this operation, the bridge becomes unbalanced in such a direction as to indicate that the resistance of R_1 has increased more than that of R_2 . Evidently, heat has been liberated at R_1 and absorbed at R_2 .

Absorption of heat is evidence for an emf that is acting in the same direction as that of the current, that is to say, electrical energy is being supplied to the circuit

at the expense of heat energy of the environment. Such is the case in the section AB . Likewise, in the section AC , the current is opposed by an emf, with consequent transformation of electrical energy into heat energy. Thus, in iron, the Thomson emf would give rise to a current *in the iron* from hot to cold regions. Many metals, including bismuth, cobalt, nickel, and platinum, in addition to iron, exhibit this same property, which is referred to as the negative Thomson effect. Another group of metals, including antimony, cadmium, copper, and silver, display a positive Thomson effect; in these, the direction of the Thomson emf is such as to support a current within the metal from cold to hot regions. In one metal, lead, the Thomson effect is zero. In certain metals the effect reverses sign as the temperature is raised or as the crystal structure is altered [9].

2.2 Efficiency and ZT

Schematics of a TE generator are given in the Fig.4. A typical TE generator consists of n -type and p -types materials legs, connected to heat source from one side while to the sink from another side, which is further connected by conducting wire to the load. The temperature of the heat source and sink is represented by T_H and T_C respectively. The heat flow from the source to the sink across the pn-junction caused the current I to flow in the electric circuit. The efficiency of the module can be determined by the output power delivered (p) divided by the heat absorbed (Q_H) from the heat source as given by the expression;

$$\eta = \left(\frac{P}{Q_H} \right) \quad (1)$$

The amount of heat absorbed by the TE module from the heat source Q_H is consists of Seebeck coefficient part and thermal gradient part represented by [4]

$$Q_H = \Delta S T_H I - \frac{I^2 R}{2} + \kappa \Delta T \quad (2)$$

And similarly for the heat exhausted to the sink is given by

$$Q_C = \Delta S T_C I - \frac{I^2 R}{2} + \kappa \Delta T \quad (3)$$

Here the ΔS is the Seebeck coefficient difference between n and p type materials, R is the electrical resistance of the circuit, I is the current and κ is the thermal conductivity.

The P can be further described in term of the difference of the heat absorbed from the heat source and the heat exhausted to the sink.

$$P = Q_H - Q_C = (\Delta S T_H - R I) I - I^2 R_L$$

So that Eq. 1 can be written as

$$\eta = \frac{P}{Q_H} = \frac{R_L S^2 \Delta T / (R + R_L)^2}{\Delta S T_H I - \frac{I^2 R}{2} + \kappa \Delta T} \quad (4)$$

2.3 TE Materials in Use

It is thought that the first TE materials studied were metals, but latter Loffe (1957) found that semiconductors can be a better choice due to high Seebeck coefficient and dominant heat conduction by phonon migration [10]. These days most of the commercialized TE materials are mostly semiconductors compounds or alloys as shown in Fig.5.

Here it can be noticed that each of the TE material performance is co related with operating temperature range. For example, Bi₂Te₃ types TE materials shows

high performance in low temperature range. Similarly, SiGe and type materials show high performance at medium to high temperature range. While Oxide based TE materials are best for very high temperature applications.

Bismuth telluride (Bi_2Te_3) and its alloys are good TE materials below room temperature. Above room temperature the relatively narrow band gap causes mixed conduction due to both electrons and holes [11]. This leads to reduced Seebeck coefficient. Bismuth telluride can be alloyed with Sb_2Te_3 or Bi_2Se_3 , which reduces thermal conductivity considerably. Problems with tellurium arise, since it is scarce, toxic and volatile at high temperatures, therefore, the use of tellurium is limited [12].

Lead telluride (PbTe) was found to have good TE properties at temperatures in the range of 300–700 K. Similar materials are such as PbS and PbSe , which belong to chalcogenides system. Chalcogenide is chemical compound including at least one chalcogen (“ore former”) ion (usually S, Se or Te) and electropositive element [13]. PbTe has high mean atomic weight and a multi-valley band structure. The band gap at 300 K is 0.32 eV, which produces higher Seebeck effect than that of bismuth telluride. Also its TE figure of merit (ZT) is higher when the temperature is raised although it has better lattice thermal conductivity than bismuth telluride [13]. It can be seen from Fig. 6 and 7 that most of the high ZT materials available are consists of elements like Ge, Te, Tl, Pb and Ge which are either expensive or toxic. Alternative chalcogenides materials are ternary chalcogenides like Cu_2SnGe_3 , Cu_2SnS_3 and TE etc. These ternary Chalcogenides compounds have higher degree of freedom compare to binary compound

systems, where we have more room to tune the physical and structural properties. Among These ternary chalcogenides Cu_2SnS_3 is recently found to be a promising choice for TE community due to its similar TE properties with that of the PbTe and consists of nontoxic and low cost elements.

Compass needle

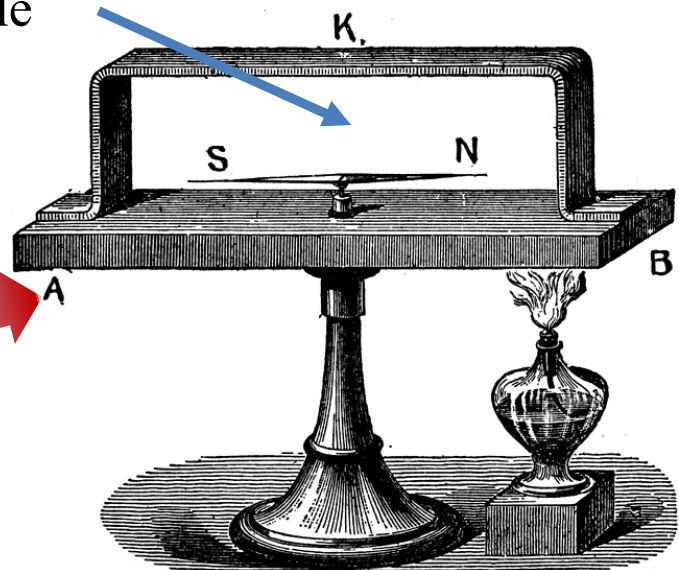


Figure.1, Schematics of Seebeck system used by Thomas Johann Seebeck to discover the Seebeck coefficient [14].

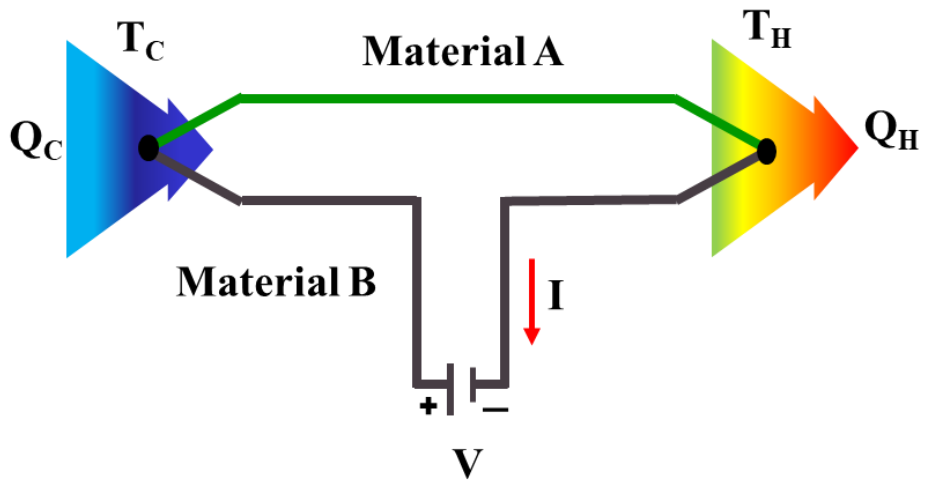


Figure.2, Schematics illustration for Peltier effect

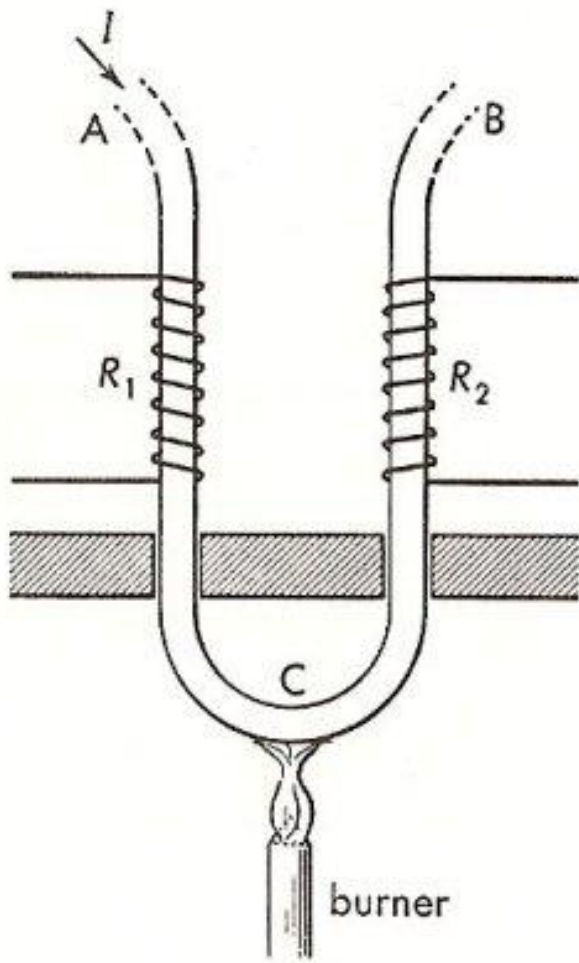


Figure.3, Schematics illustration for Thomson effect [9].

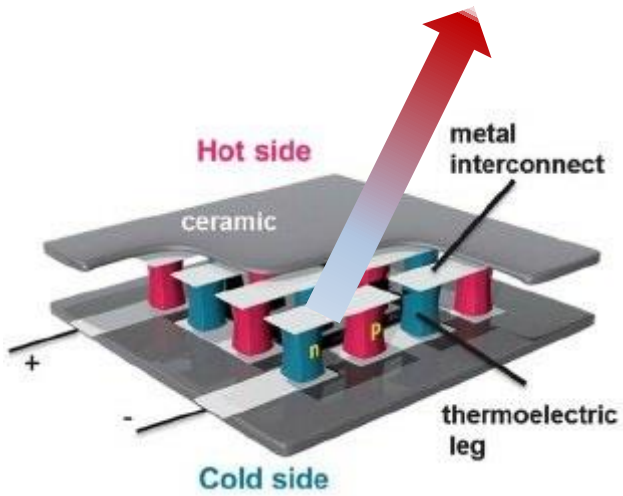
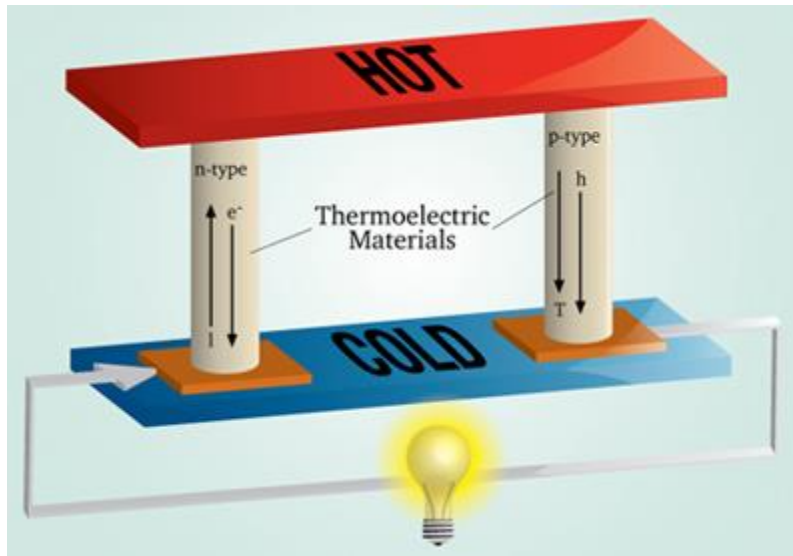


Figure.4, Schematics illustration for TE module [15].

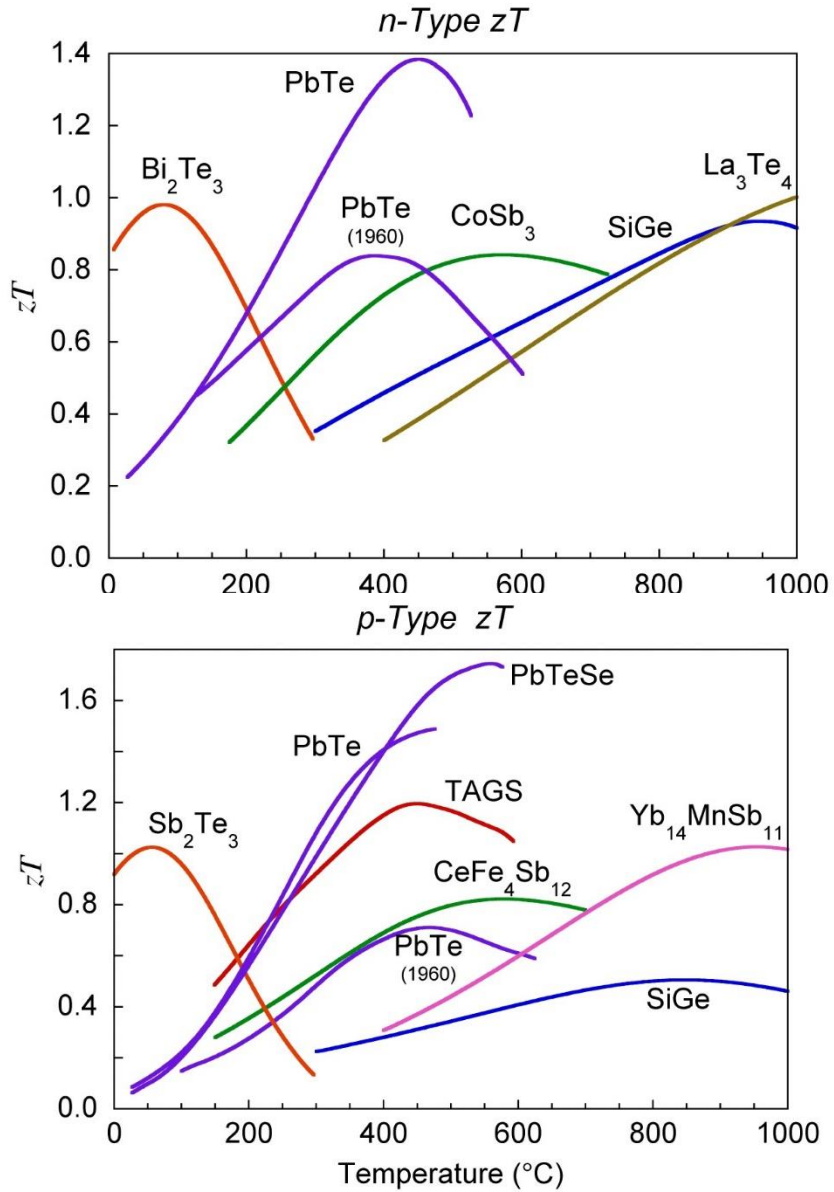


Figure. 5 Temperature-dependent ZT of n - and p - type TE materials used commercially [16].

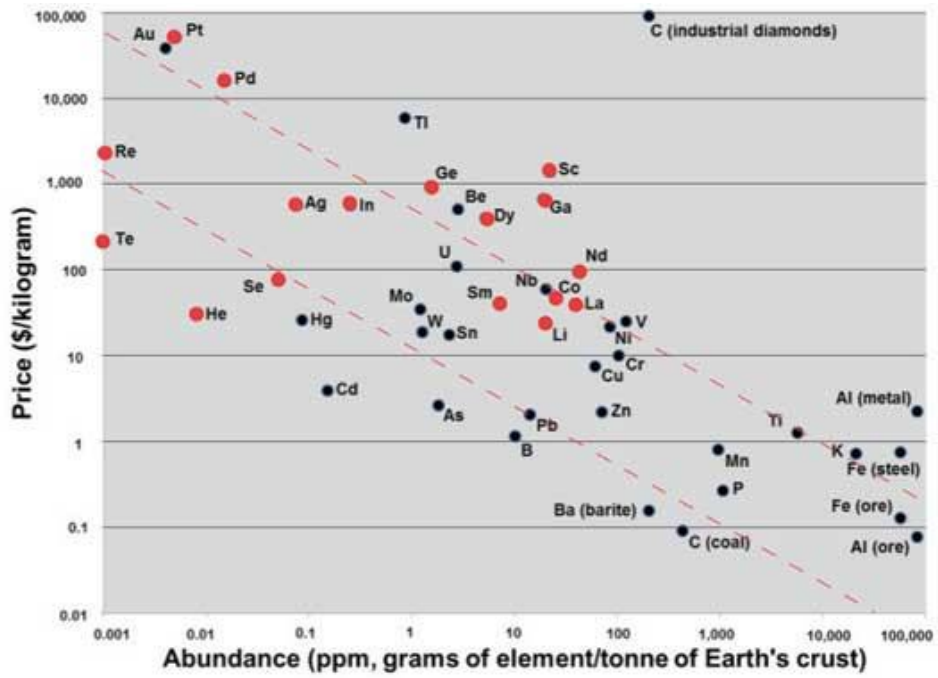


Figure. 6 price and abundance of various elements [17].

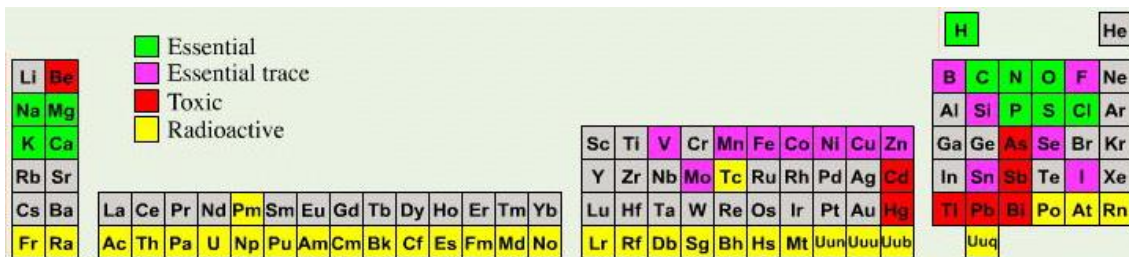


Figure. 7 Toxicity of the elements in the periodic table [18].

2.4 References:

- 1) Eng.fsu.edu. 2002-02-01. Retrieved. A.11 TE effects". (2013).
- 2) Bos, J. -W. " Education in Chemistry." (2012).
- 3) Bubnova, Olga, Crispin, Xavier. . "Towards Polymer-Based Organic Thermoelectric Generators." Energy Environ (2012).
- 4) D. M. Rowe, Thermoelectric's Handbook: Macro to Nano, CRC, Boca Raton, FL (2006).
- 5) French), Peltier . "Nouvelles expériences sur la calorificité des courants électrique" [New experiments on the heat effects of electric currents]. Annales de Chimie et de Physique (in. 56 (1834): 371–86.
- 6) G. A. Slack, D. Rowe. " Crc Handbook of Thermoelectric's." CRC Press (1995).
- 7) GE, Z. H., ZHAO, L. D., WU, D., LIU, X. Y., ZHANG, B. P., LI, J. F. HE, J. Q. . "Low-Cost, Abundant Binary Sulfides as Promising Thermoelectric Materials." Materials Today 19 (2016): 227-39.
- 8) German);, Seebeck "Magnetische Polarisation der Metalle und Erzedurch Temperatur-Differenz" [Magnetic polarization of metals and ores by temperature differences]. Abhandlungen der Königlichen Akademie der Wissenschaften zu Berlin (in. (1822): 265–373.
- 9) https://en.wikipedia.org/wiki/Abundance_of_the_chemical_elements.
- 10) Kittel, Charles. Introduction to Solid State Physics, 7th Edition. Wiley.
- 11) Ltd., A F Ioffe Semiconductor thermo elements and Thermoelectric cooling Infosearch. (
- 12) Price, J. G. "The Society of Economic Geologists Newsletter." 82 (2010).
- 13) Seebeck, Th. J. "Magnetische Polarisation Der Metalle Und Erzedurch Temperatur-Differenz in Ostwald's Klassiker Der Exaktenwissenschaften " 70 (1895): 1822-23.
- 14) Sze, S. M. Physics of Semiconductor Devices, Wiley. (1964).

- 15) Thomson, William "On a Mechanical Theory of Thermo-Electric Currents." Proceedings of the Royal Society of Edinburgh 3 no. 42 (1851): 91–98.
- 16) Thomson, William "On the Dynamical Theory of Heat. Part V. Thermo-Electric Currents." Transactions of the Royal Society of Edinburgh 21 (1854): 123–71.
- 17) WU, H, LI, R. "Properties of Bismuth Telluride Nanomaterials: A Computer Simulation Study." Journal of Nanoelectronics and Optoelectronics 12 (2017): 1199-202.
- 18) WU, H. LI, R. "Properties of Bismuth Telluride Nanomaterials: A Computer Simulation Study." Journal of Nanoelectronics and Optoelectronics 12 (2017): 1199-202.

3 Chapter 3

Review on Cu_2SnSe_3 thermoelectric materials

3.1 General properties of Cu_2SnSe_3

CTSe is a p-type semiconductor with a narrow band gap (~ 1 eV) and can crystallize into a monoclinic (Cc) or cubic (F-43m) phase depending on the processing conditions [1]. Fig.1 shows the cubic and monoclinic structures of CTSe. The structural pattern of monoclinic CTSe is characterized by tetrahedral coordination of atoms. Cu and Sn are each coordinated by four Se atoms, forming a three-dimensional network of corner-sharing MSe_4 tetrahedra (M = Cu or Sn) [2]. Though Cu and Sn are disordered in the cubic CTSe, they are ordered distinctively in the monoclinic variants. A common feature in these monoclinic structures is that one-third of the Se atoms are coordinated by two Cu and two Sn, and two-thirds of the Se atoms are coordinated by three Cu and one Sn. In this way the Cu_3Sn and Cu_2Sn_2 coordination around Se are two environments satisfying the octet rule. While the Cubic CTSe is high temperature phase where Cu and Sn atoms share the same lattice sites and form disordered structure with high symmetry [3].

Sn orbitals have a small effect on carrier transport, and Cu-Se atoms form carrier conductive bond network which determines electrical conductivity. Therefore, it is possible to control the TE properties of CTSe by doping on the Sn site. It can increase the effective mass to achieve high Seebeck coefficient while preserving 3D conductive framework as electron-crystal like structure [4]. Reports are present on the control of TE properties of CTSe, by substitution, doping and solid solution [5, 6].

3.2 Phase studies of Cu_2SnSe_3

Previous studies reported that CTSe can be found in various allotropic forms, which include orthorhombic, monoclinic and cubic structures [1, 7]. Phase transformation in solid state compounds involves rearrangement of atoms, which can be induced by the change of temperature, pressure and/or

composition. It is important to understand the thermodynamic conditions of these diverse phases since different synthesis conditions and stoichiometry can lead to the formation of different phases. Phase transitions can lead to different band gap and lattice parameters, which can further affect the physical properties.

The type of phases present at specific temperature is controversial for CTSe, due to the disagreements found in previous reports. Studies of Palantnik et al. [8] and Sharma et al. [9] reported that this compound crystallizes in sphalerite-type cubic structure with unit cell parameter ranging from $a = 5.688$ to 5.696 Å. Debye-Scherrer powder analyses of Rivet et al. [10] indicated that CTSe has an orthorhombic structure at 450 °C. On the other hand, XRD analyses of Marcano et al.¹⁶ proposed a monoclinic structure for CTSe with lattice parameters $a = 6.5936$ Å, $b = 12.1593$ Å, $c = 6.6084$ Å and $\beta = 108.56$ Å. Different compositions and synthesis parameters can lead to diverse results. Previous reports are lacking in providing specific composition, temperature and detailed TE characterization of CTSe phases. Recently Fan et al. [11] used single crystal electron diffraction and high resolution synchrotron X-ray powder diffraction with Reitveld refinement to study the different crystal structures of the CTSe. Fan et al. further studied the structure of the CTSe samples water quenched from 850 K and 950 K, and found that it has monoclinic and cubic phase structures

3.3 TE studies on Cu_2SnSe_3

Lu and Morelli have reported low temperature TE properties of Mn doped CTSe in the temperature range of 100 to 300 K and a maximum value ZT of about 0.035 (at 300 K) has been observed for the sample $\text{Cu}_2\text{Sn}_{0.08}\text{Mn}_{0.02}\text{Se}_3$ [12]. Shi et al. have studied the TE properties of In doped CTSe in the temperature range 300 to 900 K and a maximum $ZT = 1.14$ has been observed for the sample $\text{Cu}_2\text{Sn}_{0.9}\text{In}_{0.1}\text{Se}_3$ at 850 K [13]. Fan et al. have studied the TE properties of Ga doped CTSe in the temperature range of 300 to 700 K [14]. In their communication they have compared the ZT of the samples prepared by hot-pressing and spark plasma sintering and they have concluded that the hot-pressed sample $\text{Cu}_2\text{Ga}_{0.075}\text{Sn}_{0.925}\text{Se}_3$ has the highest ZT value at 700 K.

3.4 Approaches for ZT improvement of Cu_2SnSe_3

The improvements of ZT of chalcogenides and silicides, using various approaches which include nano-structuring, doping and alloying, were reported [5, 6]. Alloying of compounds can result in disorder and lattice distortion, which can enhance the phonon scattering and decrease the thermal conductivity. Optimum doping in composites can also increase the effective mass of the system which can lead to enhanced Seebeck coefficient [15]. Composites and alloys can have inclusions and grain boundary interfaces, which can block the low energy phonon without affecting the electronic carrier transport properties. Hence low thermal conductivity is expected along with reasonable electrical conductivity. This approach is an efficient way to optimize electrical and thermal transport properties to improve TE efficiency. Alloying can also lead to point defect scattering, which can reduce the lattice thermal conductivity, which in turn can help improve ZT of the alloy systems compared to the pristine compounds. It is a big challenge to decouple Seebeck coefficient and electrical properties in alloying and composites. Increasing one value will lead to compromise another. To address this, issue recent reports the solid solution and reported that Seebeck can be controlled with affecting largely the electrical conductivity [16]. Thus solid solution can be one of the promising approaches to control the Seebeck coefficient, thermal and electrical properties of CTSe. Finally making thin films and 2D structures of the CTSe can be another way to explore the its commercial potential due to its higher power density, light weight and compact size. Due to high conductive nature of the CTSe it is expected that the CTSe thin film can give us much better TE properties compare to thin films of conventional TE compounds like SnSe, due to incorporation of defects during thin film deposition.

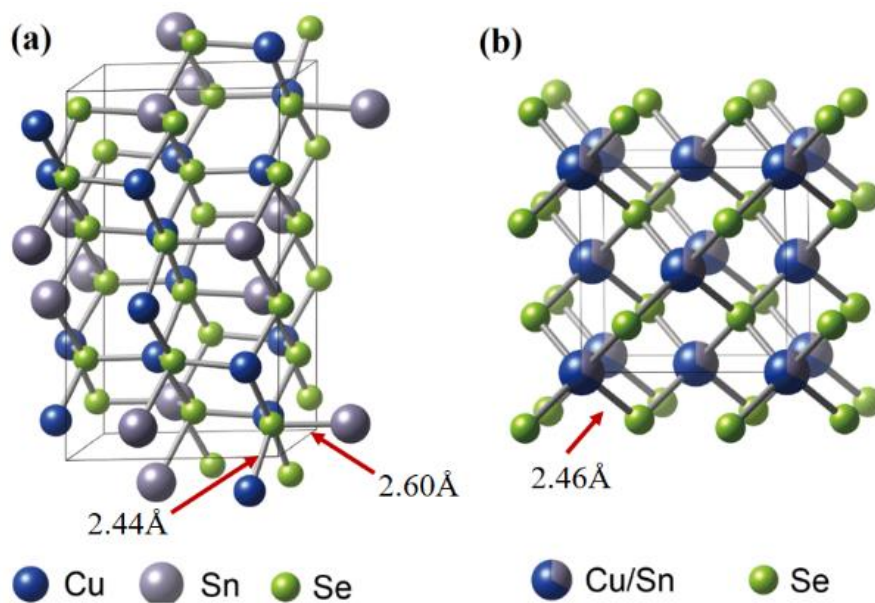


Figure. 1 Structure of (a) monoclinic and (b) cubic CTSe, simulated from the Rietveld data files of the two samples. The arrows show the bond lengths between the corresponding atoms. The bond length between Cu and Se is slightly larger for the monoclinic phase than that of the cubic structure. The mixed site occupancy of the Cu and Sn atoms is indicated by partial coloring of the corresponding atoms in (b).

3.5 References:

- 1) J. Fan, H. L. Liu, X. Y. Shi, S. Q. Bai, X. Shi and L. D. Chen, *Acta Mater*, 2013, **61**, 4297-4304.
- 2) J. J. Wang and K. M. Ryan, *Crystengcomm*, 2016, **18**, 3161-3169.
- 3) Siyar, M., J. Y. Cho, Y. Youn, S. Han, M. Kim, S. H. Bae, and C. Park. *Journal of Materials Chemistry C* 6, no. 7 (Feb 21 2018)
- 4) X. Y. Shi, L. L. Xi, J. Fan, W. Q. Zhang and L. D. Chen, *Chem Mater*, 2010, **22**, 6029-6031.
- 5) Y. Y. Li, G. H. Liu, J. T. Li, K. X. Chen, G. He, Z. C. Yang, Y. M. Han, M. Zhou and L. F. Li, *Mater ChemPhys*, 2016, **177**, 398-404.
- 6) S. Singh, M. Brandon, P. Liu, F. Laffir, W. Redington and K. M. Ryan, *Chem Mater*, 2016, **28**, 5055-5062.
- 7) J. Fan, W. Schnelle, I. Antonyshyn, I. Veremchuk, W. Carrillo-Cabrera, X. Shi, Y. Grin and L. D. Chen, *Dalton T*, 2014, **43**, 16788-16794.
- 8) L. S. Palatnik, V. M. Koshkin, L. P. Galchinetskii, V. I. Kolesnikov and Y. F. Komnik, *Soviet Physics-Solid State*, 1962, **4**, 1052-1053.
- 9) B. B. Sharma, R. Ayyar and H. Singh, *Phys Status Solidi A*, 1977, **40**, 691-696.
- 10) J. Rivet, *Ann Chim France*, 1965, **10**, 243.
- 11) J. Fan, W. Carrillo-Cabrera, L. Akselrud, I. Antonyshyn, L. D. Chen and Y. Grin, *InorgChem*, 2013, **52**, 11067-11074.
- 12) *Journal of Electronic Materials*, .41, No. 6, 2012
- 13) *Adv. Funct. Mater.* 2016, 26, 6025–6032
- 14) *Acta Materialia* Volume 61, Issue 11, June 2013, Pages 4297–4304
- 15) Chauhan, N. S., A. Bhardwaj, T. D. Senguttuvan, R. P. Pant, R. C. Mallikd, and D. K. Misra. *Journal of Materials Chemistry C* 4, no. 24 (2016): 5766-78.
- 16) *Journal of Alloys and Compounds* 506 (2010) 18–21

4 Chapter 4

Effect of annealing temperature on the phase transition, band gap and thermoelectric properties of Cu_2SnSe_3 .

4.1 Introduction

TE energy harvesting is one of the approaches to address the global environmental challenges, utilizing waste heat for useful electric power generation. This technology recently attracted attention of the commercial sectors, due to the possible applications of TE materials in wearable electronic devices, solid state Peltier cooling, remote area sensors, etc.[1-3]. Currently available commercial TE materials such as Bi_2Te_3 , Sb_2Te_3 and PbTe consist of either toxic or expensive elements [4, 5]. Therefore, exploration of TE materials with less toxic, less expensive and more earth-abundant elements, is the focus of the TE community these days. The ternary chalcogenide CTSe is expected to be one of these auspicious TE materials, owning large flexibility to tune its physical and electronic properties [6]. The elements of CTSe are less toxic, abundant in nature and relatively cheap compared to Te and Pb.

In the structure of CTSe, Sn orbitals have a small effect on carrier transport, and Cu-Se atoms form carrier conductive bond network which determines electrical conductivity. Therefore, it is possible to control the TE properties of CTSe by doping on the Sn site. It can increase the effective mass to achieve high Seebeck coefficient while preserving 3D conductive framework as electron-crystal like structure [7]. Reports are present on the control of TE properties of CTSe, by substitution, doping and solid solution [8, 9]. The dimensionless figure of merit (ZT) of ~ 1.2 was reported by Li et al. in In-doped CTSe compound at 850 K [10]. Previous studies reported that CTSe can be found in various allotropic forms, which include orthorhombic, monoclinic and cubic structures [11, 12]. Phase transformation in solid state compounds involves rearrangement of atoms, which can be induced by the change of temperature, pressure and/or

composition. It is important to understand the thermodynamic conditions of these diverse phases since different synthesis conditions and stoichiometry can lead to the formation of different phases. Phase transitions can lead to different band gap and lattice parameters, which can further affect the physical properties.

The type of phases present at specific temperature is controversial for CTSe, due to the disagreements found in previous reports. Studies of Palantnik et al.[13] and Sharma et al.[14] reported that this compound crystallizes in sphalerite-type cubic structure with unit cell parameter ranging from $a = 5.688$ to 5.696 Å. Debye-Scherrer powder analyses of Rivet et al.[15] indicated that CTSe has an orthorhombic structure at 450 °C. On the other hand, XRD analyses of Marcano et al.[16] proposed a monoclinic structure for CTSe with lattice parameters $a = 6.5936$ Å, $b = 12.1593$ Å, $c = 6.6084$ Å and $\beta = 108.56$ Å. Different compositions and synthesis parameters can lead to diverse results. Previous reports are lacking in providing specific composition, temperature and detailed TE characterization of CTSe phases. Recently Fan et al. [17] used single crystal electron diffraction and high resolution synchrotron X-ray powder diffraction with Reitveld refinement to study the different crystal structures of the CTSe. Fan et al. further studied the structure of the CTSe samples water quenched from 850 K and 950 K, and found that it has monoclinic and cubic phase structures respectively, but phase studies at temperatures lower than 800 K were not carried out. Further, the TE properties of the monoclinic phase CTSe were studied, but those of high temperature cubic phase have not been reported.

In this work, we performed phase studies using XRD on the CTSe samples, solidified from the melt at 1280 K, annealed at different temperatures and subsequently water quenched. Rietveld refinements were used to obtain the quantitative phase information. Differentiation of the different phase structures was further confirmed by Raman spectroscopy analyses, and the TE properties of both the high and low temperature phases were compared in the temperature range of 300 to 600 K.

4.2 Experimental procedure

4.2.1 Sample preparation:

Polycrystalline CTSe sample was synthesized from direct reaction of the stoichiometric amount of Cu 99.99 %, Sn 99.99 %, and Se 99.99 % powders (Kunjundo Chemicals, Japan). As-received powders were melted in a pre-evacuated quartz ampoule at 1280 K for 3 hours followed by periodic agitation to improve mixing of the reacting species. The molten sample was cooled at a rate of 1 K/min down to 720 K and 820 K, annealed for 12 hours at these temperatures and quenched in water to cease further phase changes.

In order to study phase transformation at higher temperatures, a molten sample was cooled to 960 K, annealed for 12 hours and quenched in water. The ingots were ground to fine powder using an agate mortar-pestle, and the obtained powder samples were named hereafter M-720, M-820 and C-960 respectively. The powder samples were spark-plasma-sintered (SPSed) at 673 K under the applied pressure of 60 MPa for 5 minutes. SPSed samples from M-720, M-820 and C-960 powders were named SM-720, SM-820 and SC-960, respectively. The consolidated samples were disc-shape pellets of 3 mm in height with 12.5 mm diameter.

4.2.2 Characterization:

Phase studies were performed on the pellet samples, using powder X-ray diffraction (XRD) D-8 Advance (Bruker, Germany), with copper K α radiation of $\lambda = 1.54 \text{ \AA}$. Rietveld refinement (TOPAS) was used for the quantitative phase analyses of the samples. The atomic displacement, fractional coordinates and occupancies of the elements which were obtained from the standard XRD database were used without refining. Raman scattering analyses were performed on the pellet samples using LabRAM Raman spectrometer (HORIBA Scientific). The He-Ne laser source with wavelength of 532 nm was used as the exciting light. The LabRAM spectrometer is equipped with both macroanalysis and microanalysis configurations. The laser beam of mm order spot size was focused on the sample surface using an optical input focusing macroanalysis system. The incident laser beam was further focused to 1 μm spot size using optical

microscope ($\times 50$ objective) in microanalysis system. All the measurements were performed in the range of 50 to 400 (cm^{-1}) Raman shift at ambient temperature.

The Seebeck coefficient and the electrical resistivity were measured in the temperature range of 300 to 600 K, using commercial TE property measurement system, (SEPEL, TEP-800). The measurements were carried out in Ar atmosphere to prevent the oxidation of the SPSe samples.

Laser flash technique (LFA, Netzsch, LFA 457) was used to measure the thermal diffusivity (D) of carbon coated disc-shape samples with thickness < 1 mm, in the temperature range of 300 to 600 K in the inert atmosphere. Differential scanning calorimetry (DSC) was used to measure the specific heat (C_p) in the same temperature range as D . The samples were put in an alumina crucible in Ar atmosphere, and the DSC curve was recorded with a heating rate of 10 K/min. Thermal conductivity (k) was calculated from $k = C_p \cdot d \cdot D$, where C_p , d and D are specific heat obtained from DSC, density and thermal diffusivity, respectively. The densities of the pellet samples were measured using Archimedes' principle at room temperature in ethanol medium. Hall effect measurements of carrier concentration (p_H) and mobility (μ_H) on square-shape samples with thickness < 1 mm, were performed in Van der-Pauw configuration at room temperature with 0.56 T applied magnetic field.

Ultraviolet-visible (UV-Vis) spectroscopy analyses were performed on the polycrystalline powder samples, dispersed in ethanol, using UV-Vis/NIR Spectrometer (JASCO, V-770). The optical absorption spectra were obtained in the wavelength range of 600 to 1000 nm, with a step size of 0.5 nm.

DOS analyses and electronic band structure calculations were carried out for SM-820 and SC-960 samples using the atomic positions and lattice parameters obtained from the Rietveld analysis of each sample. We performed first-principles calculations using Vienna ab-initio simulation package (VASP) based on the density functional theory (DFT) [18]. The hybrid functional method based on the HSE06 [19] was employed for the exchange-correlation energy because of the band-gap underestimation in the conventional GGA scheme [20]. The fraction of exact exchange energy we used was 0.25. The cut-off energy for the plane wave basis was set to 250 eV. In the crystal structure of cubic CTSe, Cu and Sn atoms randomly occupy the same crystallographic site. To examine the influence of the site

disorder on the electronic structure, we simulated three configurations where the Cu and Sn sites are distributed differently.

4.3 Results and Discussions

4.3.1 Phase analysis

The X-ray diffraction (XRD) patterns of CTSe powder samples annealed at 720 K (M-720), 820 K (M-820) and 960 K (C-960) and those of samples SPSed at 670 K for 5 minutes (SM-720, SM-820 and SC-960) are shown in Fig. S1 (ESI[†]) and Fig. 1 (a) respectively. Fig. 1(b) shows the log scale XRD patterns of the SPSed samples in the range of 28 to 43 degree 2θ . Fig. S1 (ESI[†]) and Fig. 1 (a) show that the XRD spectra were remain the same before and after SPS sintering, hence the phases of the CTSe samples were not affected by SPS process. The XRD pattern in Fig. 1(a), shows that CTSe sample annealed at 960 K crystallizes in a cubic sphalerite type structure, represented by only the major peaks at 27.1, 45.0, 53.3 and 65.6 degrees 2θ . Low intensity peak of the SC-960 shown in Fig. 1(b) around 30 degree 2θ , is attributed to the minor monoclinic phase, formed during water quenching. The other two samples, annealed at 820 and 720 K, are found to have mostly monoclinic structures. Since these CTSe allotropes are derived from the cubic sphalerite structure [21], the XRD peaks with high intensities for all these phases are almost the same. Monoclinic phase of the CTSe can be distinguished from the cubic phase by the presence of several peaks with very low intensities mostly between 28 to 43 degrees 2θ (Fig. 1(a)).

These experimental XRD spectra were analyzed further by Reitveld refinement using TOPAS to distinguish quantitatively the minor phases which can exist along with the parent phase. The results are shown in Fig. 2. The atomic positions, occupancies and thermal parameters of the PDF cards 04-002-6015 and 04-012-4693 for cubic and monoclinic structures, respectively, were used as an initial model for the refinement. The weighted pattern R-value (Rwp) for all the samples were ~ 10 , which we think is acceptable, with major peaks overlapping for different allotropic forms of CTSe.

We found that it is very difficult to synthesize a pure phase CTSe at both low and high temperatures. The amount of cubic phase increases with increasing annealing temperature, and at high enough temperature mostly cubic phase

exists, which agrees well with the previous reports^{11,17}. The samples annealed at 720 and 820 K consist of major monoclinic phase with minor cubic phase (2~11 %) still present. This means that either the annealing time was not long enough to complete the high to low temperature phase transition or some local difference in composition of CTSe crystallites lead to different phases. Similarly, the major phase of the sample annealed at high temperature (960 K), was cubic.

Fig. 3, shows the crystal structures of both (a) monoclinic and (b) cubic phases of CTSe. Monoclinic phase is a low temperature, less symmetric and ordered structure of CTSe, where all the atoms are tetrahedrally coordinated. Sn and Cu bonded with four Se atoms are forming three dimensional (Cu/Sn)-Se₄, corner shared 3D network. Se atoms are coordinated by one Sn and three Cu atoms, with bond length of Sn-Se~2.60 Å and Cu-Se~2.44 Å as shown in Fig. 3 (a). Cu and Sn are disordered in cubic structure with a variety of possible cation coordination pattern around the Se anion like Cu₄, Cu₃Sn, Cu₂Sn₂, CuSn₃, and Sn₄ [22].

We assumed order-disorder transition for these allotropic transformations, where slight lattice re-arrangement can result in small atomic displacement from monoclinic (space group 9(Cc)) to cubic (space group 216(F4̄3m)) at high temperature. In such types of phase transitions of CTSe, the cubic to monoclinic transition is characterized by the presence of low intensity peaks in the XRD pattern, while the major reflections of (111), (022), (133) and (044) are not much differed [23, 24].

Raman spectroscopy analyses were performed on the SM-820 and SC-960 samples in order to further confirm monoclinic to cubic phase transition at high temperature. The Raman spectra of the two samples, recorded in the range of 40~400 cm⁻¹, are shown in Fig. 4. Raman shifts of the two samples in the present work are compared with those reported in the literature, and the results are listed in Table 1, where the possible symmetries are also assigned. Kroumov et al.[25] performed factor group analysis for the various zone-center lattice vibrational modes of monoclinic CTSe structure, with 3 Se, 1 Sn and 2 Cu atoms in 4(a) Wyckoff positions [26], and argued that six Raman active modes, represented by 3A'+3A'' are possible for this compound (Table 1). The data obtained from the Raman peaks of the monoclinic structure, agree well with both the calculated symmetry modes as well as those from the literature, indicated by six Raman shifts observed at 69, 176, 203, 230, 243 and 270 cm⁻¹.

The high intensity peak, observed at 176 cm⁻¹ in all the CTSe phases is attributed to the strongest A' mode which resulted from the vibration of the Se-Cu bond, while Sn remains at rest. A broad vibrational band at ~ 360 cm⁻¹ was reported [27] as an overtone of the strong peak at 176 cm⁻¹. In the high temperature cubic phase, only one intensive peak shift at 176 cm⁻¹ and two small intensity peaks at 193 and 225 cm⁻¹ are observed. The absence of the peaks at 203, 230 and 243 cm⁻¹ in the cubic phase confirms the phase transition, where these modes of lattice vibrations are lost in Raman scattering due to the increase in structural symmetry [28].

In the cubic phase, the bond stretching force is small compared to the monoclinic ordered phase, due to the smaller bond length of Sn-Se in the cubic phase as shown in Fig. 3. This can lead to the decrease in Raman shift due to slight reduction in phonon energies, which was illustrated by Marcano et al.[21]. Slight peak shifting towards lower Raman frequencies of ~10 cm⁻¹ for cubic structure is in agreement with the fact that high temperature phase of CTSe has disordered and more symmetric lattice structure. Finally, the major Raman peak at 176 cm⁻¹ is the same for both the CTSe phases, which can be attributed to the Cu-Se bond vibration, since bond length is almost the same (~2.44 & 2.46 Å) in both compounds. From the XRD and Raman spectroscopy measurements, we conclude that CTSe can be found in monoclinic structure as a major phase at temperature 820K and below, while it has mostly cubic disordered structure at higher temperatures. Secondary phases like orthorhombic and tetragonal phases were not observed in this study.

4.3.2 Electronic transport properties

Annealing at high temperature can cause phase transition and result in various electronic structures, since band gap is reduced with the increase in annealing temperature, which can be characterized by UV-Vis spectroscopy analysis. The dependence of energy band gap (E_g) on the absorption coefficient (α) for the direct band transition is given by the relation [29]

$$\alpha hv = A(hv - E_g)^{1/2} \quad (1)$$

where A , h and v are a constant, the Planck's constant and the frequency of radiation, respectively. Fig. S2 (ESI†) shows the optical absorption spectra obtained from the UV-Vis spectroscopy for the SM-820 and SC-960 powder samples dispersed in ethanol at room temperature. The calculated values of hv

and $(ah\nu)^2$ are plotted in Fig. 5 for the (a) monoclinic and (b) cubic structures. The optical band gaps were obtained from the extrapolation of the linear region of the plot to the $h\nu$ axis, which were found to be 0.9 eV and 1.0 eV for the monoclinic and cubic phase respectively. The values of the direct band gaps of the CTSe reported previously lie in the range of 0.3 to 1.3 eV [16, 30, 31], which is in agreement with the results in this study.

To further study the changes in band structure accompanying the phase transition, we studied the density of states (DOS) and band structures of the samples SM-820 and SC-960. To further study the changes in the band structure accompanying the phase transition, we studied the density of states (DOS) and band structures of the cubic and monoclinic CTSe. The structure information of the major phase from the Rietveld refinement of the samples SM-820 and SC-960, were used for the calculation. Fig. 6 (a) and 7 (a) show the band structures of the monoclinic and cubic phases. In the monoclinic phase, the conduction band (CB) minima and the valence band (VB) maxima are separated clearly at the point Γ . The band gap of 0.58 eV is consistent with the experimental observation. On the contrary, in the cubic structure, the metallic band structure is observed. The change of band gap according to the phase transition was reported for other phase variant structures like MTe₂ (M = Mo and W) [32] and ZnS [33]. Fig. 6 (b) and 7(b) show that the VB maxima is mainly contributed by Se-p and Cu-d orbital hybridization in the VB, while the major part of the CB minima is occupied by Sn-s and Se-p hybridized orbitals. The orbital character of VB indicates that Cu-Se bonding network plays the dominant role in the hole transport of the p-type CTSe. On the other hand, Sn atoms do not contribute to the hole conduction but provide extra electrons to the whole lattice⁷.

Fig. S3 (ESI⁺) shows (a) hole concentration and (b) carrier mobility of SM-820 (square points) and SC-960 (circle points), measured at room temperature. The DFT results are also consistent with the results in Fig. S2 (ESI⁺), where the carrier concentration in the cubic phase is higher than that of the monoclinic phase. The variation in the band gap (E_g) of heavily doped semiconductors like CTSe can be governed by Burstein-Moss effect [34], where conduction band comes closer towards the Fermi energy level (E_F), due to the increase in carrier concentration.

The relation between the carrier concentration and band gap is given as [35]

$$n_i = CT^{3/2} \exp\left(\frac{-E_g}{2k_B T}\right) \quad (2)$$

where C , T , k_B , n_i and E_g are a constant, the absolute temperature, the Boltzmann constant, the carrier concentration and the band gap, respectively. The carrier concentration is exponentially proportional to the negative of the band gap, which means that band gap narrowing leads to the increase of the carrier concentration. Thus, the band gap reduction of cubic phase compared to the monoclinic phase can result in the major increase of carrier concentration.

Moreover, electrical conductivities of both the CTSe phases are reduced with increasing temperature, which is a common behavior for heavily doped degenerate semiconductors [36]. Here the Se loss resulting from the high temperature treatment can lead to the increase of the hole concentration, which in turn, can increase the electrical conductivity. These results are in good agreement with the results of band gap analyses and the hall measurements discussed above.

TE properties

Fig. 8 shows the TE properties measured in the temperature range of 300 K to 600 K. The Seebeck coefficients of both monoclinic and cubic phase have linear relationship with temperature, which validates the degenerate behavior shown in Fig. 8 (b). The Seebeck coefficients of the monoclinic phase which is larger than those of cubic CTSe phase, can be explained using the mobility of majority carriers. Sun et al. [37] studied the effect of mobility, charge relaxation (τ) and carrier potential on the Seebeck coefficient, where they included the effect of asymmetric charge relaxation ($S\tau$) in the Mott expression. The expression describes the Seebeck coefficient in the form of two factors, $S\tau$ (asymmetric charge relaxation) and S_N (conventional contribution),

$$S = S\tau + S_N = -\frac{\pi^2 k_B^2 T}{3} \frac{1}{2} \left[\frac{\partial \ln \tau}{\partial \varepsilon} \right]_{EF} - \frac{\pi^2 k_B^2 T}{3} \frac{1}{2} \left[\frac{\partial \ln N}{\partial \varepsilon} \right]_{EF'} \quad (3)$$

$S\tau$ can be further related to the Nernst coefficient,

$$\nu = -\frac{\pi^2 k_B^2 T}{3 B |e|} \left[\frac{\partial \tan \theta_H}{\partial \varepsilon} \right]_{\varepsilon F'} \quad (4)$$

by $\nu \cdot B = \pm S \tau \tan \theta_H$, where ε is energy function, $\varepsilon F'$ is Fermi level, $\tan \theta_H$ is tangent of the Hall angle and B is magnetic field. Nernst coefficient weakly depends on ordinary scattering processes, but has pronounced dependency on charge relaxation events. ν can be further expressed in terms of either charge mobility μ or τ , since $\tan \theta_H = eB\tau/m^* = \mu B$. We assume that the effect of S_N on the Seebeck is not prominent, as the stoichiometric composition of the samples used in this study is supposed to be unchanged but only the structures are slightly varied. Fig. S3 (b) (ESI[†]) shows that carrier mobility of monoclinic phase at room temperature is higher than that of cubic phase. This enhanced mobility in ordered structure can be related to the carrier concentration which is smaller than that of disordered structure, which is already discussed in the electronic structure study. From Nernst and charge relaxation expressions, it can be apparently seen that the Seebeck coefficient has direct physical link with the charge mobility, while Seebeck is further increased with increasing temperature. Moreover, the Seebeck coefficient measured at 600 K in this study is smaller than 100 $\mu\text{V/K}$ for both SM-820 and SC-960 samples, which is lower than the recently reported 120 $\mu\text{V/K}$ by Li, et al.[10] and 200 $\mu\text{V/K}$ by Liu, et al. [38]. High carrier concentration can lead to large carrier scattering, which can result in the decrease of carrier mobility and Seebeck coefficient.

The dimensionless figure of merit (ZT), calculated from electrical conductivity, Seebeck coefficient and thermal conductivity is given in Fig. 8 (d). ZT s for both the phases (SM-820 and SC-960) show linear increase with temperature. The sample SC-960 (mostly cubic phase) shows the ZT of 0.09 at 600 K, which is comparable with the recently reported value (~ 0.1) for the undoped CTSe [10]. The TE performance of cubic CTSe which is higher than that of monoclinic phase, can be attributed to the increase in electrical conductivity due to the reduction of the band gap. The contributions of both the thermal conductivity and the Seebeck coefficient to the ZT in the cubic phase are not large enough to synergistically balance the increase in electrical conductivity. Hence the power factor of the cubic phase ($0.24 \text{ mWm}^{-1}\text{K}^{-2}$) was higher than that of the monoclinic phase ($0.096 \text{ mWm}^{-1}\text{K}^{-2}$) at 600 K, but the change of thermal conductivity was not significant

The thermal conductivity results are shown in Fig. 8 (c), where both the phases have nearly the same values, which are decreased with temperature in a similar way. To find the reason of the large difference in electrical conductivity and similar thermal conductivity of the monoclinic and cubic phases, we splitted the whole thermal conductivity into the electronic part (K_e) and the lattice part (K_L). Wiedemann-Franz law [39] ($K_e = L\sigma T$, where L is the Lorenz number) was employed to determine K_e in the temperature range of 300 to 600 K. In the above relationship, it is crucial to determine the value of L before going into further calculations.

Typically for the metallic elements, free-electron model [40] is employed, using:

$$L_o = \frac{\pi^2}{3} \left(\frac{K_B}{e} \right)^2, \quad (5)$$

where K_B is Boltzmann constant and e is charge of electron. The L_o value obtained from eq. (5) is $\sim 2.45 \times 10^{-8} \text{ W}\Omega\text{K}^{-2}$, which is used to calculate K_e for the metals. However, for the heavily doped degenerate semiconductors like CTSe, chemical potential is strongly dependent on the temperature, hence the Lorentz number does not remain the same for the whole temperature range. Using the single value of the Lorentz number would underestimate the lattice thermal conductivity. The true value of L depends on the reduced Fermi energy η ($=E_F/K_B T$) and the acoustic phonon scattering parameter λ . The corresponding equation for calculating L is [41]:

$$L = \left(\frac{K_B}{e} \right)^2 \frac{(1+\lambda)(3+\lambda)F_\lambda(\eta)F_{\lambda+2}(\eta) - (2+\lambda)^2 F(\eta)^2_{\lambda+1}}{(1+\lambda)^2 F(\eta)^2_\lambda}, \quad (6)$$

where $\lambda=0$ for the acoustic phonon scattering. The fermi integrals ($F_m(\eta)$) were measured from the experimental Seebeck coefficients, using the simple parabolic band model:

$$S = \left(\frac{K_B}{e} \right) \left(\frac{2F_1(\eta)}{F_0(\eta)} - \eta \right) \quad (7)$$

The detailed calculation procedure can be found in the [41, 42]. The calculated Lorenz numbers are shown in Fig. S4 (a) (ESI+). Using these L values, we calculated the corresponding electronic part of thermal conductivity and then subtracted it from the total thermal conductivity to get the lattice thermal conductivity for each of the sample, which is shown in Fig. S4 (b) and (c) (ESI+).

It can be seen from Fig. S4 (ESI+) that the electronic conductivities are very different, while lattice parts of the thermal conductivities are nearly the same for the sample SM-820 and SC-960. It means that the lattice vibration has negligible

role in the increase of total thermal conductivity of the SM-820, since the major effect comes from the different electronic thermal conductivities. Further, the lower lattice thermal conductivity of the SC-960 in Fig. S4 (b) (ESI[†]) reveals that it has large phonon scattering due to disordered lattice structure. Monoclinic to cubic phase transition results in the increase of crystal symmetry and disorder, which leads to the increase of phonon scattering of the cubic phase. Loss of crystal symmetry due to order-disorder transition was reported by Richardson et al, [43] while its effect on the phonon scattering and thermal conductivity was recently explored [44, 45]. Presence of the mixed phases in both the samples provide an extra scattering factor to reduce the total thermal conductivity, which is favorable for higher ZT.

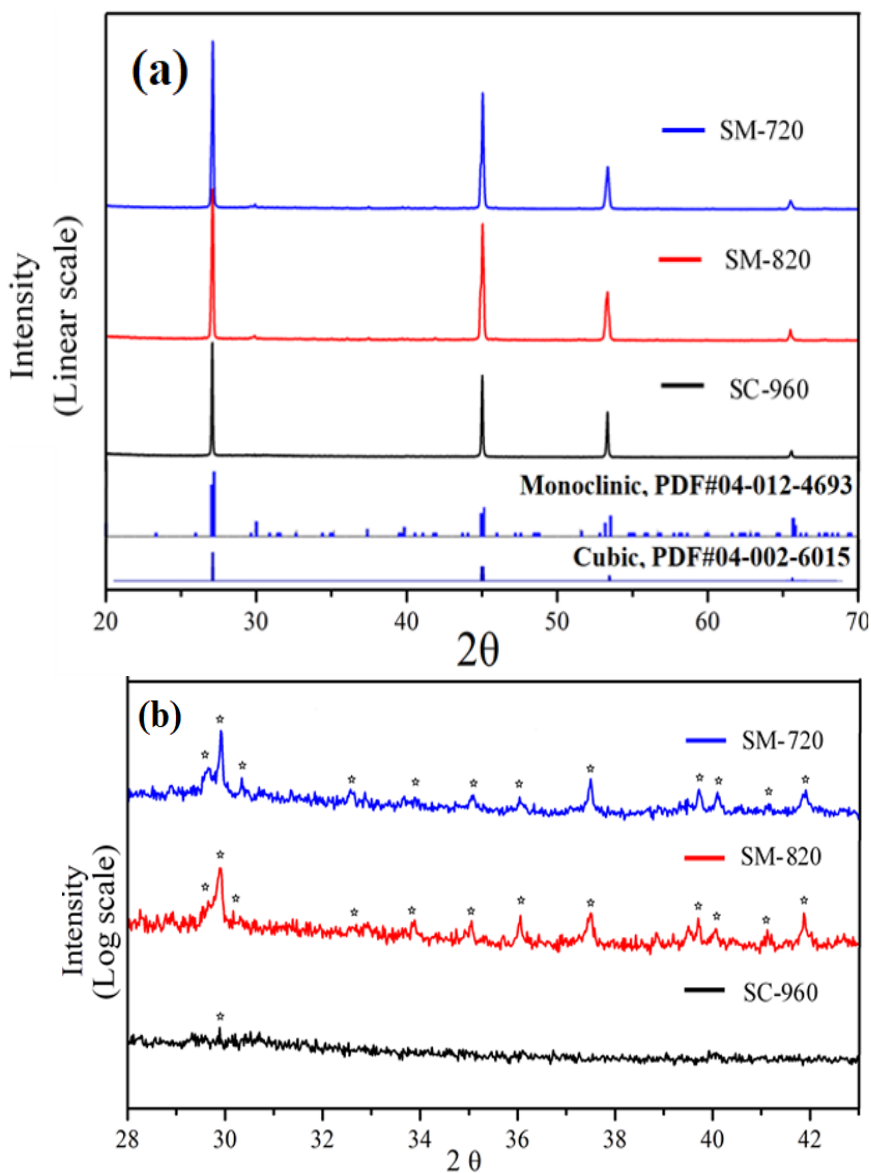


Fig. 1 (a) XRD patterns of CTSe powder samples annealed at 720 K (SM-720), 820 K (SM-820) and 960 K (SC-960). S means the samples were spark-plasma-sintered at 670 K for 5 minutes; M refers to the mostly monoclinic phase while C refers to the mostly cubic phase CTSe. (b) Log scale XRD patterns of the spark-plasma-sintered samples SM-720, SM-820 and SC-960 in the range of 28 to 43 2θ degrees,

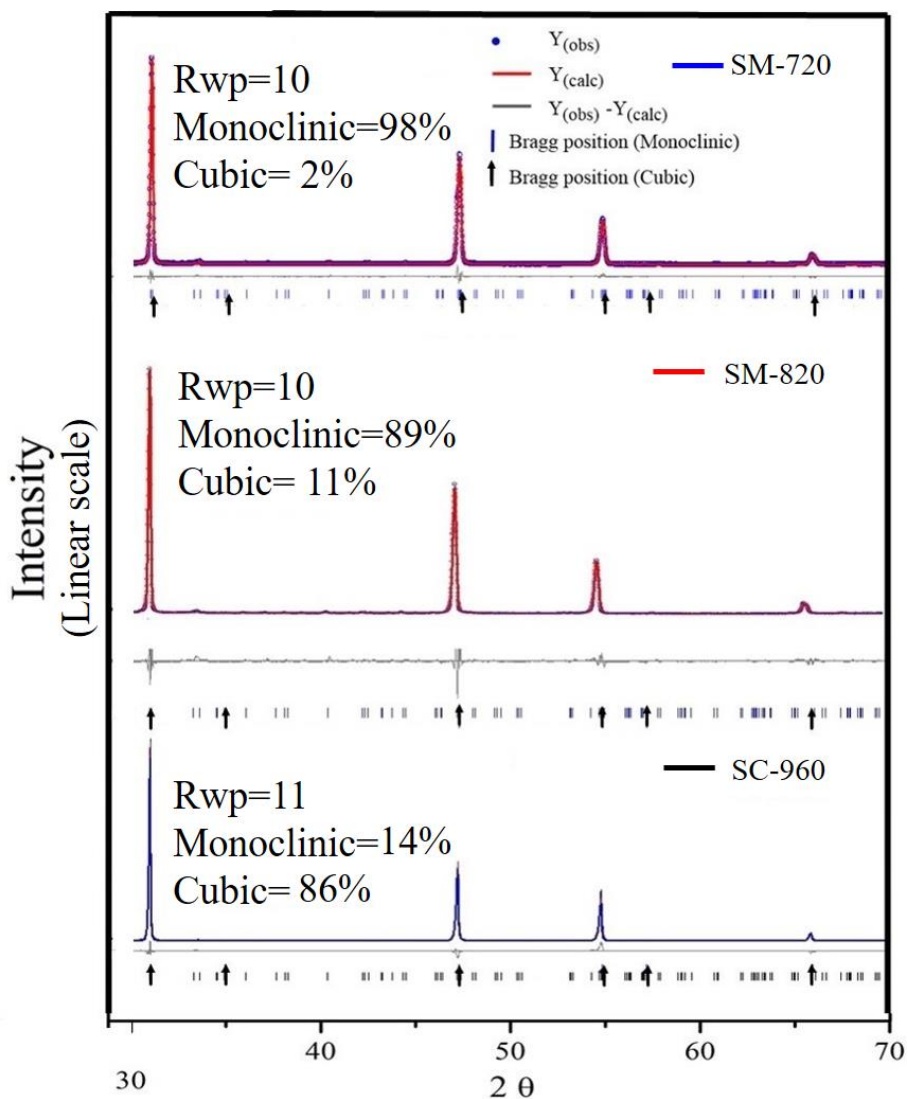


Figure. 2 Results of the Rietveld refinement quantitative phase analyses of SM-720, SM-820 and SC-960 samples are shown along with Rwp values in the upper left corner of each pattern.

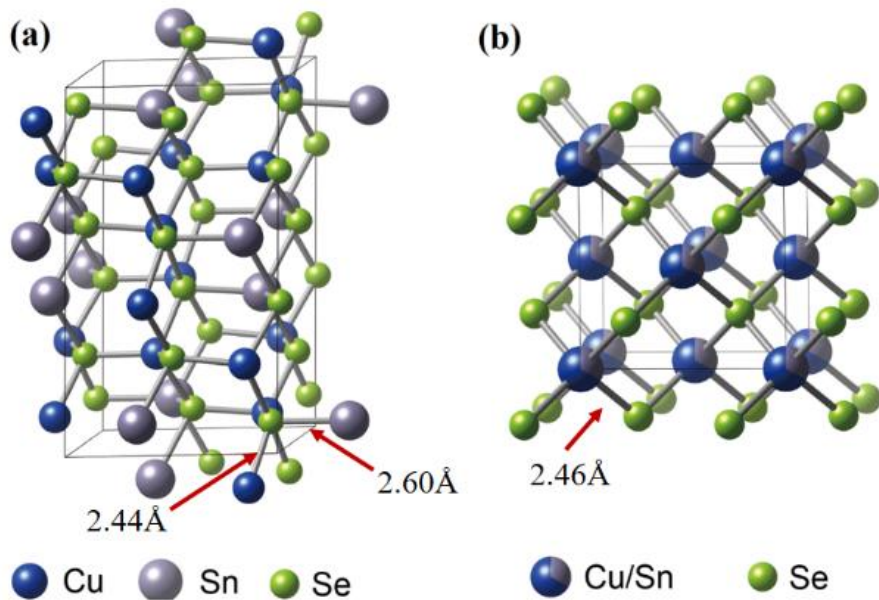


Fig. 3 Structure of (a) monoclinic and (b) cubic CTSe simulated from the Rietveld data files of the two samples [45]. The arrows show the bond lengths between the corresponding atoms. The bond length between Cu and Se is slightly larger for the monoclinic phase than that of the cubic structure. The mixed site occupancy of the Cu and Sn atoms is indicated by partial coloring of the corresponding atoms in (b).

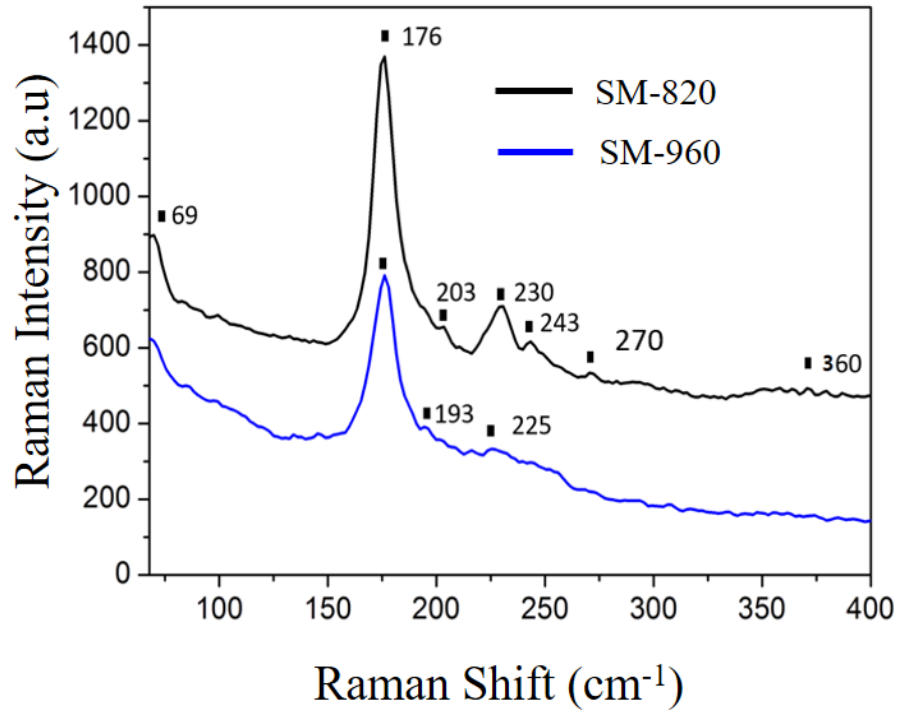


Figure. 4 Raman peaks of SC-960 and SM-820 CTSe powder samples obtained at room temperature, in the range of 40 to 400 cm^{-1} . Raman study was performed on the mostly cubic (SC-960) and mostly monoclinic (SM-820) phases.

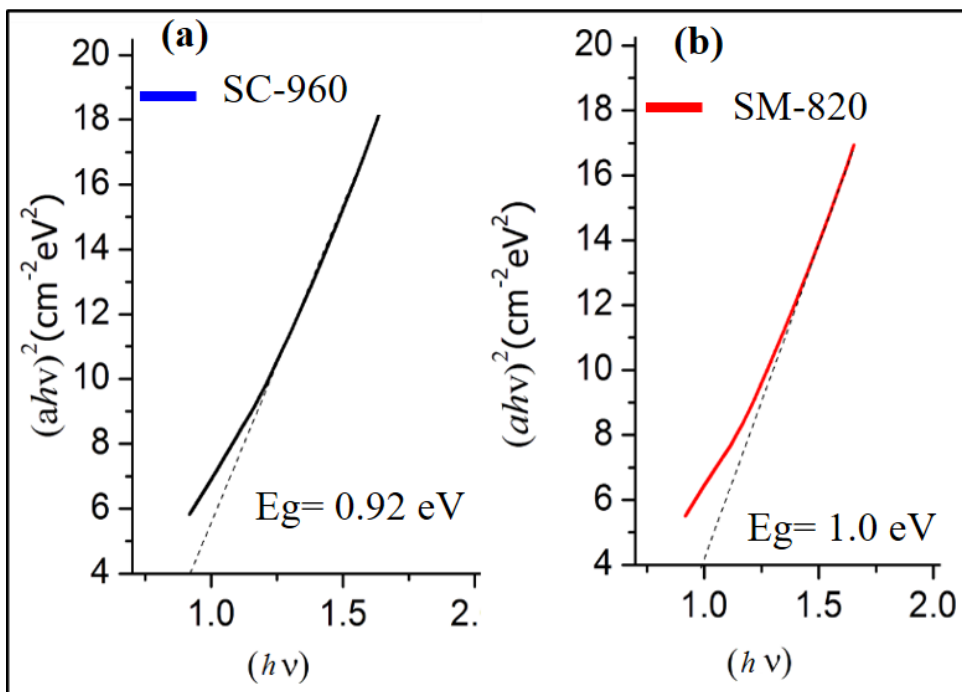


Figure. 5 Shows the UV-Vis spectroscopy measurements for the SM-820 and SC-960 powder samples. The calculated values of $h\nu$ and $(\alpha h\nu)^2$ are plotted for the (a) monoclinic and (b) cubic phases. The band gap value for each phase was obtained by extrapolating these plots to the X-axis.

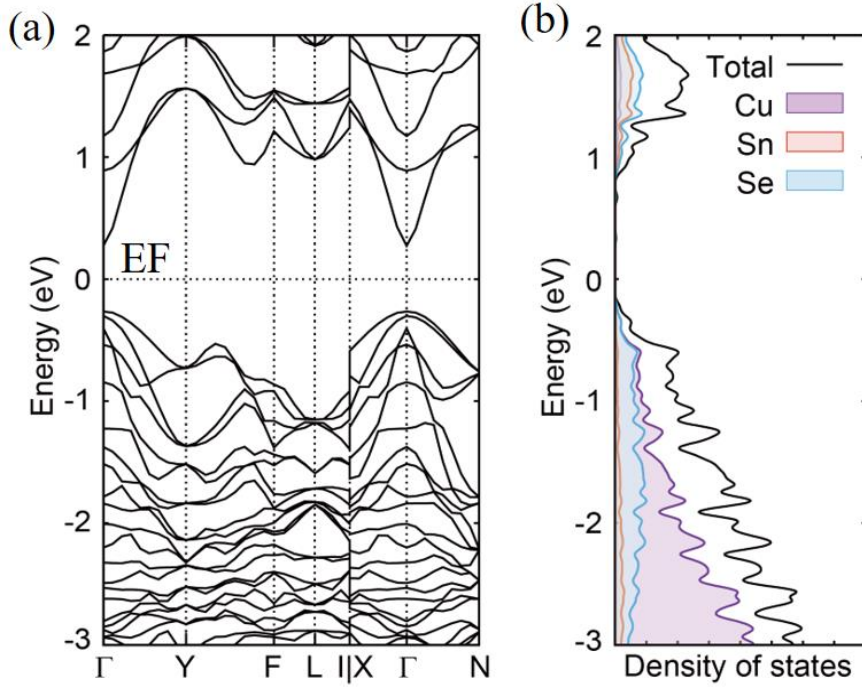


Figure. 6 (a) Band structure and (b) projective density of states of the sample SM-820 obtained by first-principles calculations. EF is the Fermi energy level of the system. The spacing between conduction band minima and valance band maxima at the zero symmetry point Γ is the electronic band gap.

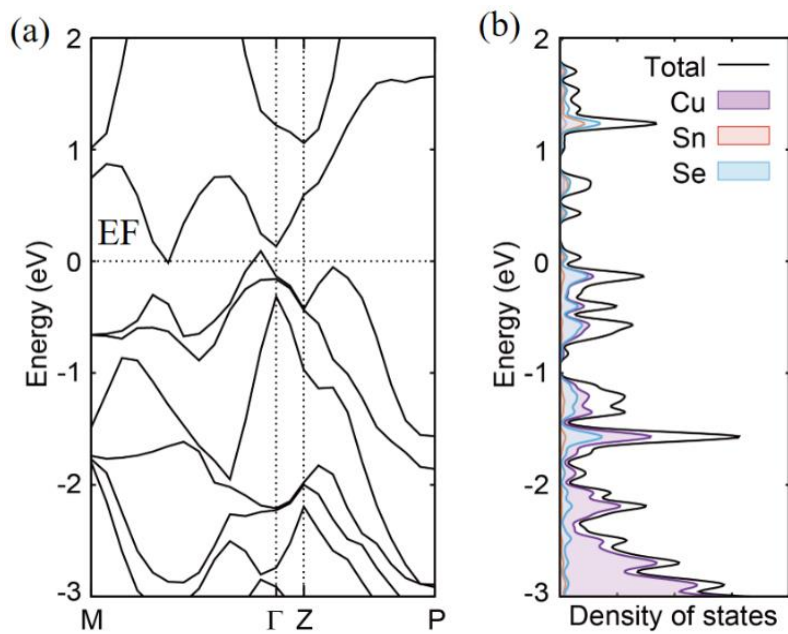


Figure. 7 (a) Band structure and (b) projective density of states of the sample SC-960 obtained by first-principles calculations. EF is the Fermi energy level of the system. There is no band gap at the EF.

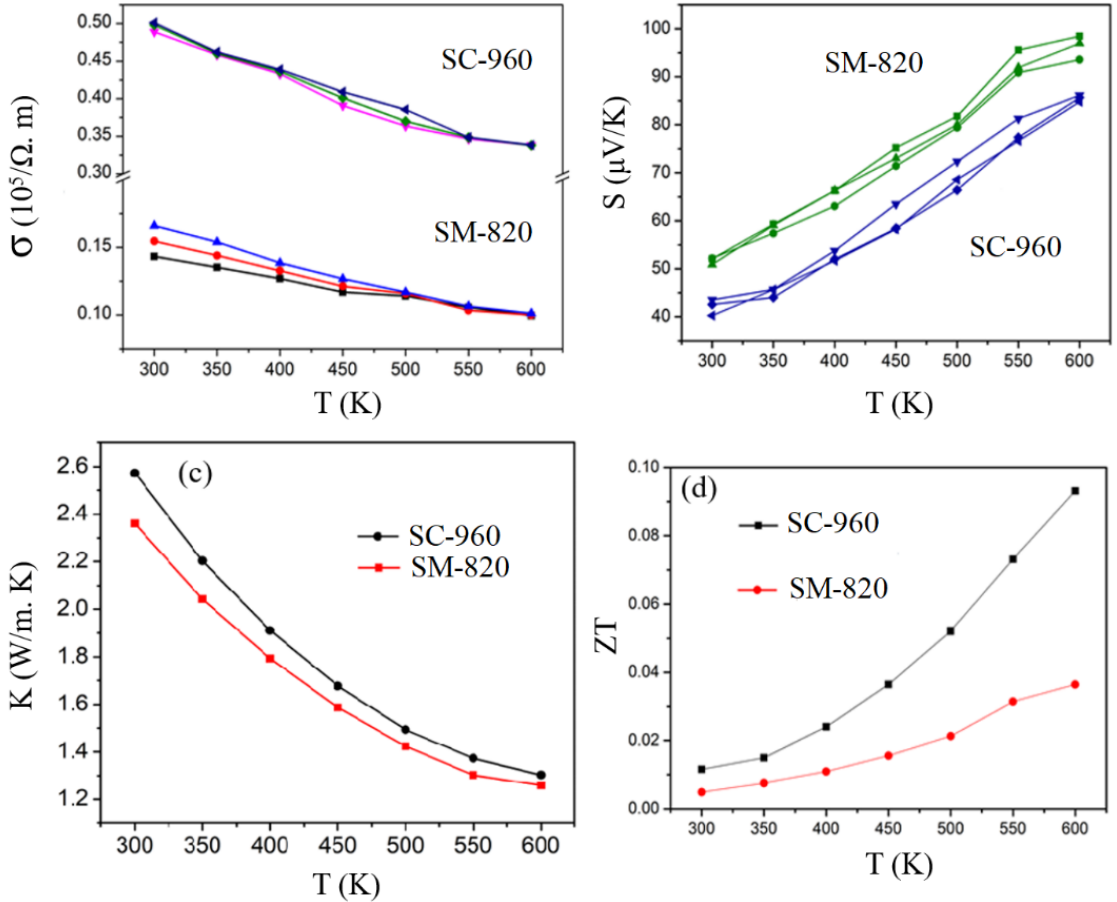


Figure. 8 Temperature dependence of (a) electrical conductivity, (b) Seebeck coefficient, (c) thermal conductivity, and (d) TE Figure of merit ZT for spark-plasma-sintered samples SM-820 and SC-960. Electrical conductivity and Seebeck coefficient measurements were recorded three times to ensure the reproducibility of results.

Table 1 Raman peak positions of the SM-820 and SC-950 taken from Figure 4 and compared with results from reported data.

Raman peaks (cm ⁻¹)								
Peak no	Monoclinic			Cubic			(Calculated) (Monoclinic) Ref. [26]	Symmetry assignments Ref. [26]
	Present Work	Ref. [26]	Ref. [27]	Present work	Ref. [28]	Ref. [29]		
1	69	83	75				82	A'
2	176	178	182	176	177	179	177	A'
3	203	204	196	193	203	199	Not calculated	A''
4	230	231	235	225	230	233	Not calculated	A''
5	243	244	251				250 246	A'
6	270	291					Not calculated	A''
7	360	363	366				356	A'+A' (overtone)

4.4 Summary

The effect of annealing temperature on the phase transition of CTSe was investigated, and the TE properties of the monoclinic and cubic phases of CTSe were compared for the first time. Stoichiometric composition of CTSe was synthesized by melt solidification and heat treatment at various temperatures followed by water quenching. XRD analyses reveal that the samples annealed at 720 and 820 K have mostly monoclinic phase along with small amount of cubic phase. The CTSe annealed at 960 K is mostly cubic. In order to investigate the effect of phase transition on the TE performance of CTSe, TE properties of the samples SPSed at 673 K for 5 min using the powder annealed at 820 (SM820) and 960 (SC960) followed by water quenching were measured in the temperature range of 300 to 600 K. It was found that the mostly cubic phase SC-960 sample has ZT much higher than the mostly monoclinic phase sample. Better TE performance of high temperature cubic phase SC-960 can be attributed to the smaller band gap (~0.92 eV) which can lead to higher electrical conductivity than monoclinic SM-820 (~1.0 eV) at room temperature.

Although the electrical conductivity of the cubic phase is enhanced due to reduction in band gap and high carrier concentration, the increase of thermal conductivity is much smaller than that of the electrical conductivity. One possible reason for the relatively small increase of thermal conductivities of both the monoclinic and cubic phase, is the presence of the minor secondary phase, which can promote the phonon scattering and reduce the thermal conductivity. The results show that the cubic phase CTSe is a better candidate for TE applications than the monoclinic phase, because cubic phase has better TE performance and the performance can be further improved by optimizing Seebeck coefficient by doping at Sn sites or by interstitial alloying.

4.5 References:

- 1) Y. N. Xie, T. M. Chou, W. F. Yang, M. H. He, Y. R. Zhao, N. Li and Z. H. Lin, *Semicond Sci Tech*, 2017, **32**.
- 2) N. Toshima, *Synthetic Met*, 2017, **225**, 3-21.
- 3) Q. Wu and J. L. Hu, *Smart Mater Struct*, 2017, **26**.
- 4) Y. Mao, Y. G. Yan, K. P. Wu, H. Y. Xie, Z. K. Xiu, J. H. Yang, Q. J. Zhang, C. Uher and X. F. Tang, *Rsc Adv*, 2017, **7**, 21439-21445.
- 5) S. N. Girard, J. He, X. Zhou, D. Shoemaker, C. M. Jaworski, C. Uher, V. P. Dravid, J. P. Heremans and M. G. Kanatzidis, *J Am Chem Soc*, 2011, **133**, 16588-16597.
- 6) L. Xi, Y. B. Zhang, X. Y. Shi, J. Yang, X. Shi, L. D. Chen, W. Zhang, J. H. Yang and D. J. Singh, *Phys Rev B*, 2012, **86**.
- 7) X. Y. Shi, L. L. Xi, J. Fan, W. Q. Zhang and L. D. Chen, *Chem Mater*, 2010, **22**, 6029-6031.
- 8) Y. Y. Li, G. H. Liu, J. T. Li, K. X. Chen, G. He, Z. C. Yang, Y. M. Han, M. Zhou and L. F. Li, *Mater Chem Phys*, 2016, **177**, 398-404.
- 9) S. Singh, M. Brandon, P. Liu, F. Laffir, W. Redington and K. M. Ryan, *Chem Mater*, 2016, **28**, 5055-5062.
- 10) Y. Y. Li, G. H. Liu, T. F. Cao, L. M. Liu, J. T. Li, K. X. Chen, L. F. Li, Y. M. Han and M. Zhou, *Adv Funct Mater*, 2016, **26**, 6025-6032.
- 11) J. Fan, H. L. Liu, X. Y. Shi, S. Q. Bai, X. Shi and L. D. Chen, *Acta Mater*, 2013, **61**, 4297-4304.
- 12) J. Fan, W. Schnelle, I. Antonyshyn, I. Veremchuk, W. Carrillo-Cabrera, X. Shi, Y. Grin and L. D. Chen, *Dalton T*, 2014, **43**, 16788-16794.
- 13) L. S. Palatnik, V. M. Koshkin, L. P. Galchinetskii, V. I. Kolesnikov and Y. F. Komnik, *Soviet Physics-Solid State*, 1962, **4**, 1052-1053.
- 14) B. B. Sharma, R. Ayyar and H. Singh, *Phys Status Solidi A*, 1977, **40**, 691-696.
- 15) J. Rivet, *Ann Chim France*, 1965, **10**, 243.
- 16) G. Marcano, C. Rincon, L. M. de Chalbaud, D. B. Bracho and G. S. Perez, *J Appl Phys*, 2001, **90**, 1847-1853.
- 17) J. Fan, W. Carrillo-Cabrera, L. Akselrud, I. Antonyshyn, L. D. Chen and Y. Grin, *Inorg Chem*, 2013, **52**, 11067-11074.
- 18) G. Kresse and J. Furthmuller, *Phys Rev B*, 1996, **54**, 11169-11186.

- 19) J. Heyd, G. E. Scuseria and M. Ernzerhof, *J Chem Phys*, 2006, **124**.
- 20) S. Park, B. Lee, S. H. Jeon and S. Han, *Curr Appl Phys*, 2011, **11**, S337-S340.
- 21) M. E. Norako, M. J. Greaney and R. L. Brutchey, *Journal of the American Chemical Society*, 2012, **134**, 23-26.
- 22) J. J. Wang and K. M. Ryan, *Crystengcomm*, 2016, **18**, 3161-3169.
- 23) L. D. Gulay, M. Daszkiewicz, T. A. Ostapyuk, O. S. Klymovych and O. F. Zmiy, *Acta Crystallogr C*, 2010, **66**, I58-I60.
- 24) Y. T. Zhai, S. Y. Chen, J. H. Yang, H. J. Xiang, X. G. Gong, A. Walsh, J. Kang and S. H. Wei, *Phys Rev B*, 2011, **84**.
- 25) E. Kroumova, M. I. Aroyo, J. M. Perez-Mato, A. Kirov, C. Capillas, S. Ivantchev and H. Wondratschek, *Phase Transit*, 2003, **76**, 155-170.
- 26) G. E. Delgado, A. J. Mora, G. Marcano and C. Rincon, *Mater Res Bull*, 2003, **38**, 1949-1955.
- 27) G. Marcano, C. Rincon, S. A. Lopez, G. S. Perez, J. L. Herrera-Perez, J. G. Mendoza-Alvarez and P. Rodriguez, *Solid State Commun*, 2011, **151**, 84-86.
- 28) J. J. Wang, A. Singh, P. Liu, S. Singh, C. Coughlan, Y. N. Guo and K. M. Ryan, *Journal of the American Chemical Society*, 2013, **135**, 7835-7838.
- 29) P. U. Bhaskar, G. S. Babu, Y. B. K. Kumar and V. S. Raja, *Appl Surf Sci*, 2011, **257**, 8529-8534.
- 30) G. S. Babu, Y. B. K. Kumar, Y. B. K. Reddy and V. S. Raja, *Mater Chem Phys*, 2006, **96**, 442-446.
- 31) D. H. Kuo, W. D. Haung, Y. S. Huang, J. D. Wu and Y. J. Lin, *Surf Coat Tech*, 2010, **205**, S196-S200.
- 32) H. H. Huang, X. F. Fan, D. J. Singh, H. Chen, Q. Jiang and W. T. Zheng, *Phys Chem Chem Phys*, 2016, **18**, 4086-4094.
- 33) F. A. La Porta, L. Gracia, J. Andres, J. R. Sambrano, J. A. Varela and E. Longo, *J Am Ceram Soc*, 2014, **97**, 4011-4018.
- 34) E. Burstein, *Phys Rev*, 1954, **93**, 632-633.
- 35) J. Jimenez and J. W. Tomm, *Journal*, 2016, DOI: 10.1007/978-3-319-42349-4, 1 online resource (xi, 307 pages).
- 36) Y. W. Shen, C. Li, R. Huang, R. M. Tian, Y. Ye, L. Pan, K. Koumoto, R. Z. Zhang, C. L. Wan and Y. F. Wang, *Sci Rep-Uk*, 2016, **6**.
- 37) P. J. Sun, B. P. Wei, J. H. Zhang, J. M. Tomczak, A. M. Strydom, M. Sondergaard, B. B. Iversen and F. Steglich, *Nat Commun*, 2015, **6**.

- 38) G. H. Liu, K. X. Chen, J. T. Li, Y. Y. Li, M. Zhou and L. F. Li, *J Eur Ceram Soc*, 2016, **36**, 1407-1415.
- 39) D. M. Rowe, *TEs handbook: macro to nano*, CRC/Taylor & Francis, Boca Raton, 2006.
- 40) K. Momma and F. Izumi, *J Appl Crystallogr*, 2011, **44**, 1272-1276.
- 41) S. Johnsen, J. Q. He, J. Androulakis, V. P. Dravid, I. Todorov, D. Y. Chung and M. G. Kanatzidis, *Journal of the American Chemical Society*, 2011, **133**, 3460-3470.
- 42) A. F. May, J. P. Fleurial and G. J. Snyder, *Phys Rev B*, 2008, **78**.
- 43) J. W. Richardson, D. L. Price and M. L. Saboungi, *Phys Rev Lett*, 1996, **76**, 1852-1855.
- 44) P. S. Whitfield, N. Herron, W. E. Guise, K. Page, Y. Q. Cheng, I. Milas and M. K. Crawford, *Sci Rep-Uk*, 2016, **6**.
- 45) R. M. Murphy, E. D. Murray, S. Fahy and I. Savic, *Phys Rev B*, 2016, **93**.

5 Chapter 5

The effect of SnS addition to Cu_2SnSe_3 on the thermoelectric properties of Cu_2SnSe_3 -SnS composites

5.1 Introduction

TE materials are the subject of great interest for the scientists and engineers, as it can directly convert waste heat into electricity [1, 2]. The TE efficiency of materials is generally governed by the dimensionless Figure of merit $ZT = \sigma S^2 T / \kappa$, where σ is electrical conductivity, S is Seebeck coefficient, T is absolute temperature and κ is the thermal conductivity. The total thermal conductivity can be further divided into lattice thermal conductivity (κ_l) and carrier thermal conductivity (κ_e). A good TE material should have a large σ and S with low κ [3]. To develop TE materials with high TE performance is the ultimate goal of TE research. The improvements of ZT of chalcogenides and silicides were reported using various approaches which include nano-structuring, doping and alloying [4-6]. Alloying of compounds results in disorder and lattice distortion, which enhances the phonon scattering and decreases the thermal conductivity. Optimized composition in composites can also increase the effective mass of the system, which can lead to the enhancement of Seebeck coefficient [7]. Composites, which consist of more than two phases, can lead to the formation of inclusions and interfaces, which can block the low energy phonon without affecting the electronic carrier transport significantly; hence, the low thermal

conductivity is expected along with reasonable electrical conductivity [8]. This approach is an efficient way to improve TE efficiency by optimizing the electrical and thermal transport properties. Composites can also lead to point defect scattering, which can reduce the lattice thermal conductivity, and hence higher ZT can be achieved for the composite system than pristine compound [9].

Besides TE performance (ZT), the cost and environmental considerations are equally important for TE materials for their commercial large scale applications. The existing efficient TE materials contain expensive or toxic elements such as Te, Pb etc. [10, 11]. And so, CTSe is a promising TE material with earth abundant, cheap and environment-friendly elements, such as Sn and Se, which emerged in the past decade as a potential alternative for those which are used in TE devices today [12, 13].

TE properties of the CTSe (CTSe) are very close to those of other commercialized TE materials like PbTe, except the Seebeck coefficient which is much lower than that of PbTe. This leads to ZT much lower than the TE materials which are used in TE devices today and which are known to be promising candidates for large scale application. It can be expected that the increase in Seebeck coefficient along with reasonable thermal and electrical properties can lead to control of TE properties of CTSe. In this study, we report the TE properties of CTSe-SnS composites fabricated by mechanical alloying and spark plasma sintering. We successfully controlled the Seebeck coefficient by adding SnS to the CTSe matrix. Improvement of TE properties (enhanced ZT) in the medium temperature range (300 K ~ 570 K) is achieved by adding 3 wt% SnS to the CTSe matrix.

5.2 Materials and Methods

CTSe-SnS composite powder samples (0.5, 1, 3 and 5 wt% SnS) which were named according to the amount of SnS added to CTSe, were synthesized by two-step process. CTSe and SnS were prepared separately from the stoichiometric amount of precursor elements, Cu 99.99 %, Sn 99.99 % Se 99.99 % and S 99.99 % powders (Kunjundo Chemicals, Japan of average size 5μ) by mechanical alloying for 5 hours. And then these two compounds were mixed and mechanical-alloyed for 1 hour to obtain homogeneous composite powder samples.

Powder samples were consolidated using spark plasma sintering. An appropriate amount of powder was put into a graphite die and pressed up to 600 kgf pressure. Sintering was performed at 670 K for 10 minutes. The thicknesses of the consolidated samples were around 10 mm with lateral diameter of about 12 mm. The bar samples with longitudinal direction parallel to the direction of the pressure applied during spark plasma sintering with typical dimension of $2 \times 2 \times 6 \text{ mm}^3$ were used to measure the out-of-plane Seebeck coefficient and electrical resistivity. Phase studies were performed on the powder and pellet samples using powder X-ray diffraction (XRD) (Bruker, D-8 Advance) with copper $K\alpha$ radiation. Microstructural and energy dispersive spectroscopy (EDS) analyses were carried out using FE-SEM (Merlin, Compact). The TE properties were measured in the temperature range of 300 to 570 K, using commercial TE property measurement system (SEPEL, TEP-800). Laser flash technique (LFA, Netzsch, 457) was used to measure the thermal diffusivity (D) of the carbon coated disc-shape samples with thickness $< 1 \text{ mm}$, in the temperature range of

300 to 570 K in an inert atmosphere. Thermal conductivity (κ) was obtained using the equation $\kappa = D\rho C_p$, where D is the thermal diffusivity, ρ is the bulk density measured by the Archimedes method and C_p is the specific heat capacity obtained by the Dulong–Petit approximation. Hall Effect measurements of carrier concentration (p_H) and mobility (μ_H) on square-shape samples were performed in a van der Pauw configuration by Ecopia (HMS-3000) system at room temperature.

5.3 Results and discussion

Figure 1 shows the XRD patterns of CTSe, SnS and CTSe-SnS composites, recorded in the range of 2θ from 20 to 70 degree. CTSe and composite samples have the monoclinic phase structure. The patterns of 3 and 5 wt% CTSe-SnS composites have peaks with very small intensities between 30 and 45 degrees 2θ , most of which come from the SnS phase. Figure 2 shows FE-SEM images of fracture surfaces of the CTSe, SnS and CTSe-SnS composite samples. Red arrows indicate the SnS phase. The images show that the grain size is decreased with the increase of the amount of SnS in the CTSe matrix. To further investigate the effect of SnS addition to CTSe on the crystallite size, we analyzed the average crystallite size and micro strain by Williamson & Hall (W-H) method [14].

The uniform distribution model (UDM) was applied in W-H method, where it is assumed that the strain is same for all crystallographic directions in the crystal

[15]. The modeled equation for the UDM in W-H method consists of both size and strain factors, represented by [15]

$$\beta_{hkl} \cos\theta = \frac{K\lambda}{D} + 4\varepsilon \sin\theta$$

Where β_{hkl} represents the full width at half maximum (FWHM) of a radiant peak. K is crystallite shape constant (0.9), λ is the wavelength of X-ray in nanometer (nm) and ε is the strain. By plotting $4 \sin\theta$ on x-axis with $\beta_{hkl} \cos\theta$ on y-axis, the strain of the crystallites was estimated from the slope of the line, while the average size was calculated from the y-axis intercept. The W-H plots for the studied samples are given in Figure 3, while the extracted data is provided in Table 1. We also estimated the average size of the crystallites for studied samples using the Scherer's formula (Table 1). The sizes of the crystallites obtained from the Scherer's formula and the W-H method which are known to be semi-quantitative methods need to be considered carefully. The absolute numbers (size of crystallites) obtained from those two methods can be different from the numbers (size of grains) which can be obtained from the direct observation (e.g. SEM). And also the instrument contribution to the breadth of the XRD peaks was not considered in Scherer's formula and W-H method because the contribution was identical in all the patterns which were collected using the same instrument with the same setting. But the trend of changes can still be compared with those obtained from the direct SEM observation.

As shown in Table 1, the average variation of the crystallite size is consistent with the SEM data (Figure 2), where the size of grains is decreased with the

increase of the amount of SnS in the composite samples. The crystallite size values obtained by Scherer's formula and W-H method are similar, and the trends in both cases are consistent. The decrease in the grain size in 3 wt% and 5 wt% can come from the particles of SnS, which can retard the grain growth. The density of the sintered sample is increased with the increase of the SnS amount as shown in Figure 4, which shows the density of the sintered CTSe, SnS and CTSe-SnS composites. EDS elemental mapping results which are given in Figure 5 show that the distribution of the element S is uniform and the composite samples have homogeneous composition in the scale shown in the figure.

Figure 6 shows temperature dependence of (a) Seebeck coefficient, (b) electrical conductivity of spark plasma sintered CTSe, SnS and composites. The Hall-Effect data measured at room temperature are given in Figure 6(c-d) and also in Table 2. Positive Seebeck coefficient is recorded for all the samples in the temperature range from 300 to 570 K (Figure 6(a)), which confirms the *p*-type nature of CTSe, SnS and CTSe-SnS composites. The Seebeck coefficient value of the pristine CTSe is in the range of 30 to 59 $\mu\text{V/K}$, which is increased up to 500 $\mu\text{V/K}$ by making composites with SnS. The large increase in Seebeck coefficient of the CTSe-SnS can come from the high Seebeck coefficient of SnS and the increase of carrier mobility. Adding SnS to the CTSe matrix results in the decrease of carrier concentration (Figure 6(c)) while carrier mobility is increased (Figure 6(d)). This can result from the misalignment of energy bands between host and foreign materials. With the misalignment of energy bands, a large potential barrier can block both majority and minority carriers and only very high-energy carriers can

pass through this potential barrier with small probability of scattering. The overall effect leads to low carrier concentration yet with high mobility within the composite samples.

The band misalignment permits the minority carriers to excite in the direction opposite to the majority carriers (*p*-type or *n*-type) so that large voltage is retained while Seebeck coefficient is increased [16, 17]. Figure 6(a) shows that the Seebeck coefficient of CTSe is not only enhanced but its behavior with increasing temperature is also changed by adding even small amount (3 wt%) of SnS to the CTSe matrix due to the large decrease in carrier concentration. The behavior of Seebeck coefficient with increasing temperature of 0.5 and 1 wt% resembles that of the CTSe sample while samples with more than 1 wt% SnS show bipolar behaviors of Seebeck coefficient which is similar to that of SnS [18].

Figure 6(b) shows the temperature dependence of the electrical conductivity from 300k ~ 570K. A decrease of electrical conductivity with increasing temperature of 0.5 and 0 wt% composite samples reveals the highly doped nature of all the samples. The reduction in the electrical conductivity of the composite samples compared to that of CTSe is in agreement with the carrier concentration data, shown in Figure 6(c). As the amount of SnS in the CTSe matrix is increased, the carrier concentration is reduced and electrical conductivity is suppressed. Figure 7(a) shows the change of thermal conductivity of the CTSe and CTSe-SnS composites at different temperatures. The lattice distortion and defects in the CTSe after incorporation of SnS can reduce the thermal conductivity of the parent matrix, due to the extra disorder

scattering (Figure 7(b)). In contrast, a large improvement of ZT was observed (Figure 8(b)) due to the reduction of thermal conductivity.

It should be noticed that further addition of SnS to the CTSe matrix in the sample with 5 wt%, leads to the decrease in both power factor and ZT due to the poor electronic transport nature of the sample.

According to Abeles et. al. [19], the composite matrix is assumed to have a random distribution of its species in a proper lattice. The resulted scattering of the phonon is larger due to displaced position and anharmonicity of the crystal lattice. One common way to find the degree of disorder scattering of the composites is calculating the scattering parameter (Γ). Large Γ means large phonon scattering, which can decrease the thermal conductivity.

Γ consists of strain induced by point defects, bonding force difference and mass difference for the binary or pseudo-binary alloy systems [20].

$$\Gamma = x.y \left[\left(\frac{\Delta M}{M} \right)^2 + \varepsilon \left(\frac{\Delta \alpha}{a} \right)^2 \right] \quad (1)$$

M and α are the mean mass and lattice constants of the binary components in the alloy, while ΔM and $\Delta \alpha$ are the differences in molar mass and lattice constants within the virtual crystal respectively. ε in eq.1 is a fitting parameter, which describes the elastic properties of a lattice system [21]. Numerical value of ε can be estimated as:

$$\varepsilon = \frac{2}{9} \left[(G + 6.4\gamma) \frac{1+\nu}{1-\nu} \right]^2 \quad (2)$$

G is a relative constant, which remain the same for the similar compound systems [22, 23], γ is the Gruneisen parameter and ν is the Poisson ratio. We used $\gamma=1.3$ and $G=4$ for the chalcogenides alloy [24, 25] to fit the ϵ value which is equal to 94. The values of γ , G and ϵ used in this study are in good agreement with those previously reported [26, 27]. The results obtained from eq.1 are plotted for the four composite samples at room temperature in Figure 7(b). It shows that increasing the amount of foreign atoms in the parent matrix results in the increase of the scattering parameter. The change of scattering parameter is consistent with the change of thermal conductivity in Figure 7(a) and results reported before [28, 29].

Figure 8 shows the effect of adding different amounts of SnS to CTSe on the power factor and the ZT of the CTSe and composite samples, measured in the temperature range from room temperature to 570K. Large improvements of Seebeck coefficient were observed in the composites

(Figure 6(a)), but the change of power factor was not significant Figure 8(a)) which can result from the synergetic effect of the reduction in electrical conductivity (Figure 6(b)). In contrast, a large improvement of ZT was observed (Figure 8(b)) due to the reduction of thermal conductivity. The sample with 3 wt% SnS has peak ZT equal to 0.18, which is comparable with those previously reported [30-32]. It should be noticed that further addition of SnS to the CTSe matrix in the sample with 5 wt%, leads to the decrease in both power factor and ZT due to the poor electronic transport nature of the sample.

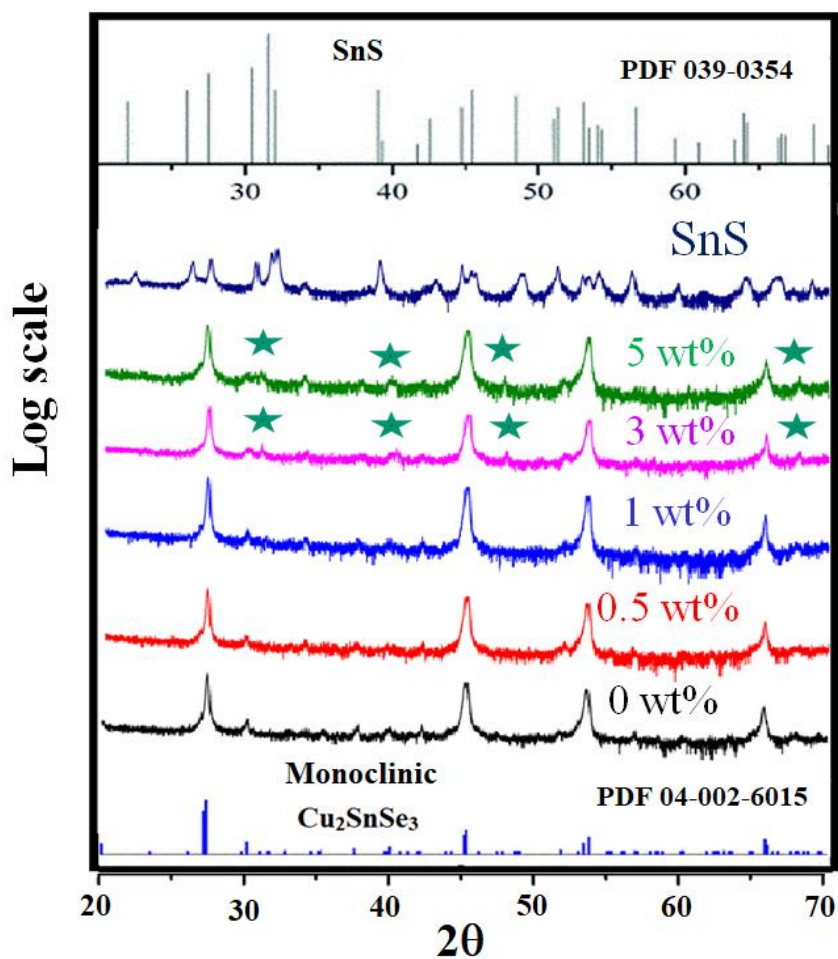


Figure 1. XRD patterns of CTSe-SnS composite samples spark plasma sintered at 670 K. The bottom and top spectra represent the XRD patterns of CTSe and SnS respectively, while the other spectra show those of composite samples. Minor peaks indicated by stars in the patterns of 3 and 5 wt% samples correspond to the SnS phase.

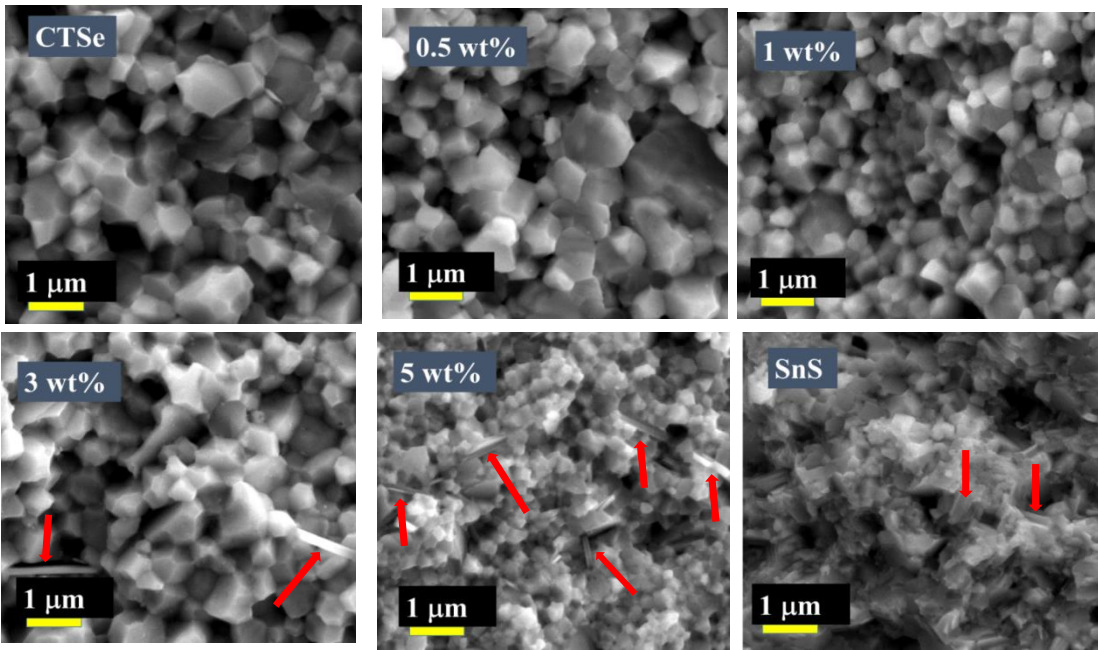


Figure 2. FE-SEM images of the CTSe, SnS and CTSe-SnS composite samples. The FE-SEM analyses were performed on the non-polished surfaces of the broken pellets. Red arrows indicate the SnS secondary phase within the CTSe matrix.

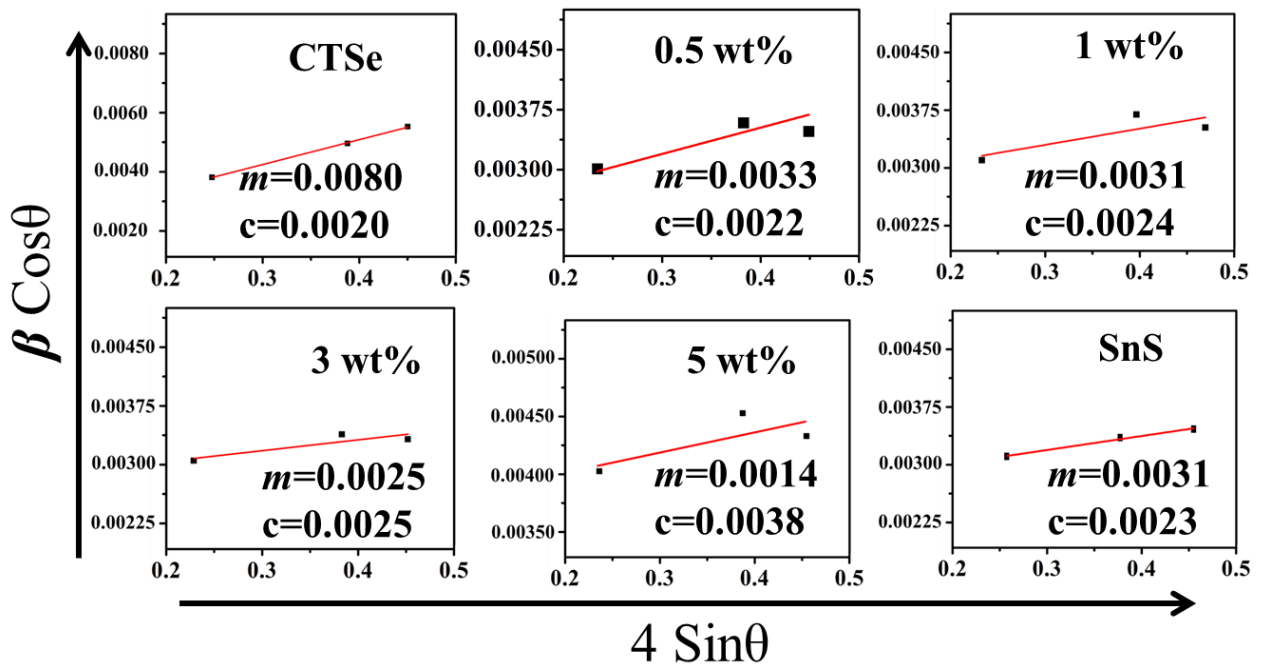


Figure 3. Results of Williamson & Hall (W-H) method. Plot of $\beta_{hkl} \cos\theta$ vs $4 \sin\theta$ of the spark plasma sintered CTSe, SnS and CTSe-SnS composites.

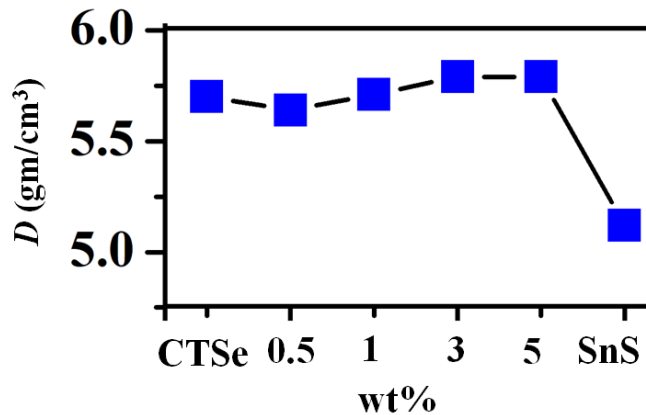


Figure 4. Density of the spark plasma sintered CTSe, SnS and CTSe-SnS composites. Each point represents the average of five different readings.

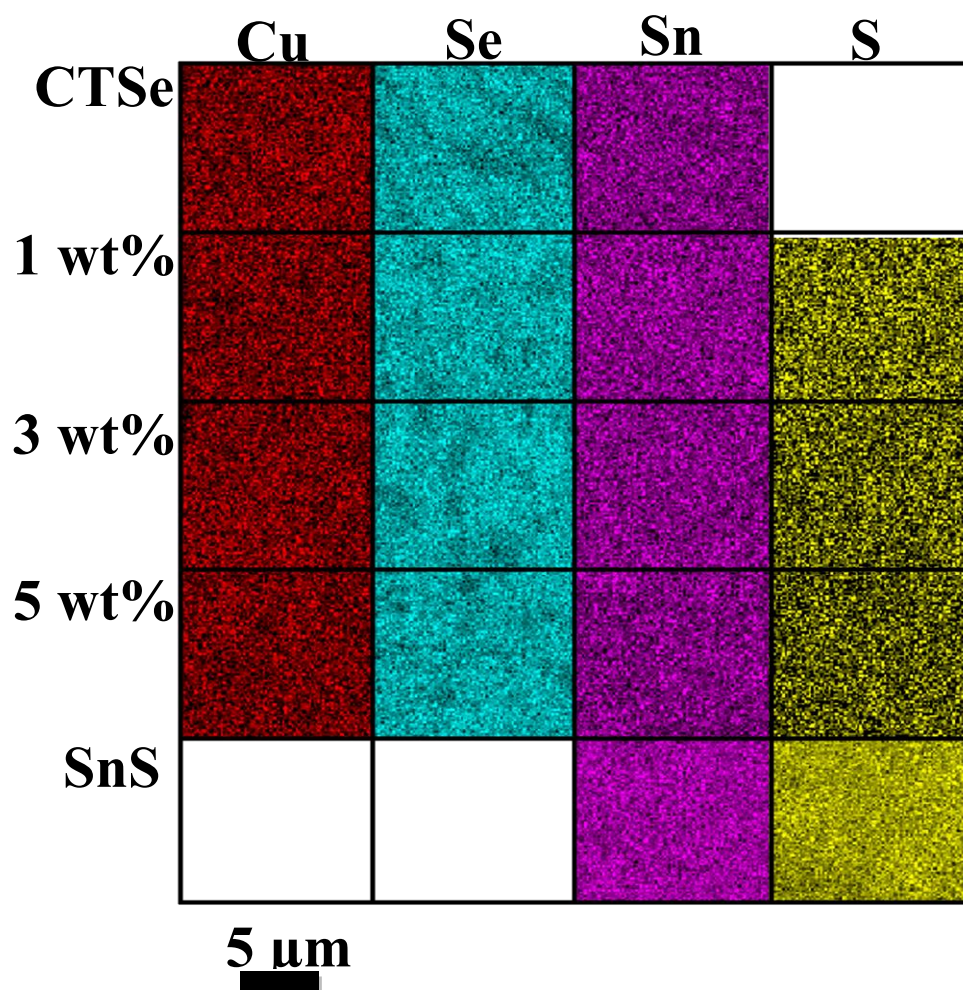


Figure 5. EDS mapping images of the CTSe, SnS and composites. The analyses were performed on the polished surfaces of the pellets.

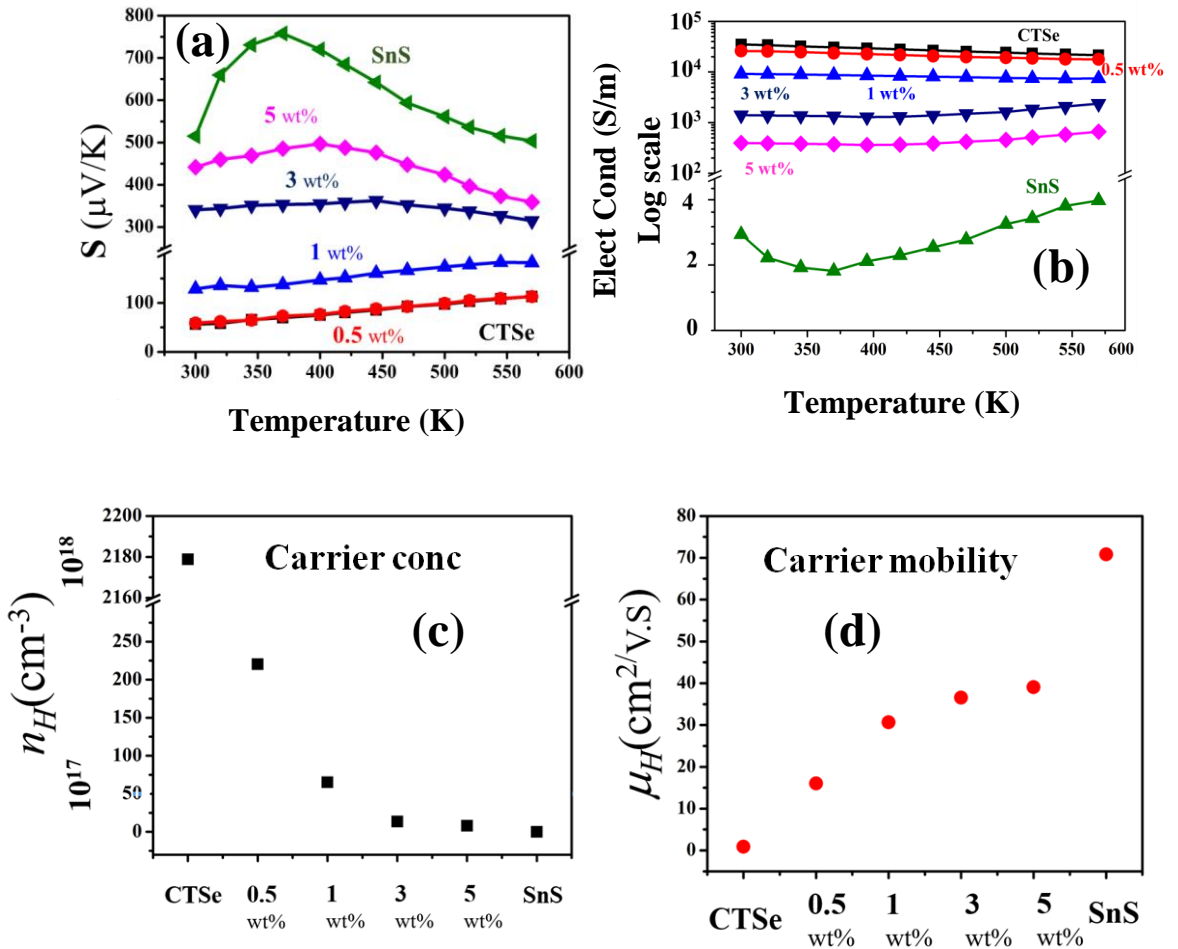


Figure 6. Temperature dependence of (a) Seebeck coefficient, (b) electrical conductivity, (c) carrier concentration and (d) electronic mobility values of the CTSe, SnS and CTSe-SnS composites. Each data point of (c) and (d) is the average of ten readings recorded on each sample.

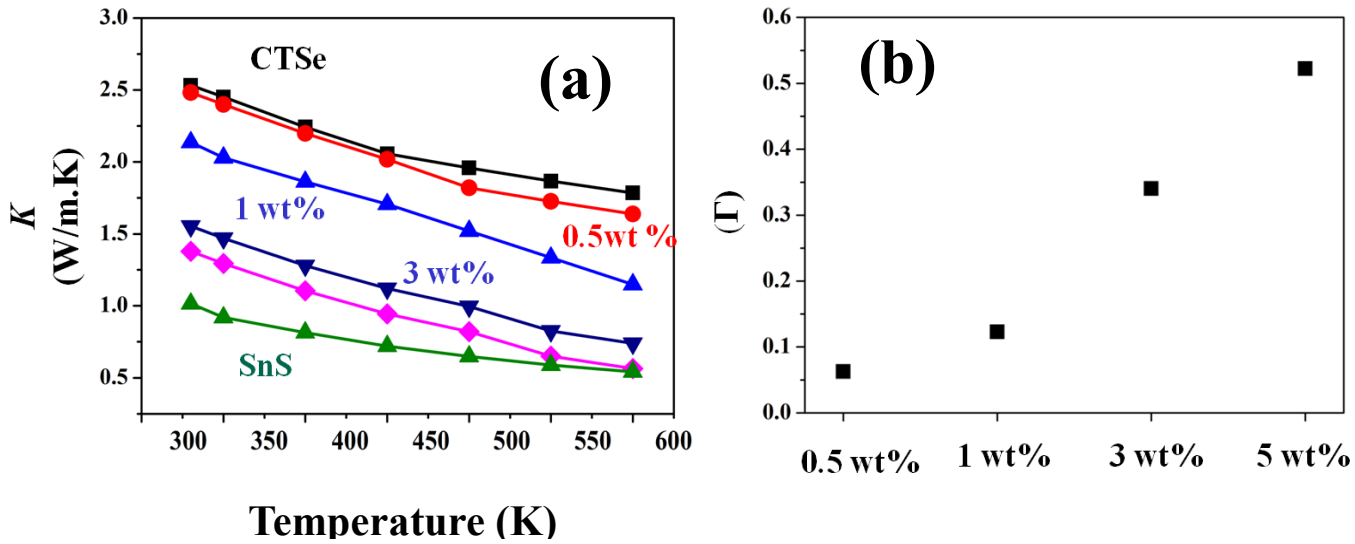


Figure 7. (a) Temperature dependence of thermal conductivity of CTSe, SnS and CTSe-SnS composites and (b) lattice scattering parameter values of the CTSe-SnS composite samples.

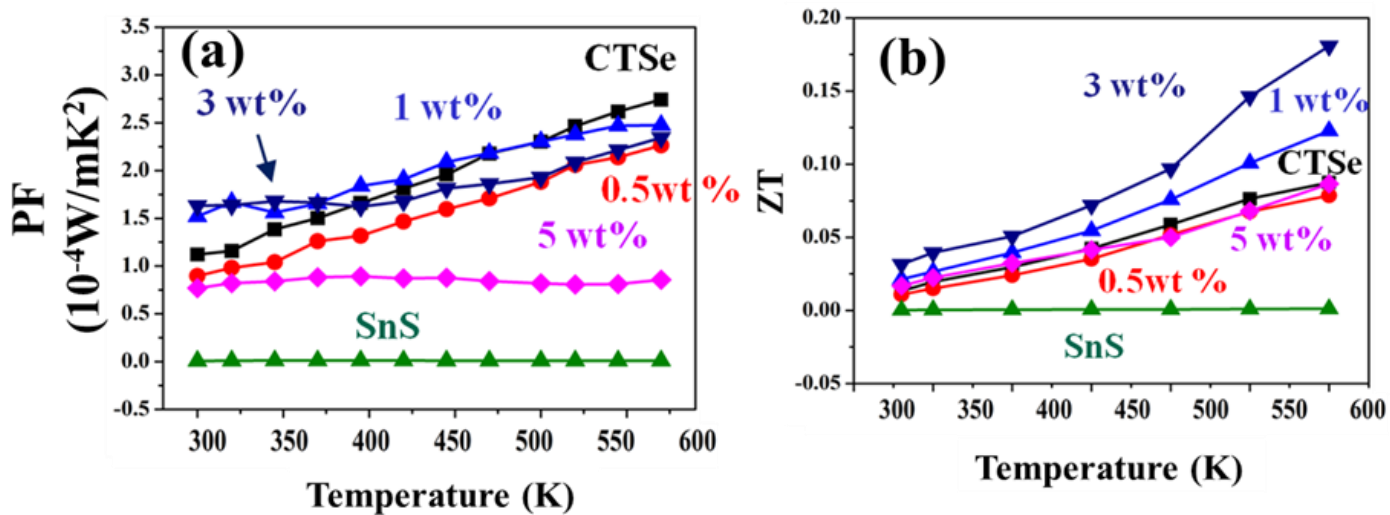


Figure 8. (a) Power factor and (b) ZT of CTSe, SnS and CTSe-SnS composites in the temperature range from 300 to 570 K.

Table 1. Geometric parameters of the spark plasma sintered CTSe, SnS and CTSe-SnS composites.

Sample	Scherer's method	W-H method	
		<i>D</i> (nm)	ϵ (10^{-3})
CTSe	49.21	67.97	8.03
0.5 wt%	41.39	62.74	3.29
1 wt%	40.47	58.50	3.07
3 wt%	38.42	55.91	2.47
5 wt%	32.14	36.30	1.41
SnS	34.62	60.02	3.46

Table 2. Hall-Effect data of the spark plasma sintered CTSe, SnS and CTSe-SnS composites.

Sample	Carrier Conc	Carrier Mobility
	$n_H (/cm^{-3}) (10^{17})$	$\mu_H (cm^2/V.S)$
CTSe	21788.21	0.89
0.5 wt%	220.35	16.03
1 wt%	65.15	30.67
3 wt%	13.58	36.56
5 wt%	0.80	39.05
SnS	0.02	73.23

5.4 Summary

The CTSe (CTSe)-SnS composites were prepared by mechanical alloying and spark plasma sintering. The effect of adding different amount of SnS to CTSe on the TE properties of the composite was investigated. The addition of SnS to CTSe was found to improve the Seebeck coefficient, but the change of power factor was not substantial due to the loss of electrical conductivity. Improvement of ZT in the medium temperature range, however, is achieved by adding 3 wt% SnS to the CTSe matrix, which can be attributed to the disorder scattering, which can decrease the thermal conductivity of the composites compared to that of the pristine CTSe. The results of this study shows that the Seebeck coefficient and the thermal conductivity of CTSe can be controlled in the direction of increasing ZT by making a composite with materials which have Seebeck coefficient higher than that of CTSe and which has no reaction with CTSe at the temperature range used to sinter CTSe. However, the concurrent suppression of electrical conductivity, still needs to be controlled to further improve the TE performance of CTSe.

5.5 References

- 1) Bell, L. E. "Cooling, Heating, Generating Power, and Recovering Waste Heat with TE Systems." *Science* 321, no. 5895 (Sep 12 2008): 1457-61. <http://dx.doi.org/10.1126/science.1158899>.
- 2) Minnich, A. J., M. S. Dresselhaus, Z. F. Ren, and G. Chen. "Bulk Nanostructured TE Materials: Current Research and Future Prospects."

- Energy & Environmental Science 2, no. 5 (2009): 466-79. <http://dx.doi.org/10.1039/b822664b>.
- 3) Park, D., H. Ju, T. Oh, and J. Kim. "Facile Fabrication of One-Dimensional Te/Cu₂Te Nanorod Composites with Improved TE Power Factor and Low Thermal Conductivity." *Sci Rep* 8, no. 1 (Dec 24 2018): 18082. <http://dx.doi.org/10.1038/s41598-018-35713-9>.
 - 4) Biswas, K., J. Q. He, I. D. Blum, Chun-Iwu, T. P. Hogan, D. N. Seidman, V. P. Dravid, and M. G. Kanatzidis. "High-Performance Bulk TEs with All-Scale Hierarchical Architectures (Vol 489, Pg 414, 2012)." *Nature* 490, no. 7421 (Oct 25 2012). <http://dx.doi.org/10.1038/nature11645>.
 - 5) Mehta, R. J., Y. L. Zhang, C. Karthik, B. Singh, R. W. Siegel, T. Borca-Tasciuc, and G. Ramanath. "A New Class of Doped Nanobulk High-Figure-of-Merit TEs by Scalable Bottom-up Assembly." *Nature Materials* 11, no. 3 (Mar 2012): 233-40. <http://dx.doi.org/10.1038/Nmat3213>.
 - 6) Zhao, L. L., F. Y. Fei, J. Wang, F. N. Wang, C. L. Wang, J. C. Li, J. Y. Wang, Z. X. Cheng, S. X. Dou, and X. L. Wang. "Improvement of TE Properties and Their Correlations with Electron Effective Mass in Cu_{1.98}S_{1-x}Se_{1-x}." *Scientific Reports* 7 (Jan 16 2017). <http://dx.doi.org/ARTN 40436>
 - 7) [10.1038/srep40436](http://dx.doi.org/10.1038/srep40436).
 - 8) Chauhan, N. S., A. Bhardwaj, T. D. Senguttuvan, R. P. Pant, R. C. Mallik, and D. K. Misra. "A Synergistic Combination of Atomic Scale Structural Engineering and Panoramic Approach in P-Type ZrCoSb-Based Half-Heusler TE Materials for Achieving High Zt." *Journal of Materials Chemistry C* 4, no. 24 (2016): 5766-78. <http://dx.doi.org/10.1039/c6tc01115b>.
 - 9) Zhang, C. H., H. Ng, Z. Li, K. A. Khor, and Q. H. Xiong. "Minority Carrier Blocking to Enhance the TE Performance of Solution-Processed Bi₂Sb₂X₃ Nanocomposites Via a Liquid-Phase Sintering Process." *Acs Applied Materials & Interfaces* 9, no. 14 (Apr 12 2017): 12501-10. <http://dx.doi.org/10.1021/acsami.7b01473>.
 - 10) Song, D. X., W. G. Ma, and X. Zhang. "Lattice Thermal Conductivity of Si/Ge Composite TE Material: Effect of Si Particle Distribution." *International Journal of Energy Research* 43, no. 1 (Jan 2019): 379-90. <http://dx.doi.org/10.1002/er.4272>.

- 11) Pei, Y. Z., A. D. LaLonde, N. A. Heinz, and G. J. Snyder. "High TE Figure of Merit in Pbte Alloys Demonstrated in Pbte-Cdte." *Advanced Energy Materials* 2, no. 6 (Jun 2012): 670-75. <http://dx.doi.org/10.1002/aenm.201100770>.
- 12) Pei, Y. Z., Z. M. Gibbs, A. Gloskovskii, B. Balke, W. G. Zeier, and G. J. Snyder. "Optimum Carrier Concentration in N-Type Pbte TEs." *Advanced Energy Materials* 4, no. 13 (Sep 16 2014). <http://dx.doi.org/ARTN 1400486>
- 13) 10.1002/aenm.201400486.
- 14) Byeon, D., R. Sobota, K. Delime-Codrin, S. Choi, K. Hirata, M. Adachi, M. Kiyama, T. Matsuura, Y. Yamamoto, M. Matsunami, and T. Takeuchi. "Discovery of Colossal Seebeck Effect in Metallic Cu₂se." *Nature Communications* 10 (Jan 8 2019). <http://dx.doi.org/ARTN 72>
- 15) 10.1038/s41467-018-07877-5.
- 16) Liu, Y., L. D. Zhao, Y. C. Liu, J. L. Lan, W. Xu, F. Li, B. P. Zhang, D. Berardan, N. Dragoe, Y. H. Lin, C. W. Nan, J. F. Li, and H. M. Zhu. "Remarkable Enhancement in TE Performance of Bicusseo by Cu Deficiencies (Vol 133, Pg 20112, 2011)." *Journal of the American Chemical Society* 134, no. 6 (Feb 15 2012): 3312-12. <http://dx.doi.org/10.1021/ja211769z>.
- 17) G.K Williamson and W.H Hall. "X-ray line broadening from filed aluminium and wolfram". *Acta Metallurgica*, 1, no 1, (January 1953): 22-31
- 18) Aly, K. A., N. M. Khalil, Y. Algamal, and Q. M. A. Saleem. "Estimation of Lattice Strain for Zirconia Nano-Particles Based on Williamson-Hall Analysis." *Materials Chemistry and Physics* 193 (Jun 1 2017): 182-88. <http://dx.doi.org/10.1016/j.matchemphys.2017.01.059>.
- 19) Banik, A., B. Vishal, S. Perumal, R. Datta, and K. Biswas. "The Origin of Low Thermal Conductivity in Sn₁-Xsbxte: Phonon Scattering Via Layered Intergrowth Nanostructures." *Energy & Environmental Science* 9, no. 6 (2016): 2011-19. <http://dx.doi.org/10.1039/c6ee00728g>.
- 20) Hobbs, C. C., L. R. C. Fonseca, A. Knizhnik, V. Dhandapani, S. B. Samavedam, W. J. Taylor, J. M. Grant, L. G. Dip, D. H. Triyoso, R. I. Hegde, D. C. Gilmer, R. Garcia, D. Roan, M. L. Lovejoy, R. S. Rai, E. A. Hebert, H. H. Tseng, S. G. H. Anderson, B. E. White, and P. J. Tobin. "Fermi-Level Pinning at the Polysilicon/Metal Oxide Interface - Part I."

- Ieee Transactions on Electron Devices 51, no. 6 (Jun 2004): 971-77.
<http://dx.doi.org/10.1109/Ted.2004.829513>.
- 21) Wang, C., Y. D. Chen, J. Jiang, R. Zhang, Y. Niu, T. Zhou, J. F. Xia, H. Q. Tian, J. Hu, and P. Yang. "Improved TE Properties of Sns Synthesized by Chemical Precipitation." *Rsc Advances* 7, no. 27 (2017): 16795-800.
<http://dx.doi.org/10.1039/c7ra00373k>.
 - 22) Abeles, B. "Lattice Thermal Conductivity of Disordered Semiconductor Alloys at High Temperatures." *Phys. Rev.* 131 (1963): 1906.
 - 23) G. T. Alekseeva , B. A. Efi mova , L. M. Ostrovskaya , O. S. Serebryannikova , M. I. Tsypin *Sov. Phys. Semicond.-USSR* 4 (1971): 1122.
 - 24) Wang, H., A. D. LaLonde, Y. Z. Pei, and G. J. Snyder. "The Criteria for Beneficial Disorder in TE Solid Solutions." *Advanced Functional Materials* 23, no. 12 (Mar 25 2013): 1586-96.
<http://dx.doi.org/10.1002/adfm.201201576>.
 - 25) Wang, H., J. L. Wang, X. L. Cao, and G. J. Snyder. "TE Alloys between Pbse and Pbs with Effective Thermal Conductivity Reduction and High Figure of Merit." *Journal of Materials Chemistry A* 2, no. 9 (2014): 3169-74. <http://dx.doi.org/10.1039/c3ta14929c>.
 - 26) Jin, H. Y., C. M. Jaworski, and J. P. Heremans. "Enhancement in the Figure of Merit of P-Type Bi100-Xsbx Alloys through Multiple Valence-Band Doping." *Applied Physics Letters* 101, no. 5 (Jul 30 2012).
<http://dx.doi.org/Artn 053904>
 - 27) [10.1063/1.4740262](http://dx.doi.org/10.1063/1.4740262).
 - 28) Nafe, Orson L. Anderson John E. "The Bulk Modulus-Volume Relationship for Oxide Compounds and Related Geophysical Problems." *Journal of Geophysical Research* 70, no. 16 (1965): 3951-63.
 - 29) Anderson, D. L. Anderson and O. L. "The Bulk Modulus Volume Relationship for Oxides." *J. Geophys. Res* 75 (1970): 3494-500.
 - 30) Baeyer, Joseph Callaway and Hans C. von. "Effect of Point Imperfections on Lattice Thermal Conductivity." *Phys. Rev.* 120 (1960): 1149.
 - 31) Klemens, P. G. "Thermal Resistance Due to Point Defects at High Temperatures
 32) " *Phys. Rev.* 119 (1960): 507.
 - 33) Qiu, P. F., X. Y. Huang, X. H. Chen, and L. D. Chen. "Enhanced TE Performance by the Combination of Alloying and Doping in Ticosb-

- Based Half-Heusler Compounds." *Journal of Applied Physics* 106, no. 10 (Nov 15 2009). <http://dx.doi.org/Artn 103703>
- 34) 10.1063/1.3238363.
- 35) Pei, Y. Z., H. Wang, and G. J. Snyder. "Band Engineering of TE Materials." *Advanced Materials* 24, no. 46 (Dec 4 2012): 6125-35. <http://dx.doi.org/10.1002/adma.201202919>.
- 36) Fan, J., W. Schnelle, I. Antonyshyn, I. Veremchuk, W. Carrillo-Cabrera, X. Shi, Y. Grin, and L. D. Chen. "Structural Evolvment and TE Properties of Cu₃Xsnxse₃ Compounds with Diamond-Like Crystal Structures." *Dalton Transactions* 43, no. 44 (2014): 16788-94. <http://dx.doi.org/10.1039/c4dt01457j>.
- 37) Li, Y. Y., G. H. Liu, T. F. Cao, L. M. Liu, J. T. Li, K. X. Chen, L. F. Li, Y. M. Han, and M. Zhou. "Enhanced TE Properties of CTSe by (Ag,in)-Co-Doping." *Advanced Functional Materials* 26, no. 33 (Sep 6 2016): 6025-32. <http://dx.doi.org/10.1002/adfm.201601486>.
- 38) Shi, X. Y., L. L. Xi, J. Fan, W. Q. Zhang, and L. D. Chen. "Cu-Se Bond Network and TE Compounds with Complex Diamondlike Structure." *Chemistry of Materials* 22, no. 22 (Nov 23 2010): 6029-31. <http://dx.doi.org/10.1021/cm101589c>.

6 Chapter 6

Seebeck coefficient optimization for the improved ZT in $\text{Cu}_2\text{Sn}(\text{S}_x, \text{Se}_{1-x})_3$ ($0 \leq x \leq 0.8$) solid solution

6.1 Introduction

The performance of a TE materials is evaluated on the basis of the dimensionless figure of merit, $ZT = S^2\sigma T/\kappa$, where σ is the electrical conductivity, S is the Seebeck

coefficient, κ is the total thermal conductivity and T is the absolute temperature in Kelvin [1, 2]. Increase in ZT requires high values of S and σ but still low thermal conductivity. It is very hard to control these TE parameters independently, where all of them are connected to each other by one way or another.

It is found that semiconductors can be a better choice due to high Seebeck coefficient and dominant heat conduction by phonon migration [3]. These days most of the commercialized TE materials are mostly semiconductors compounds or alloys. Bismuth telluride (Bi_2Te_3) and its alloys are good TE materials below room temperature. Above room temperature the relatively narrow band gap causes mixed conduction due to both electrons and holes [4]. This leads to reduced Seebeck coefficient. Bismuth telluride can be alloyed with Sb_2Te_3 or Bi_2Se_3 , which reduces thermal conductivity considerably. To date the TE technology is not commercially mature due to its low efficiency. Apart from the

low efficiency other challenges includes the high cost and toxicity of the elements used in the TE modules. TE materials such as Bi_2Te_3 , Sb_2Te_3 and PbTe consist of either toxic or expensive elements [5, 6]. Therefore, exploration of TE materials with less toxic, less expensive and more earth-abundant elements is the focus of the TE community these days. The ternary chalcogenides CTSe is expected to be one of these auspicious TE materials, owning large flexibility to tune its physical and electronic properties [7]. The elements of CTSe are less toxic, abundant in nature and relatively cheap compared to Te and Pb.

In our previous study (Chapter # 5), we found that composites is an efficient way for enhancing Seebeck coefficient of CTSe, where optimum doping in composites can increase the effective mass of the system which can lead to enhance its Seebeck coefficient. An optimized improvement in TE properties was achieved by adding 5% SnS to the CTSe matrix, which led to enhanced ZT in the medium temperature range. It was found that SnS addition to CTSe can effectively enhance the Seebeck coefficient from 30 to 490 $\mu\text{V}/\text{K}$ at room temperature, but the power factor was not much improved due to the loss of electrical conductivity. But still, a prominent improvement in ZT value from 0.06 to 0.15 at 570 K for the CTSe was achieved due to disorder scattering, which can lead to a lower thermal conductivity of the composites than the pristine CTSe. Despite of large improvement enhancement in Seebeck coefficient in the CTSe –SnS composites, the improvement in the ZT value was not that impressive due to loss of electrical conductivity.

It is a big challenge to decouple Seebeck coefficient and electrical properties in alloying and composites, where increasing one value will lead to compromise another [8]. Here we introduced a strategy to control the Seebeck coefficient without losing large part of electrical conductivity of the CTSe by making its solid solution with Cu_2SnS_3 . Suppressing Se vacancies by introducing S in the Cu_2SnS_3 lattice is one of the way to control the Seebeck coefficient. The analogous crystal and band structure of CTSe with Cu_2SnS_3 was the motivation behind the study of TE performance of $\text{Cu}_2\text{Sn}(\text{S}_x, \text{Se}_{1-x})_3$ ($0 \leq X \leq 0.8$) solid solution. Cu_2SnS_3 and $\text{Cu}_2\text{Sn}(\text{S}_x, \text{Se}_{1-x})_3$ ($0 \leq X \leq 0.8$) solid solution were prepared using mechanical alloying (MA) followed by spark plasma sintering. Rietveld refinement of the powder X-ray diffraction (XRD) data was performed to determine the variation in the lattice constants of the $\text{Cu}_2\text{Sn}(\text{S}_x, \text{Se}_{1-x})_3$ ($0 \leq X \leq 0.8$) solid solution with gradual replacing of Se with S. Here we found that the band gap and TE properties optimization as well as reducing in thermal conductivity can be efficiently achieved by careful optimizing of the composition of $\text{Cu}_2\text{Sn}(\text{S}_x, \text{Se}_{1-x})_3$ ($0 \leq X \leq 0.8$) solid solution for enhanced TE performance of the CTSe.

6.2 Experimental procedure

6.2.1 Sample preparation:

Cu_2SnS_3 and $\text{Cu}_2\text{Sn}(\text{S}_x, \text{Se}_{1-x})_3$ ($0 \leq X \leq 0.8$) solid solution were prepared using mechanical alloying (MA) followed by spark plasma sintering. Stoichiometric amount of Cu 99.99 %, Sn 99.99 %, Se 99.99 % and S 99.99 % powders (Kunjundo Chemicals, Japan) were sealed in the stainless steel container under the Argon atmosphere and run for the three hours continuously to ensure the

solid state reaction. Powder samples were sintered using spark plasma sintering (SPS). An appropriate amount of powder was put into a graphite die and pressed up to 600 kgf pressure, sintering was performed at 670 K for 10 minutes.

6.2.2 Characterization:

Phase studies were performed on the pellet samples, using powder X-ray diffraction (XRD) D-8 Advance (Bruker, Germany), with copper $K\alpha$ radiation of $\lambda = 1.54 \text{ \AA}$. Rietveld refinement (TOPAS) was used for the quantitative phase analyses of the samples. Raman scattering analyses were performed on the pellet samples using LabRAM Raman spectrometer (HORIBA Scientific). The He-Ne laser source with wavelength of 532 nm was used as the exciting light. The LabRAM spectrometer is equipped with both macroanalysis and microanalysis configurations. The laser beam of mm order spot size was focused on the sample surface using an optical input focusing macroanalysis system. The incident laser beam was further focused to 1 μm spot size using optical microscope ($\times 50$ objectives) in microanalysis system. All the measurements were performed in the range of 50 to 400 (cm^{-1}) Raman shifts at ambient temperature.

The Seebeck coefficient and the electrical resistivity were measured in the temperature range of 300 to 575 K, using commercial TE property measurement system, (SEPEL, TEP-800). The measurements were carried out in Ar atmosphere to prevent the oxidation of the SPSed samples.

Laser flash technique (LFA, Netzsch, LFA 457) was used to measure the thermal diffusivity (D) of carbon coated disc-shape samples with thickness $< 1 \text{ mm}$, in the temperature range of 300 to 575 K in the inert atmosphere. Differential scanning

calorimetry (DSC) was used to measure the specific heat (C_p) in the same temperature range as D . The samples were put in an alumina crucible in Ar atmosphere, and the DSC curve was recorded with a heating rate of 10 K/min. Thermal conductivity (k) was calculated from $k = C_p \cdot d \cdot D$, where C_p , d and D are specific heat obtained from DSC, density and thermal diffusivity, respectively. The densities of the pellet samples were measured using Archimedes' principle at room temperature in ethanol medium.

Ultraviolet-visible (UV-Vis) spectroscopy analyses were performed on the polycrystalline powder samples, dispersed in ethanol, using UV-Vis/NIR Spectrometer (JASCO, V-770). The optical absorption spectra were obtained in the wavelength range of 600 to 1000 nm, with a step size of 0.5 nm.

6.3 Results and Discussions

Figure 1 shows the XRD patterns of Cu_2SnS_3 and $\text{Cu}_2\text{Sn}(\text{S}_x, \text{Se}_{1-x})_3$ ($0 \leq x \leq 0.8$) solid solution, recorded in the range of 2θ from 20 to 70 degree. Cu_2SnS_3 its solid solutions have the monoclinic phase structure. Minor peaks (28-45 2θ) representing monoclinic structure, are more visible after sintering. XRD analysis reveal that as we increase the amount of Sulfur in the solid solution, peak positions shift towards right, which indicate the increasing amount of Cu_2SnS_3 . Shifting of peak from CTSe towards Cu_2SnS_3 along with the absence of secondary phases confirm the successful formation of the solid solution.

The XRD results were further confirmed through EDS and Raman spectroscopy. EDS elemental mapping data is given in Figure 2, where it can be seen that no segregation is resulted and all the samples shows homogeneous distribution of

all the present elements. Similarly in Raman spectroscopy results in Figure 3 it is shown that as the amount of Sulfur is increased the spectra transform from pure CTSe to the Cu_2SnS_3 and the sample $X=0.8$ has similar spectra as that of the CTSe. Results from EDS and Raman analysis confirm the successful formation of the solid solution of the CTSe and Cu_2SnS_3 structures. Raman spectra related to secondary phases was not observed as shown in Figure 3, which reveals the absence of secondary phases.

TE studies for CTSe and its solid solutions with Cu_2SnS_3 were performed on the dense pellet samples and the results are shown in Figure 4. It is notable that at first when we increased the amount of Sulfur ($X=0.2$) the Seebeck coefficient is increased while further increase of Sulfur in the solid solution resulted in decrease in the Seebeck coefficient as seen for the sample $X=0.45$. After further increase of the amount of Sulfur, the Seebeck coefficient again started to increase and the trend continue until the last sample, $X=0.8$. Similar behaviour was experienced in the electrical conductivity data as shown in Figure 4.b, where electrical conductivity first increase then decrease with increasing of the amount of Sulfur in the solid solution. To understand this anomalous behaviour of the TE properties of the studied compositions, we performed the microstructural analysis on these samples. The SEM micrographs are shown in the Figure5, where we found that no prominent effect on microstructure was observed in the solid solution samples. Here it can be seen that the grain size of the studied solid solution samples are not that much different. One other important factor which can influence the TE properties is the band gap tuning due to variation in

composition in the solid solution. The Tauc plots which represent the band gap spectra of the solid solution samples are given in the figure 6. These estimated band gap values are in well agreement with that of the TE properties as the electrical conductivity for any composition is decreased the band gap value is higher for it. This agreement between electrical properties and band gap values reveals that variation in the composition resulted in the band gap tuning and hence the TE properties are varied accordingly.

Thermal conductivity and ZT values are given in the Figure 7. It is very interesting to see that the thermal conductivity values are gradually decreased with increasing amount of the Sulfur as shown in Figure 7.a. It confirms that solid solution of these two structures (CTSe and CTS) can be way to control the thermal and electrical properties independently and hence larger ZT can be achieved. This independent control of thermal and electrical properties in the solid solution of the CTSe-S structure leads to achieve reasonable ZT of equal to 0.8 for the $X=0.8$ solid solution sample as shown in Figure 7 b.

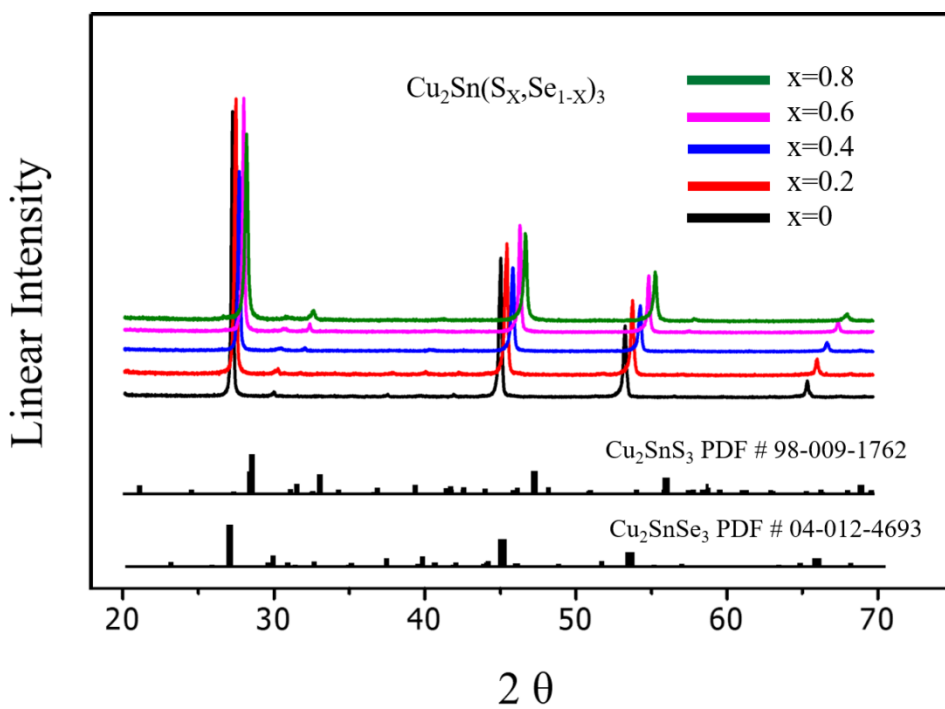


Figure 1. XRD patterns of Cu_2SnS_3 and $\text{Cu}_2\text{Sn}(\text{S}_x, \text{Se}_{1-x})_3$ ($0 \leq x \leq 0.8$) solid solution samples spark plasma sintered at 670 K.

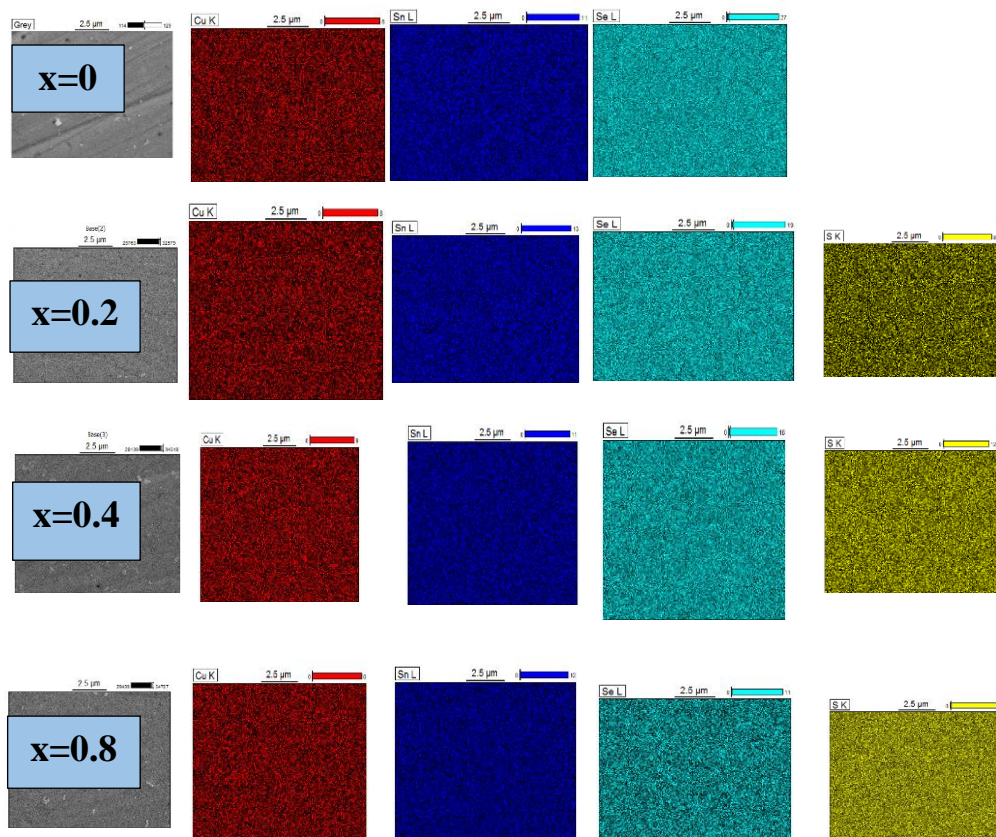


Figure 2. EDS mapping images of the CTSe and Cu₂Sn (S_x, Se_{1-x})₃ (0 ≤ X ≤ 0.8) solid solution samples. The analyses were performed on the polished surfaces of the pellets.

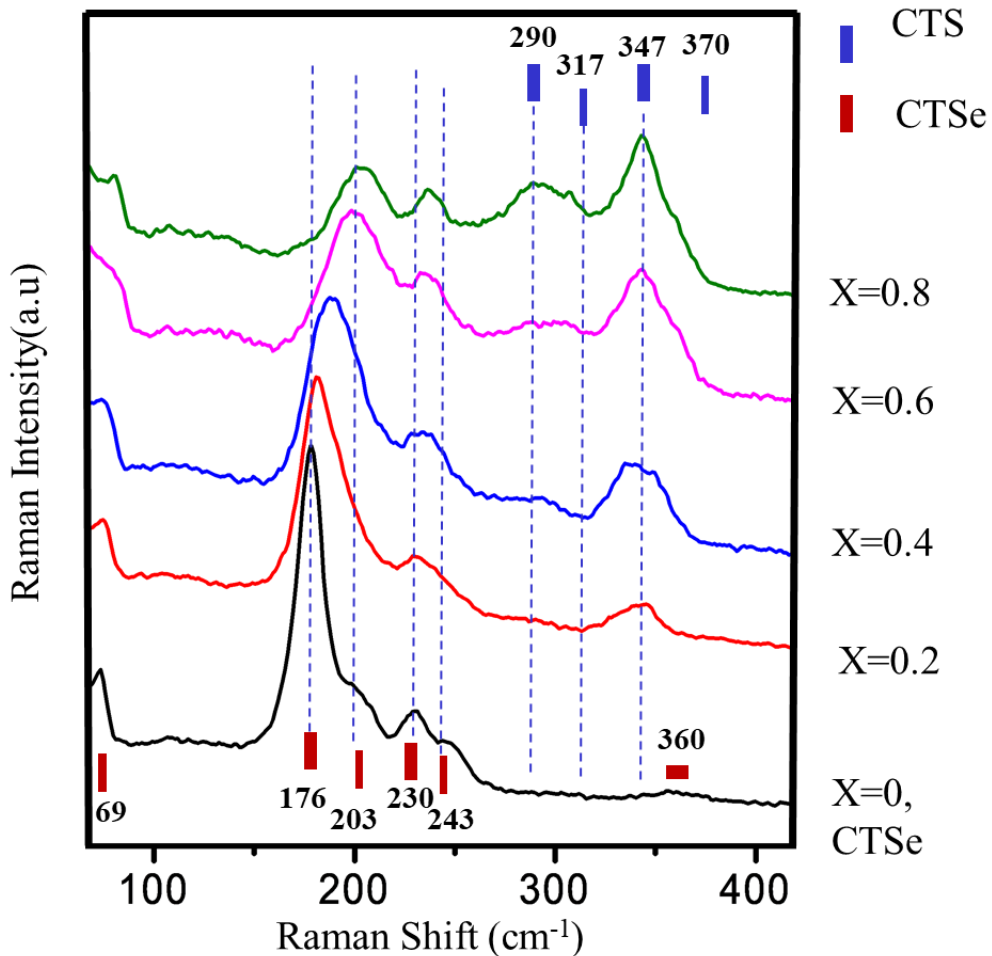


Figure 3. Raman spectra of the CTSe and Cu₂Sn (S_x, Se_{1-x})₃ (0 ≤ X ≤ 0.8) solid solution samples. The Raman spectroscopic analyses were performed on the powder samples.

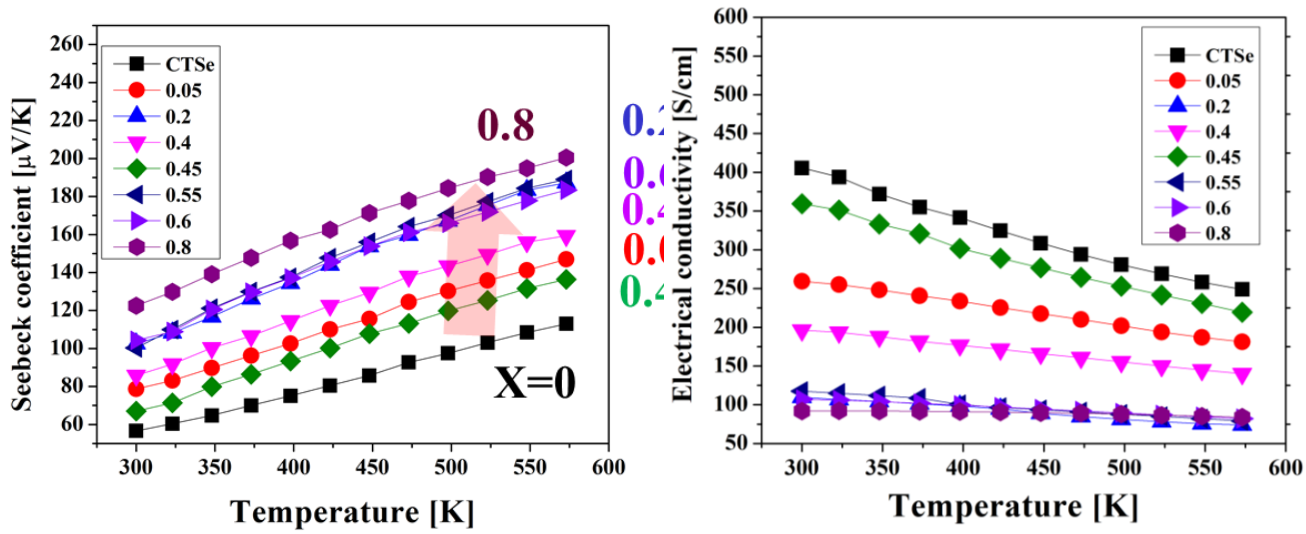


Figure 4. Temperature dependence of (a) Seebeck coefficient, (b) electrical conductivity of the CTSe and $\text{Cu}_2\text{Sn}(\text{S}_x, \text{Se}_{1-x})_3$ ($0 \leq X \leq 0.8$) solid solution samples..

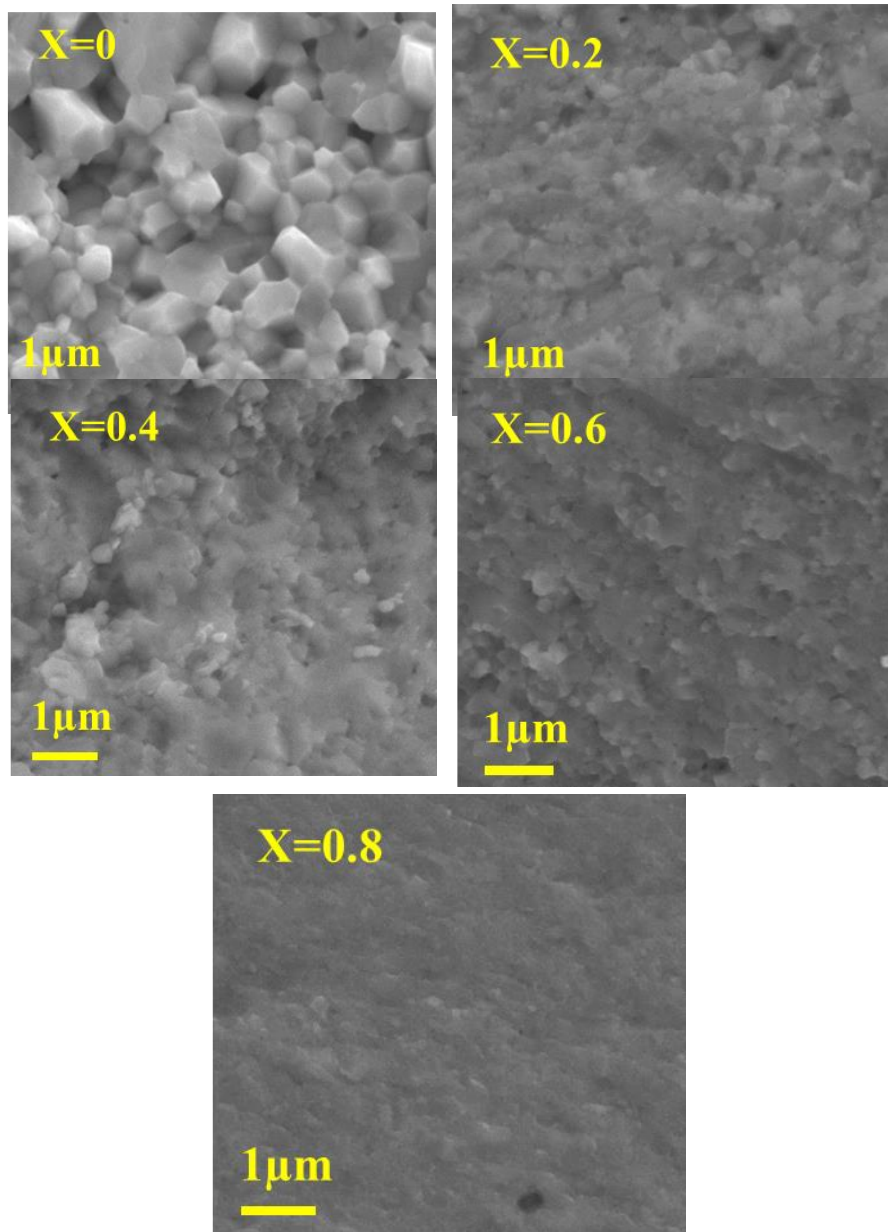


Figure5. FE-SEM images of the CTSe and $\text{Cu}_2\text{Sn} (\text{S}_x, \text{Se}_{1-x})_3$ ($0 \leq X \leq 0.8$) solid solution samples. The FE-SEM analyses were performed on the non-polished surfaces of the broken pellets.

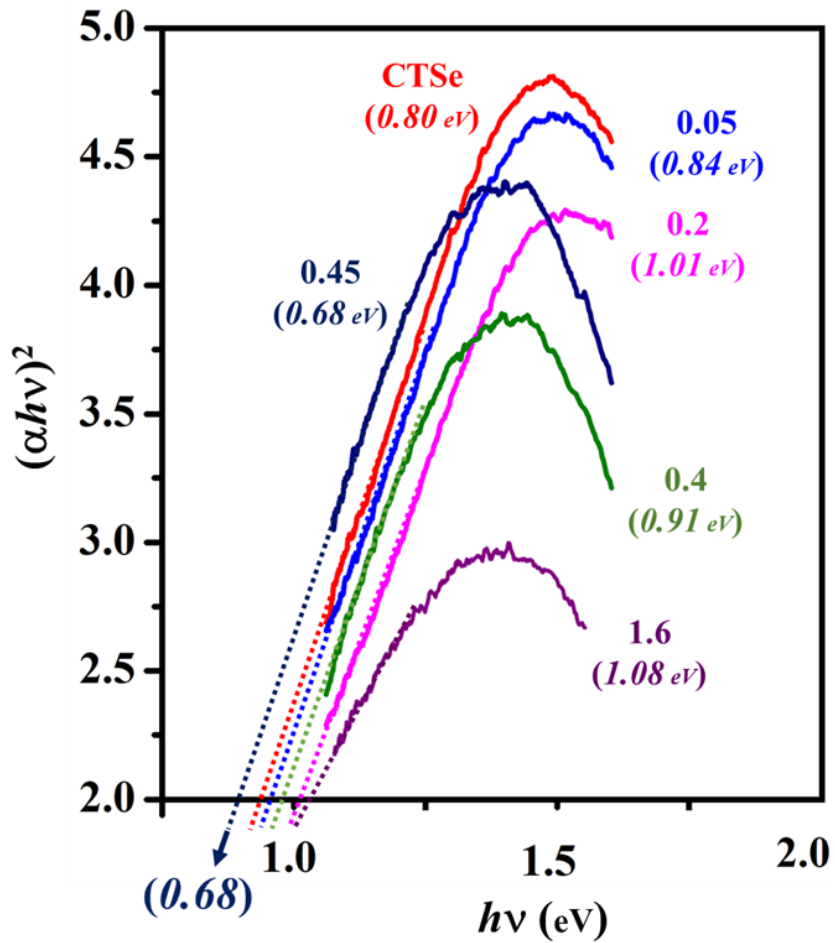


Figure 6. Shows the UV-Vis spectroscopy measurements for the CTSe and $\text{Cu}_2\text{Sn}(\text{S}_x, \text{Se}_{1-x})_3$ ($0 \leq x \leq 0.8$) solid solution samples. The calculated values of $h\nu$ and $(\alpha h\nu)^2$ are plotted for each sample and the band gap value for each phase was obtained by extrapolating these plots to the X-axis.

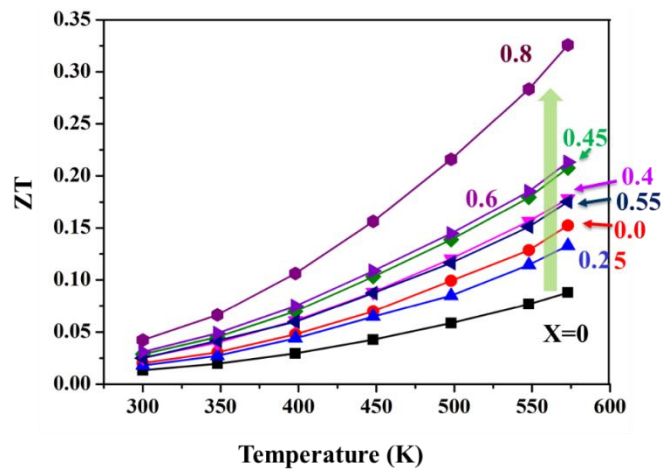
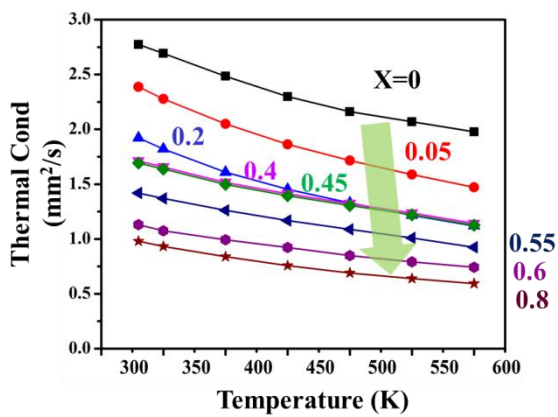


Figure 7. Temperature dependence of (a) thermal conductivity, and (b) ZT of the CTSe and $\text{Cu}_2\text{Sn}(\text{S}_x, \text{Se}_{1-x})_3$ ($0 \leq x \leq 0.8$) solid solution samples

6.4 Summary

Cu_2SnS_3 and $\text{Cu}_2\text{Sn}(\text{S}_x, \text{Se}_{1-x})_3$ ($0 \leq X \leq 0.8$) solid solution were prepared using mechanical alloying (MA) followed by spark plasma sintering. Rietveld refinement of the powder X-ray diffraction (XRD) data was performed to determine the variation in the lattice constants of the $\text{Cu}_2\text{Sn}(\text{S}_x, \text{Se}_{1-x})_3$ ($0 \leq X \leq 0.8$) solid solution with gradual replacing of Se with S. Here we found that the band gap and TE properties optimization as well as reducing in thermal conductivity can be efficiently achieved by careful optimizing of the composition of $\text{Cu}_2\text{Sn}(\text{S}_x, \text{Se}_{1-x})_3$ ($0 \leq X \leq 0.8$) solid solution for enhanced TE performance of the CTSe.

6.5 References:

- 1) F. Ioffe, A. F. (Abram Fedorovich). "Semiconductor Thermoelements and Te Cooling." (1880-960).
- 2) A.J. Minnich, M. S. Dresselhaus, Z. F. Ren, G. Chen. "Bulk Nanostructured Te Materials: Current Research and Future Prospects." *Energy & Environmental Science* 2, no. 5 (2009): 466-79.
- 3) Bell, L.E. "Cooling, Heating, Generating Power, and Recovering Waste Heat with Te Systems." *Science* 321, no. 5885 (2008): 1457-61.
- 4) D. Park, H. Ju, T. Oh, J. Kim. "Facile Fabrication of One-Dimensional Te/Cu₂Te Nanorod Composites with Improved Te Power Factor and Low Thermal Conductivity." *Sci Rep* 8, no. 1 (2018): 18082.
- 5) H. WU, R. LI "Properties of Bismuth Telluride Nanomaterials: A Computer Simulation Study." *Journal of Nanoelectronics and Optoelectronics* 12 (2017): 1199-202.
- 6) J. Fan, H. L. Liu, X. Y. Shi, S. Q. Bai, X. Shi, L. D. Chen. *Acta Mater* 61 (2013): 4297-30.

- 7) Kim, S. I. Lee, K. H. Mun, H. A. Kim, H. S. Hwang, S. W. Roh, J. W. Yang, D. J. Shin, W. H. Li, X. S. Lee, Y. H. et al. "Dense Dislocation Arrays Embedded in Grain Boundaries for High-Performance Bulk Te." *Science* 348 (2015): 109–14.
- 8) Z. H. GE, L. D. ZHAO, D. WU, X. Y. LIU, B. P. ZHANG, J. F. LI, J. Q. HE "Low-Cost, Abundant Binary Sulfides as Promising Te Materials." *Materials Today* 19 (2016): 227-39.

7 Chapter 7

The effect of substrate temperature on the microstructure and thermoelectric properties of pulsed laser deposited Cu_2SnSe_3 thin film

7.1 Introduction

TE energy technology utilizes the waste heat to generate electricity and address the global environmental issues. TE technology is expected to attract more attention from the commercial sectors in near future for applications such as remote area sensors, wearable portable electronic devices and Peltier solid state cooling systems [1-3]. Currently, bulk TE materials have not attracted a large part of the energy market due to its lower energy conversion efficiency compared to other renewable energy harvesting technologies. But for TE thin films, a great potential is expected in the near future due to its higher power density, light weight and compact size.

Currently available commercial TE materials like Bi_2Te_3 , Sb_2Te_3 and PbTe comprised of either toxic or expensive elements [4, 5]. Thus, the exploration of new TE materials with non-toxic, less-expensive and earth-abundant elements is one of the current focuses of the TE community. The ternary chalcogenide CTSe with diamond-like structure is thought to be one of the promising TE materials due to large flexibility in tuning its electronic and physical properties [6]. CTSe

elements are not from rarest elements category, non-toxic and not that expensive like Pb and Te. Recently CTSe materials are studied by various researchers in bulk form to explore its TE potential, but the TE properties of CTSe 2D structure or thin films is never been reported so far. Due to high conductive nature of the CTSe it is expected that the CTSe thin film can give us much better TE properties compare to thin films of conventional TE compounds like SnSe, due to incorporation of defects during thin film deposition.

There were reports on the fabrication of CTSe thin films for solar energy applications, which were prepared by co-evaporation [7,8], sputtering [9], salinization of metal precursors [10], flash evaporation [11] and so on. All of these techniques have a common challenge which is the controllability of the evaporation rates of the source materials. On another hand pulsed laser deposition (PLD) has the characteristic to replicate well the structure and composition of the target materials in the deposited film compared to rest of the thin-film deposition approaches [12]. PLD is a versatile technique for thin film synthesis which ablates material from a solid target using laser and deposits it on the substrate. We used PLD to grow CTSe thin films for the first time and studied its TE properties.

It is vital to study the effects of deposition conditions of a thin film on its microstructure, composition, and physical properties when exploring its potential. There, however, are only few reports on such relationships for CTSe film deposited by various deposition techniques [7, 9, 11, 13] and the effects of deposition conditions on thin films of CTSe deposited by PLD have not been

reported. In this work, we report the results of the studies on the effects of substrate temperature on the microstructure and TE properties of pulsed laser deposited CTSe thin films. We also studied the TE properties of the CTSe films for the first time. A power factor of 2.8×10^{-4} (W/m²K) was achieved with the CTSe film deposited on the silicon substrate the temperature of which was 350 °C.

7.2 Experimental procedure

7.2.1 Sample preparation

CTSe powder was directly synthesized from a stoichiometric mixture of Se 99.99 %, Sn 99.99 % and Cu 99.99 % powders (Kunjundo Chemicals-Japan of average size 5 μ) by mechanical alloying for 5 hours in an inert media. Spark plasma sintering (SPS) was used to make a dense pellet target, which relative density was calculated to be nearly 95 %. An appropriate amount of CTSe powder was put into a graphite die and was pressed up to 60 MPa for 20 minutes at 570 °C in an SPS apparatus (SPS-Weltec). The consolidated CTSe target was in the shape of a disc pellet of 8 mm in height with 25 mm diameter.

7.2.2 Substrate preparation

Silicon substrates, in two size ranges of 20 by 10 mm and 10 by 10 mm, were chosen for the deposition of the CTSe films. Si wafers of 500 μ m thickness with (100) orientation and *p*-type resistivity 9~10 (Ω .cm) were cleaned with acetone for 10 minutes in a sonicator to remove any contaminations adhered on the surface. After washing, the Si wafers were furnace heated up to 800 °C for 12 hours in Ar atmosphere to remove any moisture or adsorbed oxygen on the

surface. Finally, $\cong 200 \text{ \AA}$ -thick Pt coating was applied on the substrate surface using a Pt coater to make the Si surface electrically conductive, improve the adherence of the CTSe film to the substrate and also to improve film conformity.

7.2.3 Deposition process

A KrF excimer laser source was used to ablate the polycrystalline CTSe target at an energy density of $\sim 0.9 \text{ J/cm}^2$. The vacuum chamber was first evacuated using a rotary pump up to certain level followed by a turbo pump to achieve high vacuum of around $7.5 \times 10^{-6} \text{ mTorr}$. The incident laser beam hits the rotating target to produce an intense plasma plume ahead of the target surface upon laser irradiation. Various deposition conditions were used to optimize the PLD parameters like background pressure, laser energy density and pulse repetition rate etc. Ar gas was introduced into the chamber with a background pressure of 5 mTorr to control the shape of the plasma plume and the quality of the deposited film. Depositions were carried out at the three selected substrate temperatures (300, 350 and 400 °C) with pulse repetition rate of $\sim 5 \text{ Hz}$ for 40 minutes.

7.2.4 Characterizations

Information on the phases and the crystallinity of the films were obtained from X-ray diffraction (XRD) (D-8 Advance, Bruker) with Cu-K α radiation. The XRD spectra were recorded in the range of 20 to 65 degrees 2θ . The morphology and thickness of the samples were studied by field emission scanning electron

microscopy (FE-SEM) (Merlin compact, ZEISS, UK). The CTSe films were electrically conductive, and so we did not need any conductive coating for FE-SEM analysis. To measure the film thickness by FE-SEM, the film samples were broken into two parts. The cross sections of the broken film samples were observed using SEM. This approach not only enabled us to measure the film thickness, but also to study the inside morphology of the film. The Pt layer thickness was estimated from the power and time during DC sputtering process of Pt coating on the Si substrate.

The Seebeck coefficients and electrical resistivities were measured from 25 °C to 300 °C with increasing temperatures, using commercial TE measurement system (ZEM-3). The measurements were performed in inert media to prevent any oxidation during measurements at high temperature. Carrier concentration (p_H) and mobility (μ_H) of the samples were measured by Hall effect measurements system (Ecopia). The measurements were carried out on square-shape samples, in a van der Pauw configuration at room temperature with an applied magnetic field of 0.56 Tesla (T). Optical band gap measurements were performed by Ultraviolet-visible (UV-Vis) spectroscopy on the thin film samples, using a UV-Vis/NIR spectrometer (JASCO, V-770). The optical absorption spectra were collected in the wavelength range of 800–1600 nm, with a scan step size of 0.5 nm.

7.3 Results and discussion

The XRD spectra of the CTSe thin films deposited using pulsed laser at three different substrate temperatures 300 °C, 350 °C and 400 °C, which were named as S1, S2 and S3 respectively, are given in Fig. 1. The XRD spectra show that the deposited films are monoclinic CTSe. They also show that all the major peak positions of the CTSe target matches well with those of the deposited films. It means that CTSe monoclinic phase was successfully ablated and deposited on the Si substrate without any phase changes. A small peak around 33 degree 2-theta in XRD of all three films represents the (002) peak of Si substrate. The intensity ratios of $I_{(002)}/I_{(060)}$ and $I_{(002)}/I_{(062)}$ for all the samples were calculated, and the results are listed in Table 1. It is shown that the intensity ratios are increased with increasing substrate temperature. The increase in intensities of the (001) peaks with respect to non- (001) peak shows that the films have (001) preferred orientation and that the degree of preferred orientation is increased as the substrate temperature is increased.

Fig. 2 shows the FE-SEM surface images of (a) Pt coated Si substrate and (b)-(d) CTSe films deposited at various substrate temperatures. Cross-sectional views and the thicknesses of the three films are shown in Fig. 2 (e)-(g), while the composition of each film is given in table along each sample in the FE-SEM images in Fig. 2 (b)-(d). The surface of the Pt-coated Si substrate was free of any contamination and defects in the scale shown in Fig. 2(a). Sample S1 shows smooth CTSe film along with micron size particles. In the sample S2, it can be seen that the grains seem to grow more in size compared to S1 where average

grain size is in under 3 microns. Also small nm-size pores are formed on the film surface on the S2 sample, which we think may come from the loss of Se element from the surface grains. The sample deposited at 400 °C has more pores and voids compared to sample S2. We believe that with increasing substrate temperature, the crystallites of the CTSe films grow with (00*l*) preferred out-of-plane orientation and the grain shape changes (especially when the substrate temperature changes from 350 °C to 400 °C). The preferred orientation in sample S3 leads to corrugated type morphology leaving behind so many pores and voids. The morphological observation from SEM analyses agrees well with our XRD results, where FWHM values decreased from sample S1 to S3, as shown in Table 1, which is due to the increase of the grain size with increasing substrate temperature. The FE-SEM results were further confirmed by the atomic force microscopy (AFM) analysis, as shown in Fig. 3. It can be seen in Fig. 3 (a) that nm size Pt particles are distributed over the surface and also the topography is relatively smooth. The morphological features are changing from sample S1 to S3 which is in agreement with SEM analysis, where the roughness of the sample S3 is higher compare to other two samples. The roughness of the thin films was further confirmed by the quantitative AFM analysis of average RMS data and results are presented in Fig. 4. Few coarse particles on the film surface were observed in all three samples as shown in Fig. 2. The phenomena are common in PLD films, where coarse particles are ablated and directly deposited on the substrate.

The effect of substrate temperature on the TE properties of all three films is shown in Fig. 5. All three films are *p*-type, with positive Seebeck coefficient values shown in Fig. 5(a). The Seebeck coefficient is decreased, and electrical conductivity is increased with increasing substrate temperature from samples S1 to S2 as shown in Fig. 5(a) and (b). This can be explained from the changes of carrier concentration and electronic mobility data shown in Fig. 5(d). The carrier concentration is increased with increasing substrate temperature from 300 to 350 °C, due to the increase in vacancies generated by the loss of Se. Loss of Se with increasing substrate temperature was further confirmed by the EDS compositional analysis of the three film samples as shown in Fig. 2 (b)-(d), where the Se atomic wt % is going to decrease from sample S1 to S3. The increase in carrier concentration for the sample S2 can lead to the decrease of mobility. This is due to the increased amount of carrier scattering which can suppress the mobility of the charge carriers, which explains why its Seebeck coefficient was relatively low compared to sample S1. We measured the optical band gaps of the film samples, to study the effect of substrate temperature during PLD deposition on the band gap of the deposited films. For the direct band gap systems, the relation between optical absorption and band gap energies are given by [14]

$$\alpha h\nu = A(h\nu - E_g)^{0.5} \quad (1)$$

Where ν is the frequency radiation, A is the constant and h the Planck's constant. Fig. 6 shows the Tuac plots of the corresponding samples, from which the band gaps were estimated by The extrapolating the linear region of the plot to the x -axis. In Fig. 6 it can be seen that the band gap values decreased largely from

sample S1 to S3. This decrease in band gap value may be due to the change of the crystallites size of the deposited film particles with increasing substrate temperature. It is noticeable that although the band gap of the sample S3 was smaller than S1 and S2, but unexpectedly, electrical conductivity was not higher compare to other two samples. It means that the decrease in electrical conductivity is due to dominated effect of microstructure instead of effect of band gap. The calculated power factor values for the three samples measured at different temperatures between 25 °C and 300 °C are shown in Fig. 5(c). Sample S2 shows the power factor of $\sim 2.8 \times 10^{-4}$ at 300 °C which is comparable with the values of bulk CTSe reported previously [15-17]. In sample S3, both Seebeck coefficient and electrical conductivity are low compared to the other two samples which were deposited at lower temperatures. The microstructure of S3 shown in Fig. 2. (d) (Pores and voids on the film surface) can possibly degrade the electrical transport properties of the film S3. Both carrier concentration and mobility of S3 were low compared to samples S1 and S2, probably due to loss in film density [18], but the actual reason is not clear at this point. From these observations it can be concluded that the optimum substrate temperature for CTSe film deposited by PLD is around 350 °C at which the largest power factor was achieved among the studied substrate temperatures when all other parameters remain the same.

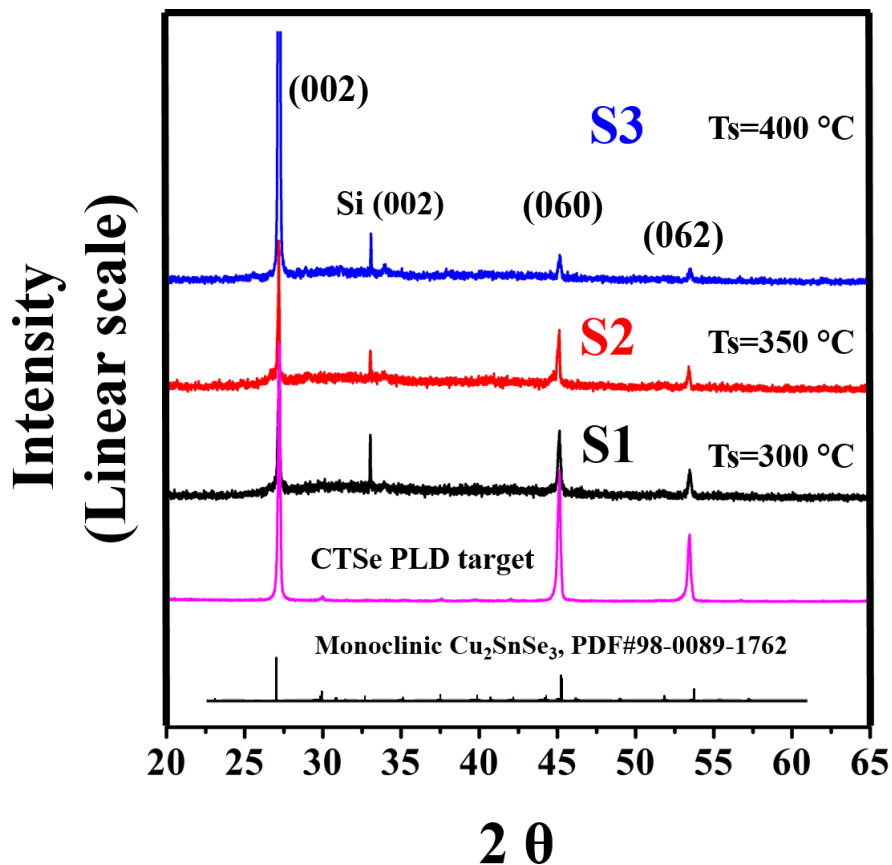


Figure 2. XRD spectra of the CTSe target and CTSe thin films deposited on Pt coated Si substrate at various temperatures by PLD. The peak around 33 degrees 2θ , comes from the (002) reflection of the Si substrate. The bottom line represents the reference PDF card of the monoclinic phases of CTSe.

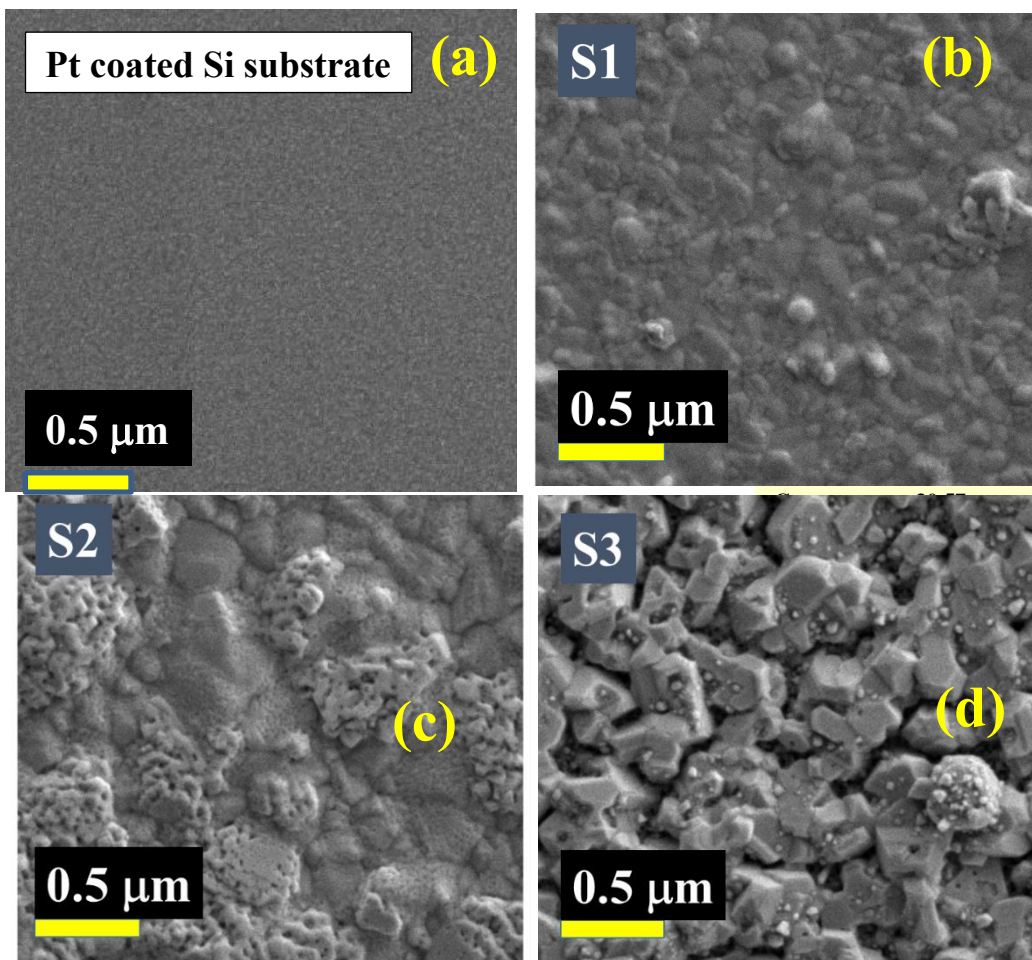


Figure 3. FE-SEM surface images of (a) Pt coated Si substrate and (b)-(d) CTSe thin films deposited by PLD at various substrate temperatures.

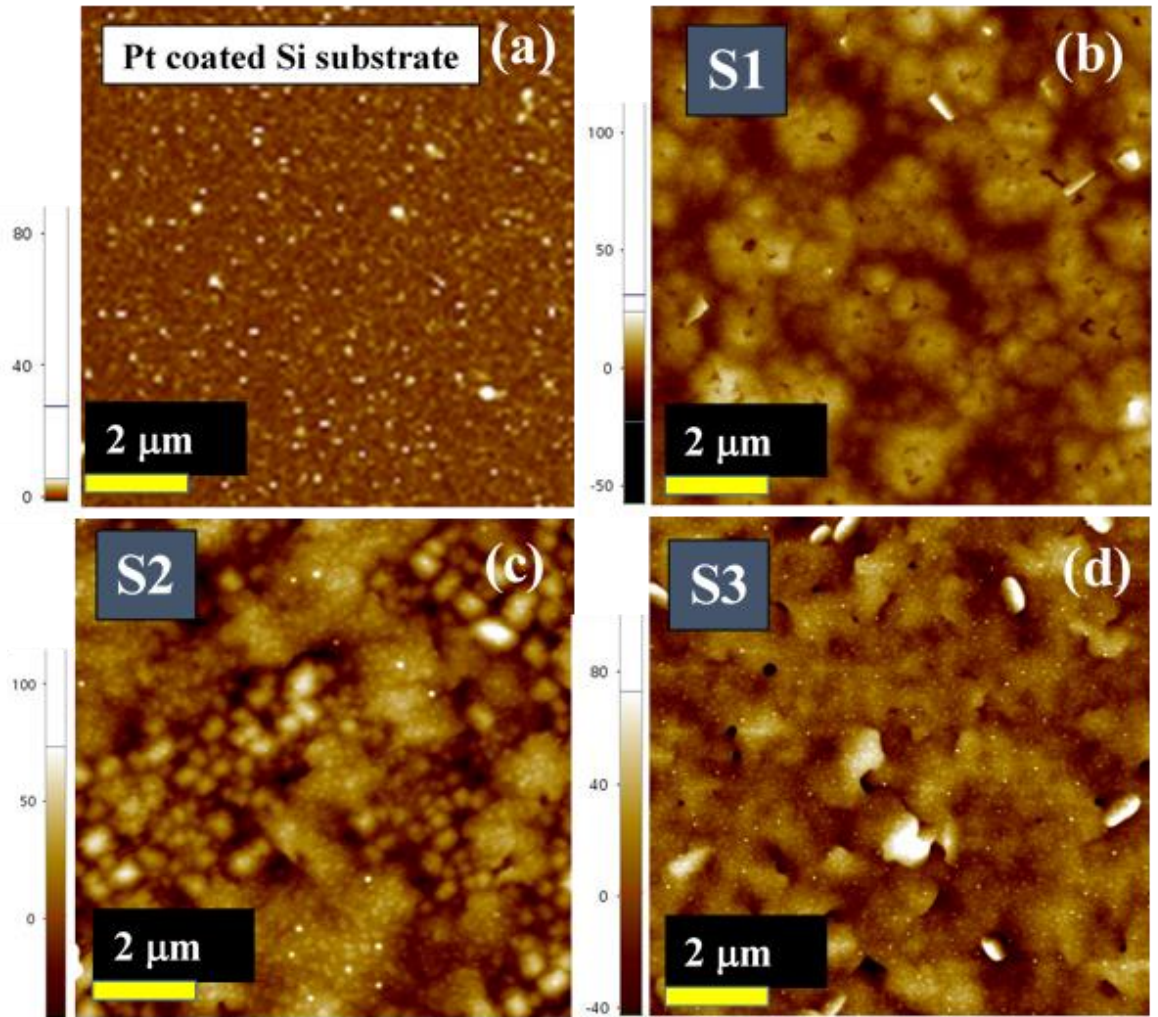


Figure 3. AFM surface images of (a) Pt coated Si substrate and (b)-(d) CTSe thin films deposited by PLD at various substrate temperatures.

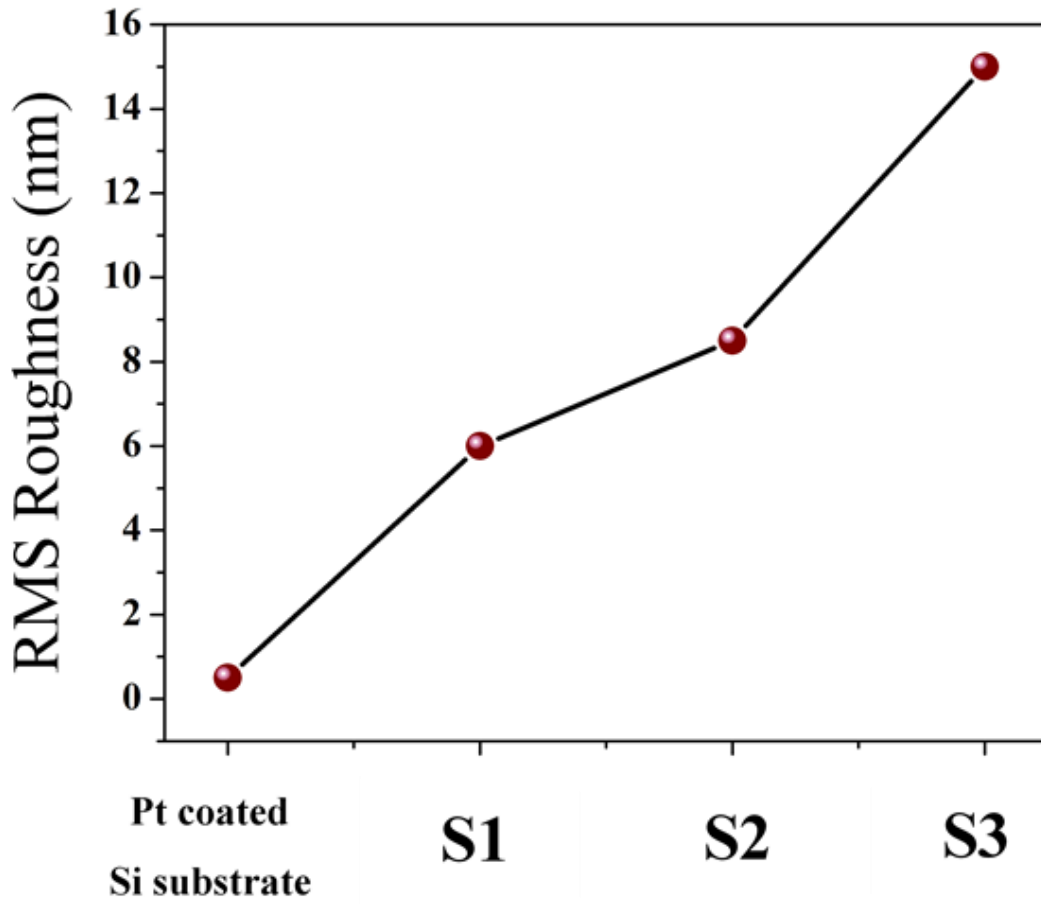


Figure 4. The average roughness in nm of 10 by 10 μm surface area, calculated during topographical AFM analysis of (a) Pt coated Si substrate and (b)-(d) CTSe thin films.

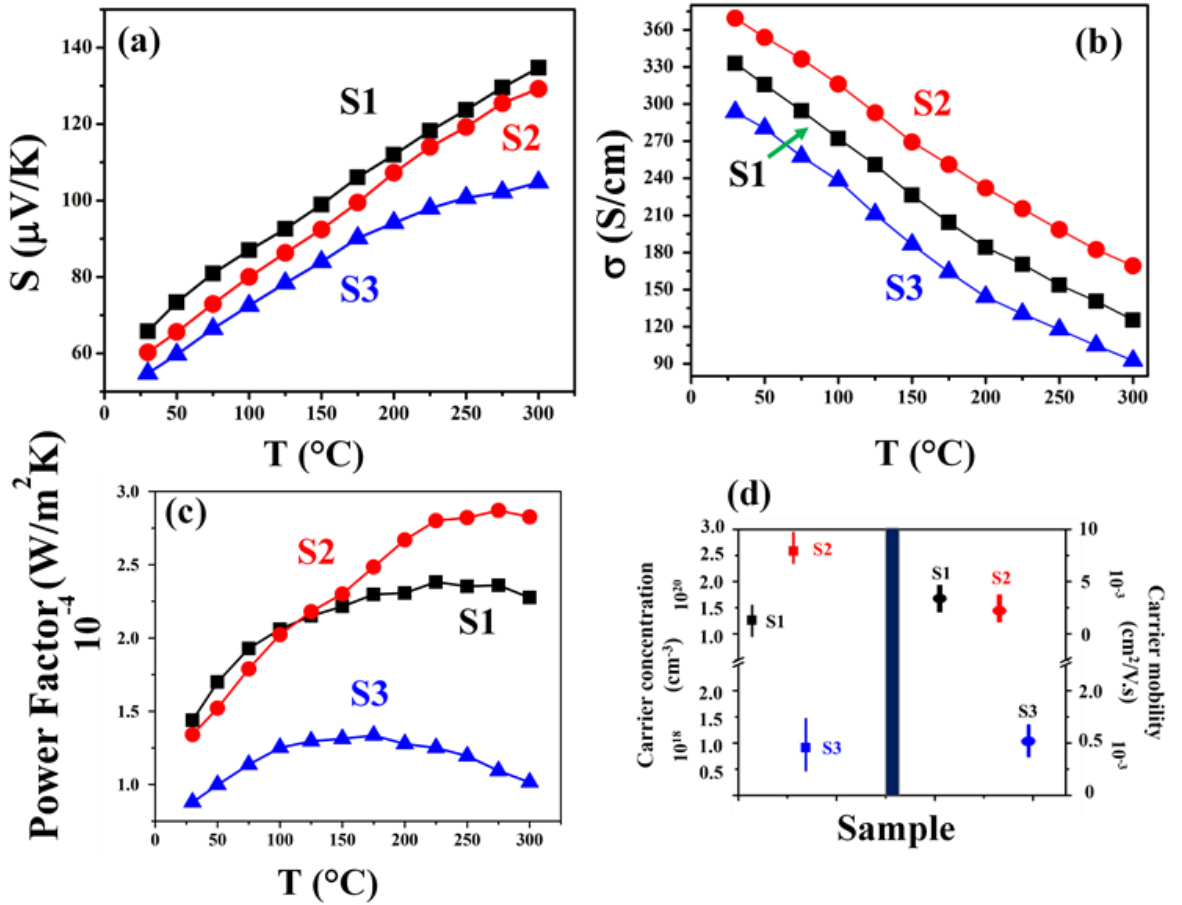


Figure 5. Temperature dependence of (a) Seebeck coefficient, (b) electrical conductivity, (c) power factor, and (d) carrier concentration (left) and carrier mobility (right) of the CTSe thin film samples deposited at various temperatures.

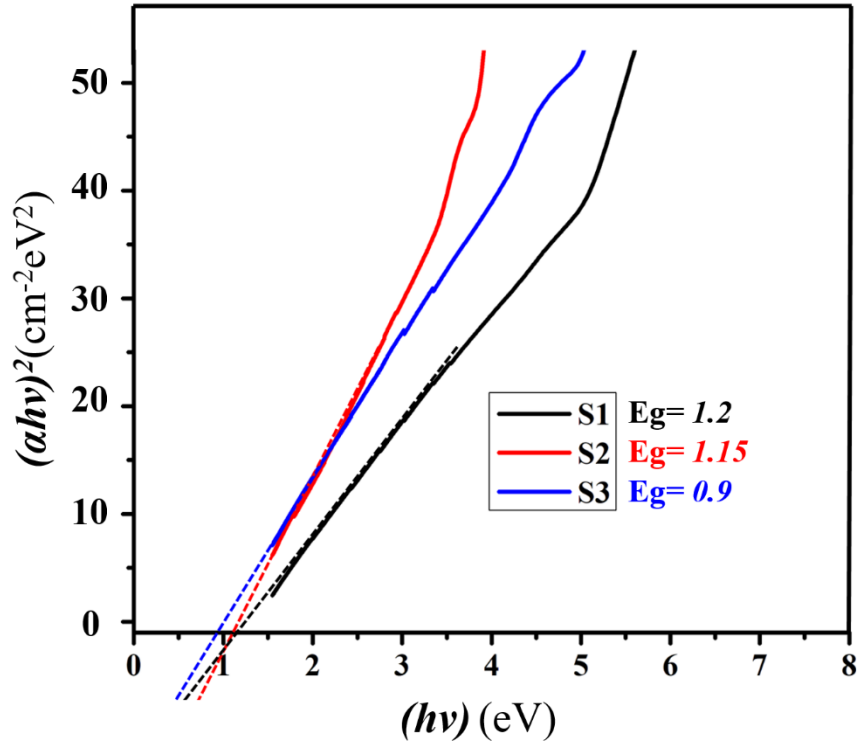


Figure 6. Band gap spectra obtained from Tuc plot approximation for the sample S1, S2 and S3 and the corresponding band gap values are given.

Table 2. The relative intensity ratios of the major peak of (002) with respect to the (060) and (062) peaks calculated from the XRD spectra of the PLD target and CTSe thin films along with the FWHM values of the major peak.

Sample	(I_{002}/I_{060})	(I_{002}/I_{062})	FWHM of the major peak (002)
PLD Target	2	4	
S1(300 °C)	2	4.6	0.16
S2(350 °C)	2.6	5.4	0.15
S3(400 °C)	18	32	0.13

7.4 Summary

CTSe thin films were deposited by PLD for the first time, and the effects of substrate temperature on the microstructure and TE properties of the films were investigated. A monoclinic CTSe target and Pt-coated silicon substrates were used to deposit films at substrate temperatures of 300, 350 and 400 °C. The crystal structure was successfully transferred to the Si substrate from the CTSe target by laser ablation without any phase changes, and all three film samples retained the monoclinic phase structure. The TE properties of the films were studied, and it was found that 350 °C is the optimized substrate temperature in which the highest power factor of 2.8×10^{-4} (W/m²K) was achieved among the studied samples. Increasing substrate temperature further up to 400 °C degraded the microstructure and electrical properties of the deposited film, and hence the power factor was decreased compared to the other films deposited at 300 and 350 °C. The power factor of 2.8×10^{-4} (W/m²K) of the sample S2 is very close to the reported value for bulk CTSe. A high power factor which is comparable with bulk CTSe, along with other benefits like higher energy density, light weight and compact size, makes CTSe film a potential candidate for various TE applications.

7.5 References:

- 1) WANG, Y., SHI, Y. G., MEI, D. Q. & CHEN, Z. C. 2018. Wearable TE generator to harvest body heat for powering a miniaturized accelerometer. *Applied Energy*, 215, 690-698.
- 2) GAYNER, C. & KAR, K. K. 2016. Recent advances in TE materials. *Progress in Materials Science*, 83, 330-382.
- 3) KIM, Y. J., GU, H. M., KIM, C. S., CHOI, H., LEE, G., KIM, S., YI, K. K., LEE, S. G. & CHO, B. J. 2018. High-performance self-powered wireless sensor node driven by a flexible TE generator. *Energy*, 162, 526-533.
- 4) WU, H. & LI, R. 2017. Properties of Bismuth Telluride Nanomaterials: A Computer Simulation Study. *Journal of Nanoelectronics and Optoelectronics*, 12, 1199-1202.
- 5) GE, Z. H., ZHAO, L. D., WU, D., LIU, X. Y., ZHANG, B. P., LI, J. F. & HE, J. Q. 2016. Low-cost, abundant binary sulfides as promising TE materials. *Materials Today*, 19, 227-239.
- 6) SHI, X. Y., XI, L. L., FAN, J., ZHANG, W. Q. & CHEN, L. D. 2010. Cu-Se Bond Network and TE Compounds with Complex Diamond like Structure. *Chemistry of Materials*, 22, 6029-6031.
- 7) KIM, K. M., TAMPO, H., SHIBATA, H. & NIKI, S. 2013. Growth and characterization of coevaporated CTSe thin films for photovoltaic applications. *Thin Solid Films*, 536, 111-114.
- 8) HE, M., LOKHANDE, A. C., KIM, I. Y., GHORPADE, U. V., SURYAWANSHI, M. P. & KIM, J. H. 2017. Fabrication of sputtered deposited Cu₂SnS₃ (CTS) thin film solar cell with power conversion efficiency of 2.39%. *Journal of Alloys and Compounds*, 701, 901-908.
- 9) KUO, D. H., HAUNG, W. D., HUANG, Y. S., WU, J. D. & LIN, Y. J. 2010. Single-step sputtered CTSe films using the targets composed of Cu₂Se and SnSe₂. *Thin Solid Films*, 518, 7218-7221.
- 10) TANG, Z. G., AOYAGI, K., NUKUI, Y., KOSAKA, K., UEGAKI, H., CHATANA, J., HIRONIWA, D. & MINEMOTO, T. 2015. Reaction path for formation of CTSe film by selenization of Cu-Sn precursor. *Solar Energy Materials and Solar Cells*, 143, 311-318.

- 11) CHANDRA, G. H., KUMAR, O. L., RAO, R. P. & UTHANNA, S. 2011. Influence of substrate and selenization temperatures on the growth of CTSe films. *Journal of Materials Science*, 46, 6952-6959.
- 12) ASHFOLD, M. N. R., CLAEYSSENS, F., FUGE, G. M. & HENLEY, S. J. 2004. Pulsed laser ablation and deposition of thin films. *Chemical Society Reviews*, 33, 23-31.
- 13) AZIZ, A. A., ELSAYED, M., ABU BAKR, H., EL-RIFAI, J., VAN DER DONCK, T., CELIS, J. P., LEONOV, V., FIORINI, P. & SEDKY, S. 2010. Pulsed Laser Deposition of Bismuth Telluride Thin Films for Microelectromechanical Systems TE Energy Harvesters. *Journal of Electronic Materials*, 39, 1920-1925.
- 14) BHASKAR, P. U., BABU, G. S., KUMAR, Y. B. K. & RAJA, V. S. 2011. Investigations on co-evaporated CTSe and CTSe-ZnSe thin films. *Applied Surface Science*, 257, 8529-8534.
- 15) SIYAR, M., CHO, J. Y., YOUN, Y., HAN, S., KIM, M., BAE, S. H. & PARK, C. 2018. Effect of annealing temperature on the phase transition, band gap and TE properties of CTSe. *Journal of Materials Chemistry C*, 6, 1780-1788.
- 16) FAN, J., CARRILLO-CABRERA, W., AKSELRUD, L., ANTONYSHYN, I., CHEN, L. D. & GRIN, Y. 2013. New Monoclinic Phase at the Composition CTSe and Its TE Properties. *Inorganic Chemistry*, 52, 11067-11074.
- 17) LI, Y. Y., LIU, G. H., LI, J. T., CHEN, K. X., LI, L. F., HAN, Y. M., ZHOU, M., XIA, M. J., JIANG, X. X. & LIN, Z. S. 2016. High TE performance of In-doped CTSe prepared by fast combustion synthesis. *New Journal of Chemistry*, 40, 5394-5400.
- 18) CHEN, X., CHANG, SIYI, CHEN, JIN 2018. Porosity-mediated High-performance TE Materials, arXiv:1810.03356.